

# Selective laser sintering of polymer particles studied by in-situ visualization

**Citation for published version (APA):**

Hejmady, P. (2021). *Selective laser sintering of polymer particles studied by in-situ visualization*. [Phd Thesis 1 (Research TU/e / Graduation TU/e), Mechanical Engineering]. Technische Universiteit Eindhoven.

**Document status and date:**

Published: 04/02/2021

**Document Version:**

Publisher's PDF, also known as Version of Record (includes final page, issue and volume numbers)

**Please check the document version of this publication:**

- A submitted manuscript is the version of the article upon submission and before peer-review. There can be important differences between the submitted version and the official published version of record. People interested in the research are advised to contact the author for the final version of the publication, or visit the DOI to the publisher's website.
- The final author version and the galley proof are versions of the publication after peer review.
- The final published version features the final layout of the paper including the volume, issue and page numbers.

[Link to publication](#)

**General rights**

Copyright and moral rights for the publications made accessible in the public portal are retained by the authors and/or other copyright owners and it is a condition of accessing publications that users recognise and abide by the legal requirements associated with these rights.

- Users may download and print one copy of any publication from the public portal for the purpose of private study or research.
- You may not further distribute the material or use it for any profit-making activity or commercial gain
- You may freely distribute the URL identifying the publication in the public portal.

If the publication is distributed under the terms of Article 25fa of the Dutch Copyright Act, indicated by the "Taverne" license above, please follow below link for the End User Agreement:

[www.tue.nl/taverne](http://www.tue.nl/taverne)

**Take down policy**

If you believe that this document breaches copyright please contact us at:

[openaccess@tue.nl](mailto:openaccess@tue.nl)

providing details and we will investigate your claim.

Selective laser sintering of polymer particles studied by  
*in-situ* visualization

Prakhyat Hejmady

Selective laser sintering of polymer particles studied by *in-situ* visualization

by Prakhyat Hejmady

Technische Universiteit Eindhoven, 2021.

A catalogue record is available from the Eindhoven University of Technology Library.

ISBN: 978-90-386-5198-9

Cover design: Prakhyat Hejmady

Printed by: Gildeprint, Enschede, The Netherlands

This work was financially supported by Brightlands Material Center, Geleen, The Netherlands.

©Copyright, 2021, Prakhyat Hejmady. All rights reserved.

Selective laser sintering of polymer particles studied by  
*in-situ* visualization

PROEFSCHRIFT

ter verkrijging van de graad van doctor aan de Technische Universiteit  
Eindhoven, op gezag van de rector magnificus prof.dr.ir. F.P.T.  
Baaijens, voor een commissie aangewezen door het College voor  
Promoties, in het openbaar te verdedigen op donderdag 4 februari 2021  
om 16:00 uur

door

Prakhyat Hejmady

geboren te Mulki, India



Dit proefschrift is goedgekeurd door de promotoren en de samenstelling van de promotiecommissie is als volgt:

voorzitter: prof.dr.ir. M.G.D. Geers  
promotor: prof.dr.ir. P.D. Anderson  
1<sup>e</sup> co-promotor: prof.dr.ir. R.M. Cardinaels  
2<sup>e</sup> co-promotor: dr.ir. L.C.A. van Breemen  
leden: prof.dr. A.J. Müller (University of the Basque)  
prof.dr. J.H. Hattel (Technical University Denmark)  
prof.dr.ir. J.M.J. den Toonder (Eindhoven University of Technology)  
prof.dr.-Ing. K. Wudy (Technical University of Munich)

Het onderzoek of ontwerp dat in dit proefschrift wordt beschreven is uitgevoerd in overeenstemming met de TU/e Gedragscode Wetenschapsbeoefening.

## Summary

Additive Manufacturing (AM) offers the possibility to produce components with increasingly complex geometries, which cannot be achieved with traditional processing methods. Selective Laser Sintering (SLS) is one such AM technique with promising prospects to replace some of the traditional manufacturing methods. Laser energy is utilized to sinter polymers or metals in powder form, by locally increasing the temperature. A new layer of powder is spread over the previously sintered layers, where-by the latter act as a support structure. This process is repeated, to eventually achieve the final part, without the need for molds and tools. In case of polymers, the final micro- and macro-structure is largely dependent on the processing conditions such as temperature and flow profile. However, the current lack of understanding of the underlying mechanisms governing the sintering process has hindered the implementation of this technique in industries for full scale production of products. The main issues are limited reproducibility of sintered parts and low mechanical stability. Material properties and process variables ranging from laser parameters, build chamber temperature to particle morphology and powder spreading, all affect the final part properties. Incomplete sintering of polymer particles is a commonly observed phenomena, resulting in significant remaining porosity after sintering, as well as limited interlayer adhesion. Hence, more insight in the effects of the different processing conditions and material characteristics on the final product morphology is required.

Given the number of process variables involved which can influence the final process conditions, the goal of this work is to systematically investigate sintering of two spherical polymer particles to establish a relationship between, on the one hand the sintering process conditions and material characteristics and on the other hand the generated microstructure. A simple but versatile, patented method, was developed to make spherical particles for a range of commodity polymer materials. To understand the coalescence of the particles during the sintering process and to utilize this knowledge in material processing, it is important to visualize the sintering process which is not possible in commercial machines. Therefore a dedicated experimental setup, which incorporates the main features of a 3D printing device, and at the same time allows in-situ visualization of the sintering dynamics by means of optical microscopy and/or X-ray diffraction is developed. The sintering studies were performed on amorphous, semi-crystalline and functionalized polymer particles. A parametric study was performed by varying laser parameters, particle size and build chamber temperature by tracking the evolution of the neck radius between two amorphous particles. By optical imaging, the effects of processing conditions on the sintering of the particles is determined. Partial sintering was observed when the supplied laser energy was not sufficient to substantially increase the temperature. Using infra-red (IR) imaging, the evolution of temperature with time was

acquired, thereby correlating viscosity buildup with reducing temperature at the end of the laser pulse. The sintering kinetics of the particle doublets is governed by a complex interplay between and temperature dependent effects.

For semi-crystalline polymers, laser sintering experiments with in-situ X-ray visualization were performed, whereby effects of processing conditions on crystallization kinetics were tracked in real time. Dependency of the cooling rate on the crystallization kinetics is observed by IR imaging and in-situ X-ray studies, for varying particle sizes and build temperatures. Morphological characterization of the melt doublet revealed a distinct difference between the laser effected zone at the interface of the particle and the bulk volume of the doublet. Additionally, polymer nanocomposite particles of semi-crystalline material were laser sintered. The incorporation of carbon nanotubes (CNTs) to the semi-crystalline polymer increased the crystallization kinetics. Moreover, increase in yield stress is observed for increasing CNTs content, thereby slowing down the sintering kinetics. As a result, polymer with increasing CNTs content showed lower neck growth. Electrical conductivity measurements of melt doublets showed lower electrical resistance with increased neck width at the interface of the particles. A unique experimental setup with in-situ visualization capabilities and a methodology to produce spherical polymeric particles were developed. In conclusions, in this work with this setup, correlations between process conditions during laser sintering of two spherical polymer particles and the material properties are established, for amorphous and semi-crystalline polymer particles. Relevant insights and understanding of laser-induced sintering of polymer particles is developed, paving way to optimize and tailor the 3D printing process by SLS.

# Contents

<b>Summary</b>	<b>iii</b>
<b>1 Introduction</b>	<b>1</b>
1.1 Selective Laser Sintering . . . . .	1
1.2 Research objective . . . . .	3
1.3 Outline of thesis . . . . .	3
<b>2 A processing route to spherical polymer particles via controlled drop retraction</b>	<b>5</b>
2.1 Introduction . . . . .	5
2.2 Materials and methods . . . . .	8
2.3 Results . . . . .	11
2.4 Conclusions . . . . .	20
<b>3 A novel experimental setup for <i>in-situ</i> optical and X-ray imaging of laser sintering of polymer particles</b>	<b>23</b>
3.1 Introduction . . . . .	24
3.2 Design and description . . . . .	25
3.3 Experimental procedure . . . . .	30
3.4 Results and discussion . . . . .	34
3.5 Conclusions . . . . .	40
<b>4 Laser sintering of polymer particle pairs studied by <i>in-situ</i> visualization</b>	<b>41</b>
4.1 Introduction . . . . .	42
4.2 Experimental setup . . . . .	43
4.3 Materials and methods . . . . .	45
4.4 Results and discussion . . . . .	47
4.5 Conclusions . . . . .	65
<b>5 Laser sintering of PA12 particles studied by <i>in-situ</i> optical, thermal and X-ray characterization</b>	<b>69</b>
5.1 Introduction . . . . .	69
5.2 Materials and methods . . . . .	71
5.3 Results and discussion . . . . .	76
5.4 Conclusions . . . . .	93
<b>6 Laser sintering of polyamide 12/carbon nanotube composite particle pairs</b>	<b>97</b>
6.1 Introduction . . . . .	97

6.2	Experimental procedure . . . . .	99
6.3	Results and discussion . . . . .	102
6.4	Conclusions . . . . .	114
<b>7</b>	<b>Conclusions and Recommendations</b>	<b>117</b>
7.1	Conclusions . . . . .	117
7.2	Recommendations . . . . .	120
	<b>Publications</b>	<b>143</b>
	<b>Acknowledgment</b>	<b>145</b>
	<b>Curriculum Vitae</b>	<b>147</b>

## Introduction

Additive manufacturing (AM) commonly referred to as Rapid Prototyping, Solid Freeform Fabrication or more recently as 3D Printing, is a production technology which enables fabrication of objects in a layer-wise fashion. Contrary to traditional subtractive techniques such as drilling and milling, wherein material is removed to produce functional parts, in AM the material is added only where it is required. Objects are designed using Computer-Aided-Design (CAD) software and transformed into a “Standard Tessellation Language” (STL) file for AM machines with pre-defined slices of a certain thickness. Hence, AM enables manufacturing of these slices in succession to form parts, without the need for a mold [1, 2, 3].

### 1.1 Selective Laser Sintering

Selective laser sintering (SLS) is one of those emerging AM techniques wherein the polymer material used is in powder form. The laser sintering process (Figure 1.1) starts by depositing a layer of powder material from the delivery system to the fabrication system. Infrared (IR) heaters positioned within the chamber, increases the temperature of top few layers to a desired temperature, below the melting temperature for semi-crystalline ( $T_m$ ) or glass transition temperature ( $T_g$ ) for amorphous polymer powders. Based on the x-y coordinates provided by the STL file, a laser scans over the powder bed, locally increasing the temperature of the powder above its  $T_g$  or  $T_m$ , fusing them together to form a consolidated structure [4, 5, 6, 7]. The process is repeated as successive layers are deposited and fused together by the laser in the same fashion, until the desired part geometry is complete. The entire powder bed is then removed from the fabrication station and the part is separated from the powder that supported it during fabrication. Unfused powder can then be reused for future builds.

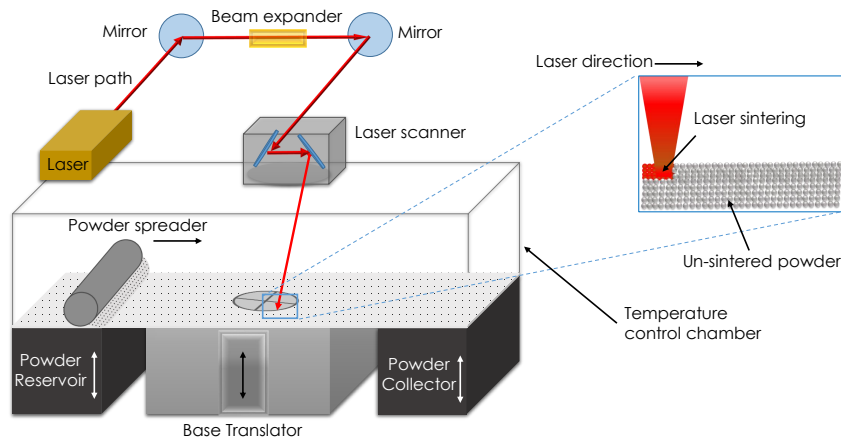


Figure 1.1: Schematic representation of a SLS machine.

The most commonly used material for SLS is PA12 due to its high melting enthalpy, low melt viscosity and its relatively narrow  $T_m$  range [8], typically of about 10 °C which are ideal material properties concerning manufacturing for SLS. This made polyamide 12 (PA12) the ideal starting material to be used by SLS processes. During the sintering process of the polymer powder, there is no pressure involved and after the desired chamber temperature has been achieved by IR heater, the laser is the only heat source which locally binds the polymer particles together [9, 10, 11]. Sintering dynamics plays a pivotal role in the melt behavior during the complete process. During laser sintering, polymer particles undergo an in-homogeneous temperature profile, giving rise to a complex flow profile. This can lead to some of the commonly found inherent defects, like porosity and poor layer-to-layer adhesion, as can be seen in Figure 1.2. This consolidated structure is a rigid and porous object having poor mechanical properties as compared to for instance injection molded products [12, 13, 14]. Particle homogeneity and laser energy supplied have a decisive effect on final part property. As a consequence, the final state of the part strongly depends on the process.

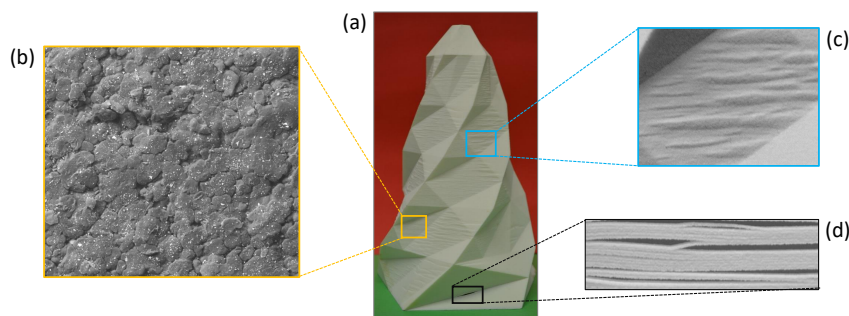


Figure 1.2: (a) Laser sintered part with inherent defects such as (b) porosity, (c) poor surface finish and (d) delamination between consecutive layer.[15]

## 1.2 Research objective

The processing conditions during SLS greatly impact the thermal conditions of the powder bed and the sintering kinetics of the material. Commercially available SLS machines have limited process parameters that can be varied, and also limited by material choice. Furthermore, with no access for in-situ visualization, insight on the sintering kinetics are unavailable. Optimization of the process is often done on a trial-and-error basis, by studying the properties of the final printed part.

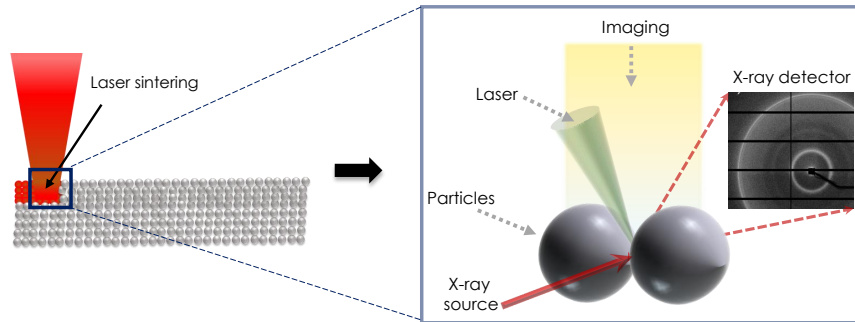


Figure 1.3: Simplification of complex SLS process (left) to a two particle system (right).

Therefore, the focus of this work is to provide a fundamental link to the influence of process conditions on sintering kinetics of polymer particles in SLS. Simplification of this process is key, therefore we study only an isolated polymer particle pair. This enables us to question how the process parameters during sintering process effect the coalescence process of polymeric particles, either amorphous and semi-crystalline. Furthermore, how a given set of process parameters can influence the crystallization kinetics as well as final morphology during and after sintering. This allows a systematic investigation of the coalescence process during sintering by linking the intrinsic material properties to the process conditions. Knowledge gained from this work can then be supplemented together with the modelling [16] as well as long term mechanical performance [17] efforts done, to be able to anticipate and predict the final part property.

## 1.3 Outline of thesis

Well defined spherical particles were utilized in this work. **Chapter 2** describes a simple and cost effective methodology to manufacture these spherical particles. An interplay between the material characteristics to the process condition is described, where temperature and time is crucial in controlling final particle shape.

To mimic the SLS process, a unique experimental setup was developed in-house to perform laser sintering experiments on polymer particle doublets. Two polymer particles were kept together in a temperature controlled chamber and were subjected to a laser pulse with a defined amount of energy. In **Chapter 3** this setup with the possibility



to perform in-situ visualization studies by optical imaging and X-ray diffraction is described. These possibilities provide crucial real time information concerning the sintering dynamics and crystallization kinetics, which was not accessible up to now.

In **Chapter 4** coalescence of two amorphous polystyrene particles (PS) are systematically investigated for varying sintering parameters. The evolution of the neck at the interface of the particles was tracked and compared with existing models to quantify the process. Combining a full material characterization with the sintering experiments, a complex interplay between flow and temperature is observed. Effects of transient rheology, due to the finite relaxation times of the polymer, effects viscosity of the polymer influencing the sintering kinetics.

To investigate the sintering dynamics of semi-crystalline polymers, in-situ x-ray experiments were performed on PA12 particles, at the ESRF in Grenoble. **Chapter 5** focuses on the influence of processing conditions on the crystallization kinetics of PA12 particles, for varying particle sizes and bed temperatures at a fixed laser energy, laser spot diameter and pulse duration. The generated X-ray data is analyzed and combined with the coalescence process obtained from optical imaging. Relations are established between flow and crystallization kinetics, thereby in-turn relating the processing to the achieved microstructure.

The influence of incorporating CNTs on crystallization and sintering kinetics of PA12 particles is investigated in **Chapter 6**. In-situ experiments were performed on PA 12 particles with varying CNTs (carbon nanotubes) content and varying particle sizes at fixed laser parameters and build temperature. A comparison is drawn from known rheological behavior of PA12 with varying CNTs content to the neck growth particle doublets by laser sintering. Electrical measurements along the melt doublets showed a correlation between neck radius width to the conductive properties.

## A processing route to spherical polymer particles via controlled drop retraction

### Abstract

In this work we describe the production of spherical polymer particles from thermoplastic polymers. A simple, cost-effective method is developed to transform rough powders into spherical particles. The polymer particles are molten within heated oil where after interfacial tension driven reduction of curvature and shape retraction can be exploited to induce a transformation to the equilibrium spherical shape. The sphericity of the obtained particles was validated by determining the aspect ratio, roundness, as well as circularity. Furthermore, batches of narrow particle size distributions are attained by sieving on different mesh sizes which allows to fractionate the resulting powder. The effects of the relevant material characteristics as well as processing conditions is investigated and is rationalized based on the governing physical processes and their scaling relations. As a result, the processing conditions can a priori be tailored depending on the material characteristics. The versatility of the method is confirmed by generating spherical particles from various thermoplastic polymers including PS, LDPE, PP, PA12 and PA12 filled with carbon nanotubes.

### 2.1 Introduction

Control over particle morphology has received tremendous attention during the past decades. Potential application areas include drug delivery systems, pigments, electronics and advanced manufacturing techniques like powder-based additive manufacturing [18, 19, 20, 21, 22]. It is often desired to control the particle size (distribution), shape,

---

*Largely reproduced from:*

- 1) Hejmady, P., Cardinaels, R. M., van Breemen, L. C. A. & Anderson, P. D., 20 Apr 2020, Polymer spheres, Patent No. 19156044.0-1102, 7 Feb 2019
- 2) Hejmady, P., van Breemen, L. C. A., Anderson, P. D. & Cardinaels, R. M., A processing route to spherical polymer particles via controlled drop retraction, *submitted to Powder Technology*

surface morphology and composition at the same time. Control over particle morphology, size and shape makes it possible to manufacture final parts with better defined property and functionality. Unfortunately, only a handful of (nearly) spherical thermoplastic polymers particles are commercially available, thereby limiting the application areas. Particles currently used in applications are either not completely spherical or are partially crosslinked. During selective laser sintering, which is a popular additive manufacturing technique, good flowability of the powder during spreading before laser sintering, is crucial for the final part properties and critically depends on the particle shape [12, 23, 24, 25]. Henceforth, having spherical particles allows for control over the final packing and size uniformity, ensuring better prediction of material behaviour and enhanced repeatability. At the same time, it is undesirable to have any degree of cross-linking leading to a reduction of the flow during the laser sintering process [18]. At present, the polymeric materials suitable for SLS are largely limited to polyamide based thermoplastic polymers, more specifically polyamide 12 (PA12), due to its good flowability, wide processing window, and availability in powder form with close to spherical particle shapes [26, 27]. The part properties that can be obtained with SLS are limited to the intrinsic material properties of the polyamide itself, thereby limiting the full potential of the process [28]. Hence, efforts have been made towards several physio-chemical techniques for the production of spherical polymer particles of various thermoplastic polymers. Industrially viability depends on the complexity of the setup, its ability to handle high viscosities, capability to produce varying sizes, and cost effectiveness [29].

Since the patent by Baumann & Wilczok [30], the precipitation method has been the most widely used technique in SLS powder production for PA12. Due to its ability to create relatively round particle shapes with good control over the particle size distribution. The precipitation method for PA12 involves dissolving the polymer in a suitable solvent under elevated temperatures and pressures. The temperature is reduced until nucleation due to thermally induced phase separation starts and is held there for a predetermined time. Supersaturation is achieved by reducing the temperature even further, after which the polymer powder is precipitated and the suspension is dried [30]. This methodology has been used successfully to create spherical microparticles for a few thermoplastics such as polypropylene (PP) [31, 32], polyethylene (PE) [33], polycarbonate (PC) [34], polyamide 6 [35], polyamide 11 (PA11) [36], polylactic-co-glycolic acid (PLGA) [37] and polybutylene terephthalate (PBT) [38]. By varying the stirring speed, and process temperature a narrow particle size distribution can be obtained with high crystallinity due to the effect of the solvent, in case of PP [31]. However, the solvents used in these works are hazardous. In the latest work PLLA particles were obtained using non-toxic solvents [39]. A similar attempt was made to obtain particles of polyoxymethylene (POM) [40], but the resulting particles were not spherical. Similar to temperature, also non-solvents can be used to induce phase separation, as demonstrated for PA12 [41]. Although applicable to various polymers, this method requires selection of the solvent and operating conditions for each particular polymer separately. Thereby, it has been shown that a complex interplay between solution-induced crystallization and liquid-liquid phase separation determines the particle formation process [31]. Moreover, rough particles with a

significant porosity are generally obtained [42].

Apart from phase separation, other techniques starting from polymers in solution are less common. For instance, an interesting method is the use of supercritical fluid extraction, wherein compounds dissolved in a liquid undergo fast expansion when in contact with a supercritical fluid, to precipitate small particles [43]. Another notable method is inkjet printing, an additive manufacturing technique to dispense droplets. Since this technique is restricted to low viscosities, polymer solutions can be used, similar to the spray drying process [44, 45].

More recently new methodologies for production of polymer particles in one processing step have been developed. Various methods are based on droplet dispersion and breakup within immiscible polymer blends whereby a sacrificial matrix polymer is used to facilitate removal of this matrix phase after particle production. Under high shear and elongational forces during polymer blending a melt emulsion is formed. The emulsion is then cooled down to solidify the spherical particles which are finally dried. Different mixing devices including a rotor-stator device, torque rheometer, extruder and Brabender mixer have been used for this purpose resulting in particles of PBT [46], PP [47], PA12 [48], PE and paraffin [49]. As sacrificial matrix polymers, polyvinylalcohol, polyethylene glycol and polyethyleneoxide have been used. However, it was concluded that prediction of the particle size is difficult due to the complex flow histories and in many cases the use of an emulsifier was critical to avoid agglomeration of the molten particles. Continuing further along the line of using a polymer blend or emulsion to generate spherical particles, droplet formation based on Plateau-Rayleigh instability of melt spun PA12 fibers in a PEO matrix [50] was studied. The main disadvantage of this method is the fact that the material needs to be processed and molten twice, which is problematic since PEO is prone to degradation and ageing while PA12 can undergo post-condensation i.e its viscosity and molecular weight increase in time at high temperatures.

In this work we demonstrate a simple, cost-effective approach to prepare spherical polymer particles and demonstrate its applicability for a wide range of thermoplastic polymers of varying molecular weight. Mechanical methods, such as milling and grinding have traditionally been the most commonly employed techniques to obtain polymer in powder form [51, 52], with their own limitations [53, 54, 55, 56, 57]. Fine powders can be produced by milling, but the obtained particles are non-spherical in nature [58]. Subsequently, the generated irregular particles obtained via wet grinding can be rounded by heating in a downer reactor [46, 59]. The rounding of the particles depends on the residence time, therefore the height of the reactor and the temperature homogeneity within it. If the time and temperature are not sufficient, the particle shape will remain irregular and anisotropic. This technique has the advantage that it is versatile and can in principle be used on a wide range of particle types. However, a heated downer reactor requires a huge and expensive installation. The method is tested for a wide range of

thermoplastic polymers of varying molecular weight and the physical phenomena underlying the shape change process are analyzed to allow a priori rational selection of the processing parameters.

## 2.2 Materials and methods

### 2.2.1 Materials

Thermoplastic polymers in pellet form namely polystyrene (PS, Sigma Aldrich, ( $M_w$ ) = 35 kg/mol), polyamide 12 (PA12, Vestamide L-1700, ( $M_w$ ) = 51 kg/mol), PA12 with 2wt% carbon nanotubes (CNTs, NC7000 from Nanocyl), isotactic polypropylene (iPP, grade SABIC, ( $M_w$ ) = 360 kg/mol) and low density polyethylene (LDPE, grade Exxon Mobil, ( $M_w$ ) = 217 kg/mol), were reduced to a coarse powder using a Retsch ZM 100 rotor milling machine at 14000 rpm. Coarse particles were removed from the powder by sieving using a stainless steel mesh (500  $\mu\text{m}$  mesh size), resulting in a powder with particle sizes < 500  $\mu\text{m}$ . Table 2.1 provides the estimated viscosity as well as surface tension values at the respective processing temperatures for each material of interest. To determine the viscosity of the polymers, frequency-sweep measurements were performed in the linear viscoelastic regime with a strain amplitude of 1%. Measurements were performed on a rotational rheometer (Anton Paar MCR502) equipped with a parallel plate geometry (25 mm diameter), where a nitrogen-flushed convection oven was used. Surface tension values for the polymer materials were obtained from literature [60]. The values were recalculated to the required temperatures using a temperature dependence of the surface tension of 0.05 mN/m [61, 62].

For the droplet retraction experiments, rice bran oil (Unidex, Netherlands), with a smoke point of 265°C was used as the matrix phase. For various vegetable oils, Esteban et al. [63] described a linear dependency between surface tension and temperature given by:

$$\gamma = A + BT, \quad (2.1)$$

where  $\gamma$  is the surface tension,  $A$  the intercept,  $B$  the negative slope and  $T$  the temperature of interest. Rice bran oil was not included in this study, but considering the minor differences between the surface tension values of the various vegetable oils, a similar behavior is assumed for rice bran oil. The measured viscosity values and estimated surface tension values for rice bran oil are added to Table 2.1.

Table 2.1: Viscosity and surface tension values for rice bran oil and polymers at the indicated temperatures. Viscosity values are taken at a shear rate of  $0.1 \text{ s}^{-1}$ .

Material	Temperature ( $^{\circ}\text{C}$ )	Viscosity (Pa·s)	Surface tension (mN/m)	Mixing time (s)
Rice Bran oil	130 - 260	0.008 - 0.0019	25.5 - 15.7 <sup>[27]</sup>	120 - 300
PS	130	90 <sup>[30]</sup>	27.2 <sup>[60]</sup>	180
PA12	210	130 <sup>[28]</sup>	29.6 <sup>[60]</sup>	120
LDPE	230	11200	26.2 <sup>[60]</sup>	240
PP	240	2709	17.3 <sup>[60]</sup>	180
PA12 + CNTs	260	17024	29.6 <sup>[60]</sup>	300

### 2.2.2 Particle production method

To allow deformation of the polymer particles, they are heated above their glass transition temperature ( $T_g$  for amorphous polymers) or melting temperature ( $T_m$  for semi-crystalline polymers) and given sufficient time for relaxation. The procedure of the production process is as follows. In a 100 ml borosilicate glass container (inner diameter of 50 mm), 50 ml of rice bran oil is heated up to a temperature higher than the glass transition temperature ( $T_g$ ) or melting temperature ( $T_m$ ) of the polymer. It is ensured that the temperature of the medium is high enough to liquify the polymer while avoiding degradation. About 1 mg of sieved polymer powder is added and the dispersion is stirred to avoid agglomeration or sedimentation of the powder particles. The suspension is stirred at a rotation speed of 30 rpm for a fixed time period of up to 5 minutes, depending on the type of thermoplastic polymer used. The stirrer is spaced at about 10 mm from the edge of the beaker. The suspension is then quenched by pouring it in another container partially filled with water at room temperature. The polymer particles remain at the rice bran oil - water interface, henceforth avoiding sedimentation of the polymer particles and sticking to the bottom of the vessel. This suspension is subsequently poured through a cylindrical column made of plexiglass containing metallic meshes of different grid sizes, as shown in Figure 2.1, which allows to separate particles depending on the mesh grid sizes. A 5 vol% surfactant solution in water is then flushed through this plexiglass column, removing any residue of rice bran oil from the particle surface. An extra step of rinsing the polymer particles with ethanol ensures a residue free particle surface. The final step involves drying the particles for 8 hours in an oven, in case of amorphous polymers below  $T_g$  and for semi-crystalline polymers sufficiently below the optimum crystallization temperature.

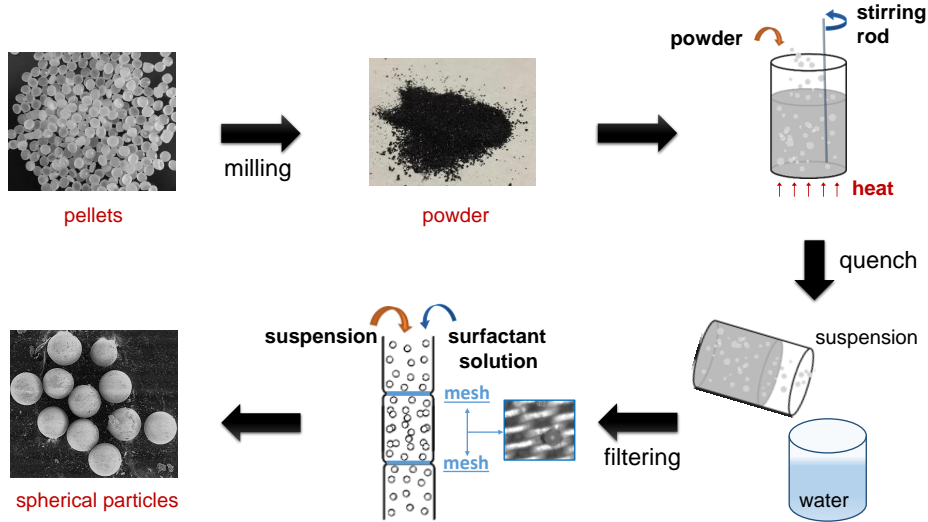


Figure 2.1: Schematic representation of experimental steps involved in producing spherical particles.

### 2.2.3 Characterization methods

Polymer particles obtained before and after the treatment process were analyzed for their shape and surface morphology by scanning electron microscopy (SEM, FEI Quanta, 10 KeV ) and optical microscopy (Olympus, 10x magnification) in bright-field illumination mode to quantitatively analyze the particle shape.

### 2.2.4 Parameters to quantify particle shape

To quantify the size of the particles, even in the case when they are not perfectly spherical, a representative diameter is defined, by measuring the cross-sectional area of each particle and converting it to diameter under the assumption of a spherical particle shape [64]:

$$d = 2\sqrt{\frac{A}{\pi}}. \quad (2.2)$$

where  $d$  is the diameter and  $A$  the area. To define the shape of the particles three parameters namely aspect ratio  $A_r$ , roundness  $R$  and circularity  $C$  are used. The aspect ratio  $A_r$  defines the global particle shape as:

$$A_r = \frac{d_{\max}}{d_{\min}}, \quad (2.3)$$

wherein  $d_{\min}$  is the smallest and  $d_{\max}$  the largest particles diameter. These diameters were determined by fitting an ellipse on the particle shape using ImageJ<sup>®</sup>. When the

particles become elongated, the aspect ratio gradually increases from one to infinity. To further take into account the curvature profile of the particle edge the roundness  $R$  is determined:

$$R = \frac{4A}{\pi(d_{\max})^2}. \quad (2.4)$$

For an ellipse,  $R$  corresponds to  $1/A_r$ , but in case of a more rectangular shape,  $R$  would be larger for the same aspect ratio  $A_r$ . Finally, the circularity  $C$  is determined, as defined by ISO 9276-62008 [65]:

$$C = \frac{4\pi A}{P^2}. \quad (2.5)$$

$P$  the perimeter of the particle. Deviations from circularity and thus values of  $C$  smaller than one can originate from an aspect ratio different from one, from shapes that are more rectangular than elliptical and finally also from the presence of protrusions on the particle surface [66]. Hence, the three parameters used to characterize particle shape are chosen in increasing order of complexity and amount of deviations from circularity.

All required parameters were determined by image analysis using the Analyze Particles option in ImageJ<sup>®</sup> processing software after thresholding the optical images. The presented parameters were obtained from analyzing at least 100 particles.

## 2.3 Results

### 2.3.1 Characterization of starting material

Milled and sieved polymer powders are utilized as the starting materials for the production of spherical particles. Figure 2.2(a) shows a thresholded image of such milled powder obtained for PS. The particle shape obtained after milling depends on the type of material, wherein brittle polymers produce more sharp edges in contrast to softer polymers. It has been shown that the type of milling process used can influence the shape as well [67]. For the initial sieving process, a mesh size of 500  $\mu\text{m}$  was used, hence the distribution of obtained particle sizes is below this range, as shown in Figure 2.2(b). Figure 2.2(c) shows the roundness  $R$  and circularity  $C$ , characteristic for the milled and sieved PS particles. As can be observed from Figure 2.2(c), the milled particles show a large distribution of shapes, ranging from sharp and elongated shapes resulting in low roundness and circularity values to almost spherical particles with values of roundness and circularity close to 1. An overall linear trend between roundness and the reciprocal aspect ratio as well as between circularity and roundness values can be seen, as expected by the fact that particle characteristics causing a reduction of aspect ratio also affect roundness and effects included in roundness also affect circularity. However, the large spread around this general correlation indicates a wide variability in the exact particle



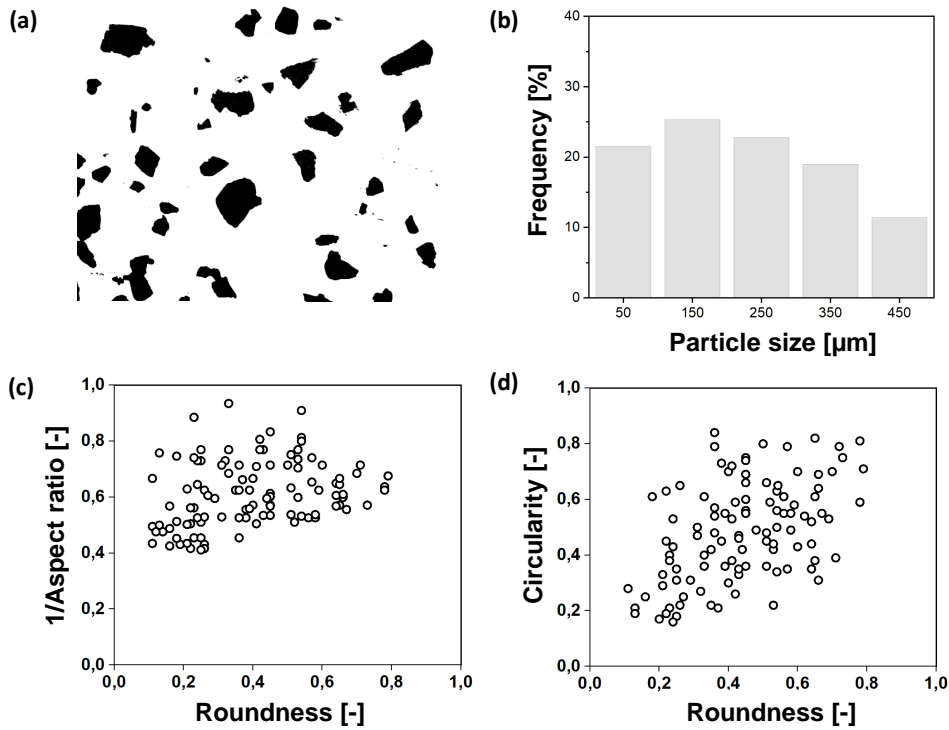


Figure 2.2: (a) Thresholded optical microscopy image (b) Particle size distribution (c) Shape factors roundness versus reciprocal aspect ratio, (d) Circularity  $C$  versus roundness  $R$  for milled PS powder sieved with a 500  $\mu\text{m}$  sieve.

surface shape, resulting in variations in the particle perimeter. Particles with a rough or uneven surface will hinder the flowability during powder spreading in the SLS process [68]. Therefore, the particle shapes should be modified to reach roundness  $R$  and circularity  $C$  values close to 1.

### 2.3.2 Optimization of process parameters

The initial particles are irregular and pointy in shape, thereby exhibiting a relatively large surface to volume ratio. If sufficient mobility is present, particles will tend to minimize their interfacial energy by reducing their interfacial area [69]. For the irregularly-shaped particles after milling, the process is expected to occur as shown in Figure 2.3. Since the interfacial stress increases with curvature, first retraction of pointy edges and protrusions will occur resulting in ellipsoidal particles. Subsequently, the ellipsoids will undergo shape retraction towards spheres. Hence, if the temperature is high enough to allow shape retraction and the residence time is long enough for completion of this process, full retraction will occur and spherical particles are created.

The most time-consuming step in this process is the last one, as this involves the smallest driving force (low curvature) and largest volume. The time required for an ellipsoidal

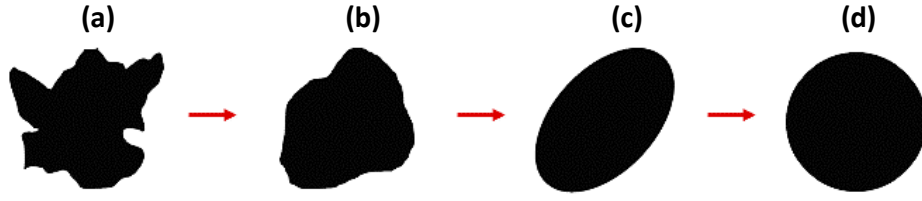


Figure 2.3: Schematic representation of a rough particle (a) undergoing deformation due to surface tension by retraction of protrusions and sharp edges (a-b), high curvature lobes (b-c) and retraction of the remaining ellipsoid (c-d).

Table 2.2: Estimated values of relaxation time for a droplet diameter of 500  $\mu\text{m}$ , at the chosen process temperature as indicated in Table 2.1.

Suspension	Viscosity ratio (-)	Interfacial tension (mN/m)	Relaxation time (sec)
PA12/ Rice Bran	$5.3 \cdot 10^4$	42.2	1.5
PS/ Rice Bran	$5.3 \cdot 10^4$	38.1	1.2
LDPE/ Rice Bran	$1.4 \cdot 10^7$	34.5	154
iPP/ Rice Bran	$2.7 \cdot 10^6$	29.6	44
PA12+CNT/Rice Bran	$2.1 \cdot 10^7$	39.3	206

droplet to retract to a sphere, can be estimated from the characteristic emulsion time [70]:

$$\lambda = \frac{n_m R (19p + 16)(2p + 3)}{\gamma_{12} 40(p + 1)}, \quad (2.6)$$

$$p = \frac{\eta_d}{\eta_m}, \quad (2.7)$$

where  $\lambda$  is the droplet retraction time to form a sphere,  $\eta_m$  is the matrix viscosity in Pa.s,  $\gamma_{12}$  is the interfacial tension in N/m and  $p$  is the viscosity ratio with  $\eta_d$  being the droplet viscosity. Due to disparities in polarity of the droplet and matrix, the surface tensions of the individual phases will determine the interfacial tension. Therefore, the interfacial tension at a given temperature can be estimated by [60]:

$$\gamma_{12} = \gamma_1 + \gamma_2 - \frac{4\gamma_1^d \gamma_2^d}{\gamma_1^d + \gamma_2^d} - \frac{4\gamma_1^p \gamma_2^p}{\gamma_1^p + \gamma_2^p}, \quad (2.8)$$

where  $\gamma_{12}$  is the interfacial tension,  $\gamma_i$  the surface tension of material  $i$  and  $\gamma_i^d$  and  $\gamma_i^p$  represent the dispersive and polar components of  $\gamma_i$  respectively. The dispersive and polar components for the rice bran oil and polymers were estimated from literature data [62, 71, 72]. The resulting interfacial tension values are listed in Table 2.2. With Eqn. 2.6 using known material properties, the relaxation times are calculated, for each system consisting of polymer droplets in rice bran oil at a fixed particle size.

Based on Table 2.2, the required annealing time depends on the polymer type, with the viscosity being the main factor. To optimize the process parameters for the generation

of spherical particles, the annealing time in the oil bath, the temperature of the oil bath and the volume fraction of particles in the oil bath were varied. The stirring speed was fixed at 30 rpm. Thereby, the estimation of the relaxation times in Table 2.2 were used as a guideline. For an optimal condition the stirring time chosen was at least 1.5 times the relaxation time for a 500  $\mu\text{m}$  particle. Figure 2.4 shows the effects process conditions can have on the obtained particle shape, for representative data on PA12 with 2 wt% CNT particles. Figure 2.4(a) demonstrates that after optimization of the process, perfectly spherical particles are obtained. The applied annealing time of 5 min at 260°C is in agreement with the estimated time required for retraction from the ellipsoidal to the spherical shape.

Temperature and residence time in the oil bath are critical to obtain spherical particles. Figure 2.4(b) and Figure 2.4(c) show examples of particles obtained with a too low residence time or a too low temperature. In Figure 2.4(b), the residence time was limited to 3 instead of 5 min whereas in Figure 2.4(c), the temperature was lowered to 240°C instead of 260°C. The former process conditions results in a residence time less than required for full shape retraction, whereas the latter process conditions increase the viscosity and thus the relaxation time to 382 s, whereby 5 min is no longer sufficient for shape retraction. Under these conditions, the initially irregular particles clearly do not undergo the full transition to the spherical shape. In Figure 2.4(b) and Figure 2.4(c), it can be observed that whereas large particles display remaining anisotropy, smaller particles have turned into spheres. This is caused by the direct proportionality between relaxation time and particle radius, as shown in Eqn. 2.6. Hence, a factor two reduction in particle size leads to a factor of two acceleration of the retraction process. Moreover, for the larger particles, it can be seen that most of the irregularities have smoothed and the remaining deviation from a sphere is the elongated ellipsoidal shape. This confirms the sequence of processes occurring during rounding, as proposed schematically in Figure 2.3.

Apart from optimizing the process conditions to facilitate the desired shape retraction dynamics towards the spherical shape, conditions are chosen as such that undesired droplet dynamics processes such as droplet breakup and coalescence are inhibited. The stirring speeds used are low and only aimed at avoiding sedimentation. Moreover, simple rotational stirring is used to avoid complex flow profiles in the beaker. Under these conditions, the suspensions undergo a rotational and shear flow. The ability of droplets to break up in shear flow is given by the Grace curve [73], which shows that breakup of droplets can only be achieved for viscosity ratios below 4 [73]. Based on the data in Table 2.1, this process is expected to be excluded here.

On the other hand, it is important to realize that the volume fraction,  $\phi$ , of the powder is an important criterion in determining the particle size distribution that can be achieved. With increasing  $\phi$  the probability of particles colliding becomes higher, which can further increase the probability of two or multiple particles coalescing together. Eqn. 2.9 shows the collision frequency  $c(t)$ :

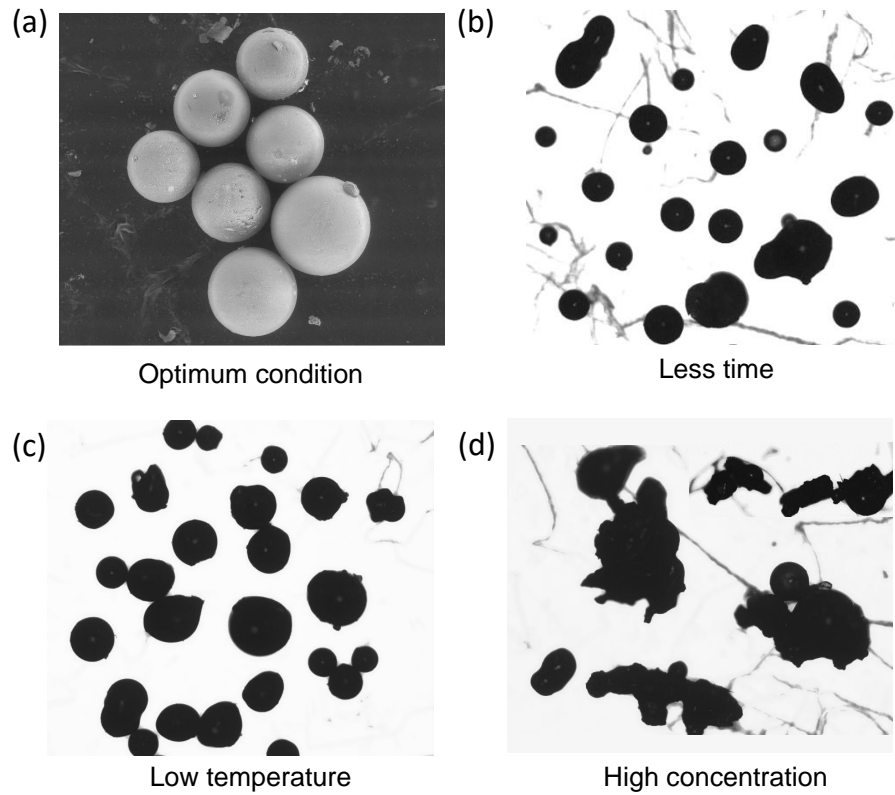


Figure 2.4: SEM (a) and Optical (b-d) images of PA12 particles with 2 wt% CNTs, fraction retained within mesh grid sizes of 75 and 300  $\mu\text{m}$ , (a)  $t_{\text{stir}} = 5$  min,  $\omega_{\text{stir}} = 30$  rpm,  $T = 260^\circ\text{C}$ ,  $\phi = 0.0002$  vol% (b)  $t_{\text{stir}} = 3$  min,  $\omega_{\text{stir}} = 30$  rpm,  $T = 260^\circ\text{C}$ ,  $\phi = 0.0002$  vol% (c)  $t_{\text{stir}} = 5$  min,  $\omega_{\text{stir}} = 30$  rpm,  $T = 240^\circ\text{C}$ ,  $\phi = 0.0002$  vol% (d)  $t_{\text{stir}} = 5$  min,  $\omega_{\text{stir}} = 30$  rpm,  $T = 260^\circ\text{C}$ ,  $\phi = 0.0006$  vol%.

$$c(t) = \frac{24\phi^2\dot{\gamma}}{\pi^2(2R_p)^3}, \quad (2.9)$$

as a function of the volume fraction  $\phi$ , the radius of the particle  $R_p$  and the shear rate  $\dot{\gamma}$ .

This equation assumes that the initial particle size is monodisperse and neglects effects of hydrodynamic interactions on the collision. The shear rate can be estimated from the velocity of the stirrer and taking the relevant length scale for the decay of the velocity to zero as the distance between the stirrer and the vessel wall. This results in a value of 0.5/s at 30 rpm. Hence, a collision frequency of 486 /( $\text{s}\cdot\text{m}^3$ ) is obtained. This means that within the volume of the vessel, approximately one collision occurs every 50s, under the optimized processing conditions. Figure 2.4(d) illustrates the need to keep the collision frequency low. The particles in Figure 2.4(d) were obtained when 3 mg instead of 1 mg of polymer powder is added to 50 ml rice bran oil (0.0006 vol% versus 0.0002 vol%). According to Eqn. 2.9 this results in a factor nine increase of the collision frequency

and Figure 2.4(d) clearly illustrates the resulting bigger particles and particle clusters. These bigger particles on the one hand require a longer time to undergo shape retraction. On the other hand, ongoing coalescence events at the end of annealing result in particle clusters with complex shape dynamics. Figure 2.4(d) illustrates the presence of irregularly shaped clusters resulting from these processes.

Apart from the particle concentration, also the stirring speed is related to the collision frequency, whereby too rigorous stirring (high shear rates) results in excessive amounts of collisions. However, the dependence is only linear rather than quadratic and moreover, with increasing shear rate, the interaction time during collision also reduce. As a result the percentage of collisions that will effectively result in coalescence will also reduce. Therefore, we noticed that the stirring speed is a less crucial process parameter as compared to the particle concentration. Nevertheless, Eqn. 2.9 allows to estimate how  $\phi$ ,  $R_p$  and  $\dot{\gamma}$  combined affect the collision frequency and can be used to have more control over the process. In addition, the annealing time becomes relevant as well since under given conditions, the total amount of collisions increases proportionally with the residence time. Therefore, temperatures are chosen as such that maximum a few minutes of annealing is required.

Finally, it should also be noted that immediate quenching of the particles after annealing is crucial in maintaining sphericity. This way further collisions with neighbouring particles at high temperature are minimized, thereby reducing the probability of coalescence. Figure 2.4(b) shows some examples of particles that were coalescing while being quenched.

From the process optimization it can be concluded that for generation of spherical particles an interplay between the matrix temperature, annealing time, stirring speed and particle concentration should be taken into account. The rationalization of the process parameters, as illustrated in this section for PA12 with 2 wt% CNTs, can be used to make a priori estimates of the required process parameters for other polymers. The relevant parameters for other polymers used are provided in Table 2.1.

### 2.3.3 Control over the particle size distribution

For the optimized process conditions, particles were segregated based on their diameter using consecutive meshes with well-defined grid sizes. The system is shown in Figure 2.1, and can easily be implemented on larger scale. To characterize the particle shape, SEM images were utilized. Figure 2.5 shows the particle size distribution and SEM images obtained for PA12 polymer particles. For this system, the temperature could be lowered to 210 °C (which is 40°C above  $T_m$ ) while maintaining an annealing time of 3 min. Almost perfectly spherical particles were obtained under the defined process conditions, for all particle sizes. Similar to the starting material, a uniform particle size distribution is obtained. It should be noted here that the amount of particles retained on the sieve with the largest mesh size was negligible. Therefore, it can be concluded that conditions

are indeed tailored as such that coalescence is avoided and as a result the yield of the method is close to 100%.

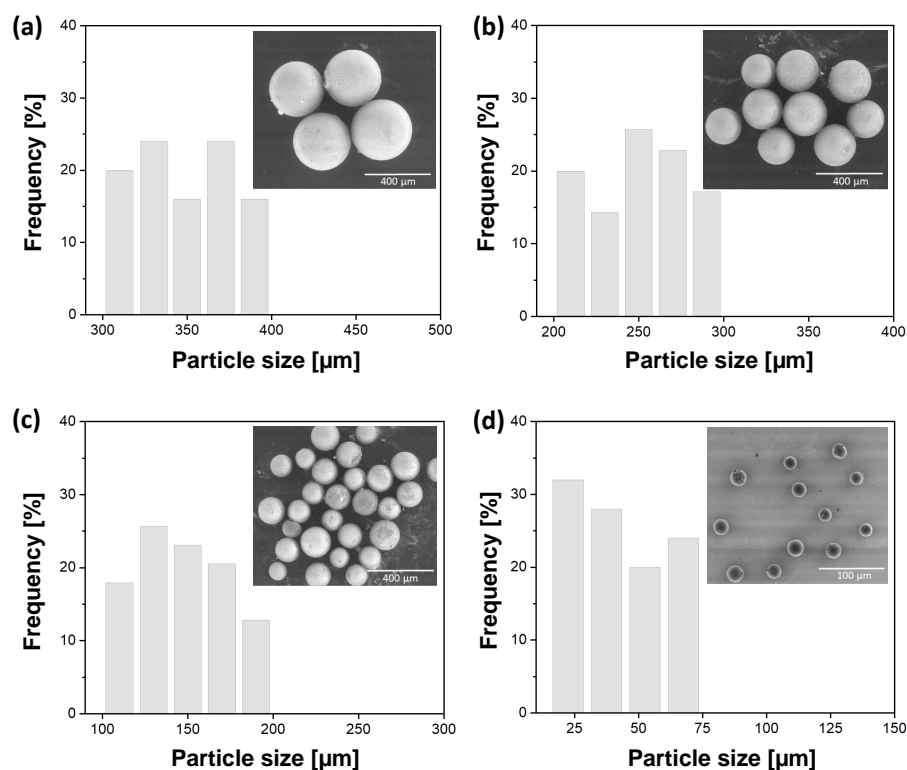


Figure 2.5: Particle size distribution and SEM images of PA12 polymer particles obtained from mesh grid sizes (a) 400 μm to 300 μm (b) 300 μm to 200 μm (c) 200 μm to 75 μm and (d) 75 μm to 10 μm. Refined powder of PA12 was added to rice bran oil kept at 210°C, and stirred for 3 minutes at 30 rpm before quenching it.

For many applications, it is of interest to obtain a narrower particle size distribution. This parameter can easily be regulated by narrowing the range between consecutive mesh grid sizes. As an example set, powder of PS was added to rice bran oil kept at 130°C, which is 90°C above  $T_g$ , and stirred for 2 minutes at 30 rpm before quenching it. The influence of grid size range can be observed for the obtained PS particles from Figure 2.6(a) and Figure 2.6(b), for a grid size ranging between 200 μm to 75 μm and 180 μm to 120 μm respectively.

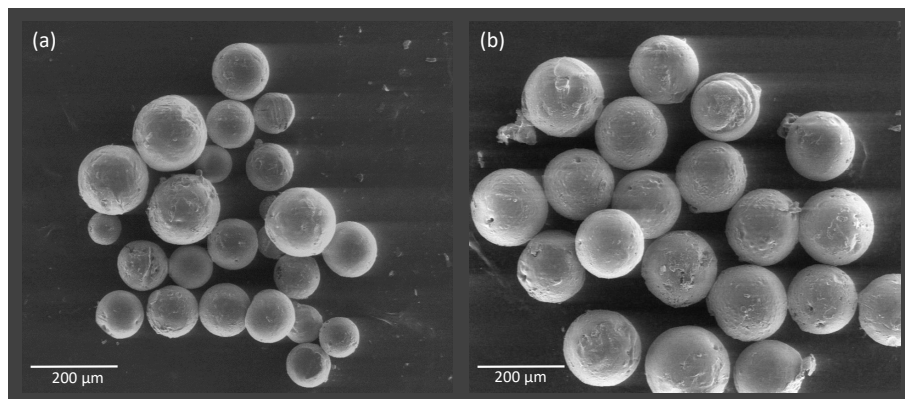


Figure 2.6: SEM images of PS polymer particles obtained from mesh grid sizes (a) 75  $\mu\text{m}$  to 200  $\mu\text{m}$  (b) 120  $\mu\text{m}$  to 180  $\mu\text{m}$ .

This can be confirmed from the particle size distribution, as shown in Figure 2.7. By narrowing the grid size, particles with sizes within the consecutive grid size can be contained, thereby reducing the polydispersity as can be seen from Figure 2.7(b).

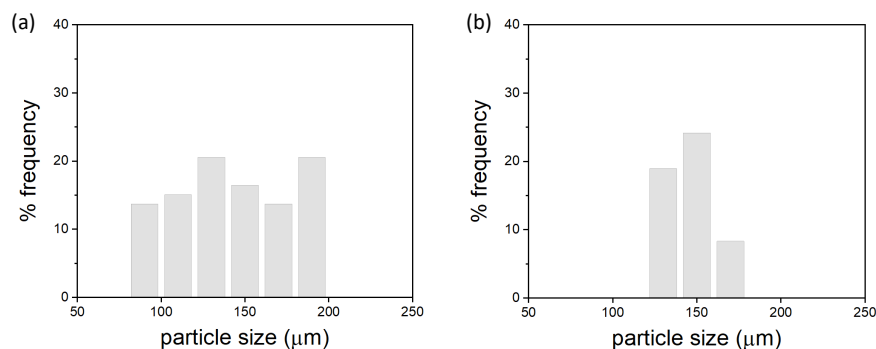


Figure 2.7: Particle size distribution of PS polymer particles obtained from mesh grid sizes (a) 75  $\mu\text{m}$  to 200  $\mu\text{m}$  (b) 120  $\mu\text{m}$  to 180  $\mu\text{m}$ .

### 2.3.4 Characterization of spherical particles from various thermoplastic polymers

Based on the information gathered in Section 2.3.2 concerning the mechanisms of shape retraction and possible simultaneous dynamic processes such as sedimentation and coalescence, optimal process conditions were established for a range of thermoplastic polymers. As summarized in Table 2.1, the annealing temperature was adjusted to ensure shape relaxation within a maximum of a few minutes. For the optimized process conditions, irrespective of the polymer type, spherical particles were generated, as demonstrated in Figure 2.8. Similar results were obtained for PS, PA12, PA12 with 2 wt% CNTs, LDPE and PP. Apart from the spherical shape, the particles in Figure 2.8(a-d) show an exceptionally smooth surface, whereas the PP particles in Figure 2.8(e) have rougher surface in comparison. This could be attributed to the high degree of crystallinity of PP [74],



which during sudden quenching can lead to shrinkage resulting in a rough surface.

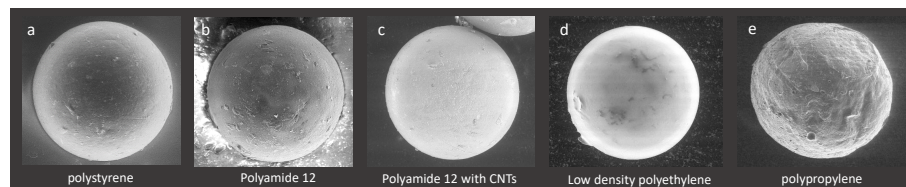


Figure 2.8: SEM images of spherical particle of 300  $\mu\text{m}$  diameter obtained from different classes of thermoplastic polymers.

To demonstrate the particle characteristics in a more quantitative manner, Figure 2.9 shows the shape factors obtained for the different thermoplastic polymers. Irrespective of the particle size and particle type both the aspect ratio as well as the circularity value are close to 1 which defines the nearly perfect spherical shape of the produced particles. However, Polypropylene tends to show a consistently higher standard deviation in comparison to the other thermoplastics tested. This larger variability corresponds to the larger roughness and irregularity of the particle surface, as demonstrated in Figure 2.8(e).

Figure 2.9(b) summarizes the overall result of this work for the representative case of PS, clearly demonstrating that particles starting from the complete range of circularity and roundness values can be reshaped to nearly spherical particles. Rounding of raw material in a downer reactor [75] has been shown to shift the overall sphericity (= surface area of volume equivalent sphere relative to actual particle surface area) of the initial raw material from an average value of 0.4 to close to 1. However still retaining a clear distribution in sphericity values between 0.2 and 1. In addition, it appeared to be impossible to fully avoid agglomeration during the rounding process [76].

For applications like selective laser sintering, the shape of the polymer powder is one of the bottlenecks restricting the technology to a handful thermoplastic polymers, thereby limiting its potential [4]. Particle shape and morphology can dictate the flowability and eventually obtained packing density of the powder bed, which have a direct influence on the final part density [77, 78, 79, 80]. The smooth surface morphology as well as levels of roundness and circularity achieved in this work with one singular processing method applicable for a wide range of thermoplastic polymers has not yet been shown before. These results show that this process is well suited to produce spherical particles with shape and size that can match the commercial requirements. Using this particle preparation method, we have produced spherical PS particles, PA12 particles and PA12 particles with CNTs that were laser sintered in our home-build laser sintering setup [81, 82].



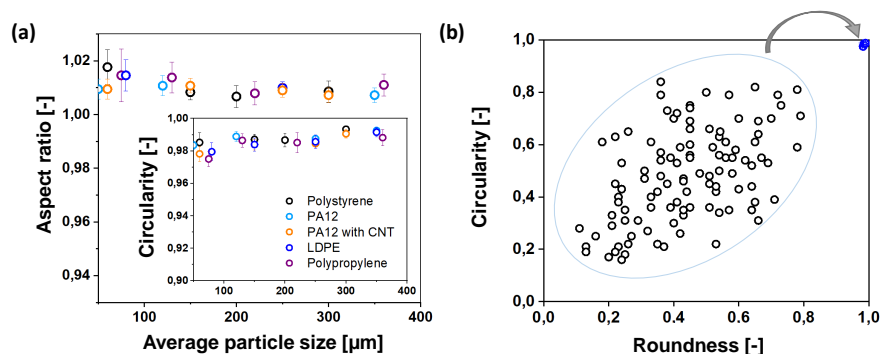


Figure 2.9: (a) Plot showing the shape factor values as a function of the particle size for different classes of thermoplastic polymers. (b) Circularity versus roundness of rough PS particles obtained after milling in comparison to PS particles obtained after the optimized annealing process.

## 2.4 Conclusions

Compared to conventional set of methods, we describe an economic method to obtain spherical particles from thermoplastic polymers. This methodology is developed to obtain spherical particles from different classes of thermoplastic polymers, showing the versatility of the method. The method is based on the shape retraction of liquid droplets. Randomly shaped powder particles are transformed to a spherical shape. To reduce polydispersity, particles are fractionated within meshes with well-defined grid sizes. The final particle shape depends on the interplay between the material characteristics and the processing conditions. Optimization of the process is possible by considering the time required for shape retraction and aiming at reducing undesired droplet dynamics processes such as droplet breakup, droplet collision and coalescence and droplet sedimentation. The temperature is crucial to shift the characteristic shape relaxation time within a timeframe that largely excludes particle interactions. Moreover, close control over the particle volume fraction further eliminates particle interactions. Based on an analysis of the relevant phenomena and their scaling relations, guidelines for process conditions are presented. As a result, for any thermoplastic polymer, the relevant processing parameters can be defined a priori. A comparison of shape factors between the starting material and particles after the rounding process shows the versatility and potential of the method. Altering the processing conditions can be used to generate particles with a certain aspect ratio, which is sometimes desired to enhance packing in for instance SLS [83, 84]. Thereby, the proposed method combines advantages of the heated downer reactor and the melt emulsification techniques that started to receive attention lately. Similar to the former method, the particle size is largely retained and process optimization can be done a priori without trial-and-error tests. Similar to the later technique, the required equipment is standard lab equipment. Considering the potential of this methodology, future work focus on upscaling of the method for continuous mass production, which brings up challenges of its own.

## Acknowledgements

This work forms part of the research program of the Brightlands Materials Center (BMC). We acknowledge the assistance of Lucien C. Cleven with machining the parts required for this work. We are thankful to Prof.dr.ir. Leon E. Govaert and Prof.dr.ir. Gerrit W. M. Peters for providing us with polymer materials.



## A novel experimental setup for *in-situ* optical and X-ray imaging of laser sintering of polymer particles

### Abstract

We present a unique laser sintering setup that allows real time studies of the structural evolution during laser sintering of polymer particles. The device incorporates the main features of classical selective laser sintering (SLS) machines for 3D printing of polymers, and at the same time allows *in-situ* visualization of the sintering dynamics with optical microscopy as well as X-ray scattering. A main feature of the setup is the fact that it provides local access to one particle-particle bridge during sintering. In addition, due to the small scale of the device and the specific laser arrangement process parameters such as temperature, laser energy, laser pulse duration and spot size can be precisely controlled. The sample chamber provides heating up to 360°C, which allows for sintering of commodity as well as high performance polymers. The latter parameters are controlled by the use of a visible light laser combined with an acousto-optic modulator for pulsing, which allows small and precise spot sizes and pulse times and pulse energies as low as 500  $\mu\text{s}$  and 17  $\mu\text{J}$ . The macrostructural evolution of the particle bridge during sintering is followed via optical imaging at high speed and resolution. Placing the setup in a high flux synchrotron radiation with a fast detector, simultaneously allows *in-situ* time-resolved X-ray characterizations. To demonstrate the capabilities of the device, we studied the laser sintering of two spherical PA12 particles. The setup provides crucial real-time information concerning the sintering dynamics as well as crystallization kinetics, which was not accessible up to now.

---

*Largely reproduced from:*

1) Hejmady, P., Cleven, L. C., van Breemen, L. C. A., Anderson, P. D., & Cardinaels, R. (2019). A novel experimental setup for in situ optical and X-ray imaging of laser sintering of polymer particles. *Review of Scientific Instruments*, 90(8), 083905.

### 3.1 Introduction

Laser sintering (LS) of polymer powders, also known by its trade name selective laser sintering (SLS), is an emerging 3D printing technology, by which complex parts are manufactured layer-by-layer [4, 23, 85, 86, 87]. In SLS, polyamide 12 (PA12) is the most commonly used polymer due to their large sintering window [25]. Though this technique receives significant interest from industry as well as academia [88, 89, 90], the final products often suffer from poor mechanical properties. Due to limited control over the process parameters as well as incomplete insights in the relations between process conditions and structure development during laser sintering, the final products cannot be produced with tailored and reproducible structural/mechanical properties [14]. Moreover, porosity, poor layer-to-layer adhesion and dimensional inaccuracy are some of the commonly found defects in such SLS printed parts [12]. While there are ample studies showing the effects of laser sintering on the microstructure, crystalline morphology and mechanical properties of polymers, they are all limited to post-mortem characterization techniques thus lacking information on the actual structure development [91, 92]. Since shape evolution and crystallization kinetics during laser sintering are complex and coupled processes involving non-isothermal, non-homogeneous temperature profiles and complex flow fields, studies with high temporal and spatial resolution are required to provide fundamental insights in the effects of processing conditions on the microstructure development during laser sintering.

Hot stage microscopy has been a convenient technique to observe coalescence of two polymer particles [93] during and after heating, and to validate analytical models describing sintering dynamics [94, 95, 96]. Although this technique is suitable to study traditional polymer processing operations such as rotational moulding, it misses several aspects typical for laser sintering. In laser sintering, the laser pulse causes fast heating followed by cooling, the speed of which is essential for the sintering kinetics [97] but also for the melting and crystallization of the polymer. In addition, the heat distribution in the particles due to the laser is not uniform, which can lead to partial melting and further affects the flow, and therefore the structure development within the particles [2]. To investigate polymer structure, X-ray diffraction is a powerful and widely used technique [98]. Ex-situ X-ray diffraction and scattering experiments have been utilized to study the crystalline microstructure within SLS printed parts [99], but studies on time dependent microstructure developments that take place during the process are not available. For traditional polymer processing operations such as extrusion or injection moulding, custom-designed setups have been developed that can incorporate high flux synchrotron radiation to allow for *in-situ* time resolved X-ray studies of polymer crystalline morphology development [100, 101, 102]. Moreover, for extrusion additive manufacturing it was recently shown that *in-situ* characterization of the extruded material via infrared thermography and Raman spectroscopy can provide valuable information about the weld formation and crystallisation kinetics during extrusion additive manufacturing.[103, 104] Recently, laser sintering of metals has been studied *in-situ* and time-resolved by means of X-rays[105, 106], but these studies were concentrated on using X-ray attenuation to study powder motion, melting and melt dynamics in a bed of metal powder. Zhao et

al. used time-resolved X-ray diffraction to study the kinetics of the phase transformations of  $\alpha$ - $\beta$  Titanium Alloy (Ti-Al-4v) upon solidification, using a spot size around five times bigger than the particle size and targeting a metal powder bed [107]. However, up to now, experimental setups allowing to provide real time information on the melting dynamics and crystallization kinetics during sintering of polymers as well as setups targeting single particle pairs are not available. Intrinsically transient processes like laser sintering pose many challenges in building such a system, which should incorporate the main features of an SLS machine and at the same time should allow optical visualization and X-ray scattering/diffracton characterization. Recently, we have developed a setup that allows optical visualization of laser sintering and have studied laser sintering of amorphous polystyrene [81]. In the present work, we present an experimental setup that not only enables us to study laser sintering of polymer particle doublets with precisely controlled sintering parameters, but also enables *in-situ* X-ray characterization thereby providing access to the polymer internal microstructure development during sintering.

## 3.2 Design and description

The key feature of the experimental setup is the ability to precisely control the laser impact energy at the interface of two polymer particles while simultaneously visualizing the sintering process optically and performing *in-situ* X-ray experiments. This gives us the exclusive advantage to be able to track the dynamics and kinetics of macro- and microstructure development during the sintering process, which is not possible in commercial SLS machines. Figure 3.1 shows the layout of the experimental setup as arranged in the beamline. The polymer particle pair to be sintered is placed in the sample chamber, which allows for X-ray access via the side windows and optical visualization as well as laser entrance from the top. The main components of the setup namely the laser, the sample chamber and the imaging system are discussed in more detail in the following sections.

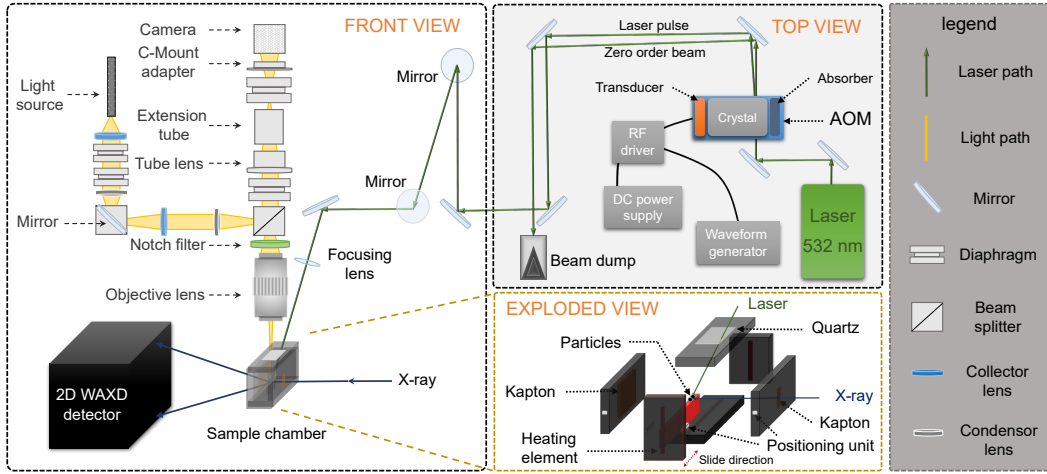


Figure 3.1: Schematic representation of the experimental setup with *in-situ* X-ray scattering/diffraction capability. Front and top view represent the visualization and laser systems respectively, which were arranged on a 600 mm x 600 mm optical table. The exploded view of the sample chamber shows the particle substrate.

### 3.2.1 Laser

A visible-light laser is used, as this allows a more precise control over the laser power and facilitates lower power values as compared to CO<sub>2</sub> lasers, which are used in classical SLS machines. In addition, the smaller wavelength enables smaller laser spot sizes. High power stability, low beam divergence and a high quality factor  $M^2$  are essential to be able to focus the laser beam to the desired spot size and to ensure precise control over the laser impact energy. In our setup, we use a Genesis MX STM from Coherent, which is a continuous wave (CW) laser of 532 nm wavelength with a spatial TEM<sub>00</sub> mode, which provides a Gaussian intensity distribution. The beam waist diameter is 2 mm with a beam divergence of  $< 0.7$  mrad and a beam quality factor,  $M^2 < 1.1$ . The output power ranges between 0.02 mW and 2 W with a beam stability within 2%. Diverting the laser through the objective lens used for visualization limits the final spot size achievable. Furthermore the peak intensities of the laser pulse exceed the damage threshold limit of the infinity corrected objective. Hence, the laser is sent directly next to the objective lens under the minimum possible incidence angle with respect to the objective lens ( $30^\circ$ ). By using focusing lenses with different focal lengths, the final spot size of the laser beam can be varied as [108]:

$$D_s = \frac{1.27 \cdot M^2 \cdot \lambda \cdot f}{D_l}, \quad (3.1)$$

where  $M^2$  is the laser beam quality factor,  $\lambda$  the wavelength,  $f$  the focal length of the lens and  $D_l$  the beam waist diameter of the laser. For *in-situ* experiments we use a focusing lens with a focal length of 100 mm. By tight focusing we achieve a final spot diameter of 40  $\mu\text{m}$ , whose size was verified by optical imaging and corresponds to the value predicted by Eqn. 3.1. To simulate the limited laser-impact time on the sample

during actual SLS processes due to the fast movement of the laser over the powder bed, the laser is pulsed with a well-defined pulse length as well as pulse energy. To do so, the beam path of the continuous wave laser is diverted using mirrors (Altechna HR laser line mirror, reflectivity: 99.5%), through an acousto-optic modulator (AOM) from Isomet, which has an aperture of 2 mm and maximum modulation frequency of 30 MHz. In single pulse-mode, pulses as short as 500  $\mu\text{s}$  can be sent with a minimum rise and fall time of 360 ns. AOM's are primarily used to control laser beam intensity, and their main components are a piezo-electric transducer, a crystal and an absorber. By switching on and off the modulation within the AOM, the output intensity can be controlled by redirecting part of the laser beam to a beam dump. To generate the modulation signal, the AOM is connected to an RF driver (Isomet) which in-turn is connected to a DC power source (Basetech) and waveform generator (Keysight 33500B). Via the waveform generator and RF driver, any arbitrary waveform can be supplied to the piezo-electric transducer, which generates an acoustic wave in the crystal. The absorber damps the RF signal such that secondary waves due to reflection are suppressed. Due to the photo-elastic effect, areas of compression and densification are created in the crystal bulk, which provides a single pulsed first order beam under an angle of  $0.7^\circ$  with respect to the zeroth order continuous wave beam. The former is then diverted to the sample chamber and the later to the beam dump, as schematically shown in Figure 3.1. With a known laser output power, which is measured using a Gentec XLP12 thermopile, and a known waveform signal supplied, single pulses with energy values ranging from a minimum of 17  $\mu\text{J}$ /pulse upto a maximum of 0.5 J/pulse can be sent. The laser pulse energy is measured using a Gentec QE12, which is a pyroelectric based energy meter with a precision of 0.5  $\mu\text{J}$ .

### 3.2.2 Sample Chamber

Another important feature of the setup is the heating chamber with a sample substrate which has been designed to meet the requirements on temperature accuracy and homogeneity. Furthermore, it allows to perform *in-situ* optical and X-ray measurements. The sample substrate (1 mm thickness) consists of mirror polished steel (roughness of 100 nm) to eliminate spurious reflections in the optical images. Furthermore, its width along the X-ray direction is minimized to avoid interference with the incoming or outgoing scattered X-ray beam. To facilitate the placement of the sample, the substrate is connected to one of the sides of the sample chamber which can be opened and closed by means of the rail slider and positioning units, as illustrated in Figure 3.1. The sample chamber (32 mm x 70 mm x 32 mm) has a 3 mm thick quartz window (17 mm x 13 mm) on top that allows entering of the laser beam and optical visualization via an objective lens. Moreover, two side walls contain 0.025 mm thick Kapton windows to allow for entrance (2 mm x 10 mm) and exit (15 mm x 15 mm) of X-rays (Figure 3.1). The sample to window distance on the scattering side was taken as small as possible (0.8mm), thereby facilitating  $2\theta$  scattering angles up to  $45^\circ$ , which is large enough to capture the main crystallization peaks of all common polymers. The chamber is built from aluminum with a wall thickness of 6 mm. An enclosure of low thermal conductivity (0.4 W/(m·K) at  $400^\circ\text{C}$ ) around the box minimizes heat loss to the environment. Based on a heat analysis



of the sample chamber including conduction and free convection to the environment at 25°C a heat loss of 17.9 W was estimated at a sample chamber temperature of 360°C. For heating, the side walls of the chamber as well as the bottom plate contain heating rods (three rods with length 60 mm and diameter 6 mm, 100 W) which provide sufficient heating power. In addition, K-type thermocouples (RS Pro,  $\pm 1^\circ\text{C}$  accuracy) are integrated in the sample chamber to measure substrate and air temperature. Heating rods and thermocouples are connected to a temperature control unit (Hasco), which allows to regulate the temperature of the substrate and the air independently. Simultaneously, air and substrate temperature are monitored using calibrated voltcraft thermometer with K-type thermocouple. This allows to maintain the sample temperature within  $\pm 0.6^\circ\text{C}$  up to the maximum operating temperature of 360°C. These specifications ensure that common polyolefins as well as engineering plastics such as PEEK can be sintered within the heating chamber. Based on the thermal mass of the sample chamber, a maximum heating rate of 25°C/min can be obtained with the heating rods. Temperature overshoots from the desired set-point are avoided using PID control (Eurotherm).

### 3.2.3 Optical imaging system

Given the thin interface between the two polymer particles at the initial stages of sintering and the large curvature effects that dominate the coalescence process during sintering, the imaging system needs to provide adequate resolution. However, due to the high temperature of the sample chamber heat loss from the sample chamber can heat up and expand the lenses within the objective lens (maximum working temperature of 65°C) which can cause optical aberrations. This limits the usage of objective lenses with a high numerical aperture or low working distance. Moreover, sintering is a fast dynamic process, requiring minimum image acquisition times on the order of 50 ms, depending on the polymer type used. In order to fulfill these requirements and maintain geometrical flexibility for placement in the beamline, we custom designed the optical train for imaging. Figure 3.1 illustrates the individual components of the optical train which mimics the architecture inside a microscope. The main components of the optical train are an infinity corrected Mitutoyo 20x objective lens (NA 0.28, working distance 30 mm) and a Pixelink (PL-D725MU-T) CMOS camera with 1 inch sensor size (2592 x 2048 pixels), which can capture images at 75 frames per second in full resolution. By reducing the region of interest, frame rates can be further increased. The objective lens is corrected for aberrations with a glass sample cover with a thickness of 3 mm, which corresponds to the thickness of the quartz glass in the sample chamber. This combination of high camera resolution and objective lens allows to capture images with 4.3 pixels/ $\mu\text{m}$ , which suffices for the length scales we are interested in. Moreover, no image distortions are observed while imaging at 360°C sample chamber temperature. Besides the main components, the optical train contains several auxiliary components. Right above the objective a notch filter (center wavelength  $532\pm 2$  nm, Thorlabs) is placed to exclude reflected laser light from the optical train, which would otherwise lead to overexposure of the camera and hamper imaging. The tube lens used to focus the image on the camera is a bi-convex lens with a focal length of 200 mm, which equals the focal length of a Mitutoyo tube lens. This lens is placed in a zoom housing which provides a vertical translation of 4 mm

with a precision of 0.5 mm per revolution, allowing to optimize image focusing. A 50:50 beam splitter is positioned between the tube lens and the objective lens which facilitates simultaneous illumination and imaging through the objective. Illumination is provided by a 150 W halogen light source (Intralux 6000) with intensity control knob, through a flexible optic cable. The cable is connected to the tube with two diaphragms as well as two collector and two condenser lenses to provide sufficient light intensity. A mirror at 45° diverts the collimated light source into the beam splitter. In addition to this, the main body of the imaging system (above the tube lens) consists of two diaphragms which reduce internal reflections within the tubing which would otherwise cause image distortions. Furthermore, a tube system is placed to position the camera at a suitable distance of the bi-convex lens considering its focal length. The imaging setup is attached to a micromanipulator with a lateral resolution of 0.25 mm per revolution, for fine adjustments along the vertical direction.

### 3.2.4 Placement in the beamline

The complete setup, as schematically depicted in Figure 3.1, is placed in the BM26 (DOUBLE) beamline at ESRF, in Grenoble (France) to perform wide-angle X-ray diffraction experiments[109]. Figure 3.2(a) shows the setup mounted in the beamline, with the main components indicated. An imaginary laser path (green line) is indicated as a guide to the eye. The sample chamber is mounted on a PI M-111 x-y-z micromanipulator stage with 1  $\mu\text{m}$  minimal incremental steps and 15 mm travel range, along all directions. This allows alignment with respect to the incoming X-ray beam. The inset picture in Figure 3.2(b) shows a close-up of the sample chamber with the laser and X-ray paths indicated. To achieve a high signal to noise ratio, a metallic cone under vacuum is attached in front of the detector, such that the scattering from the air can be reduced. A synchrotron beam of 100  $\mu\text{m}$  x 100  $\mu\text{m}$  was achieved on the sample interface, using a JJ X-ray slit system. This beam size reduction method is the best compromise between maintaining sufficient intensity and focusing on the main sintering area. The wavelength of the X-rays was 0.9799 Å and the sample to detector distance was 409 mm. The sample-detector distance and tilt angle were calibrated using AgBe (silver behenate) for the WAXD experiments. We used a Pilatus 300K detector with a pixel size of 172  $\mu\text{m}$  x 172  $\mu\text{m}$ . Thereby a minimum exposure time of 0.3 s could be achieved. Considering the typical crystallization times, this acquisition time provides an optimal balance between signal-to-noise ratio and time resolution. This setup provided access to scattering vectors  $q$  up to 23  $\text{nm}^{-1}$ , which corresponds to characteristic length scales ranging down to 0.28 nm. The Fit2D software[110] developed by the European Synchrotron Radiation Facility was used to analyze the 2D WAXD data. The acquired images were corrected for background noise and the beamstop as well as traces of the direct beam were masked.

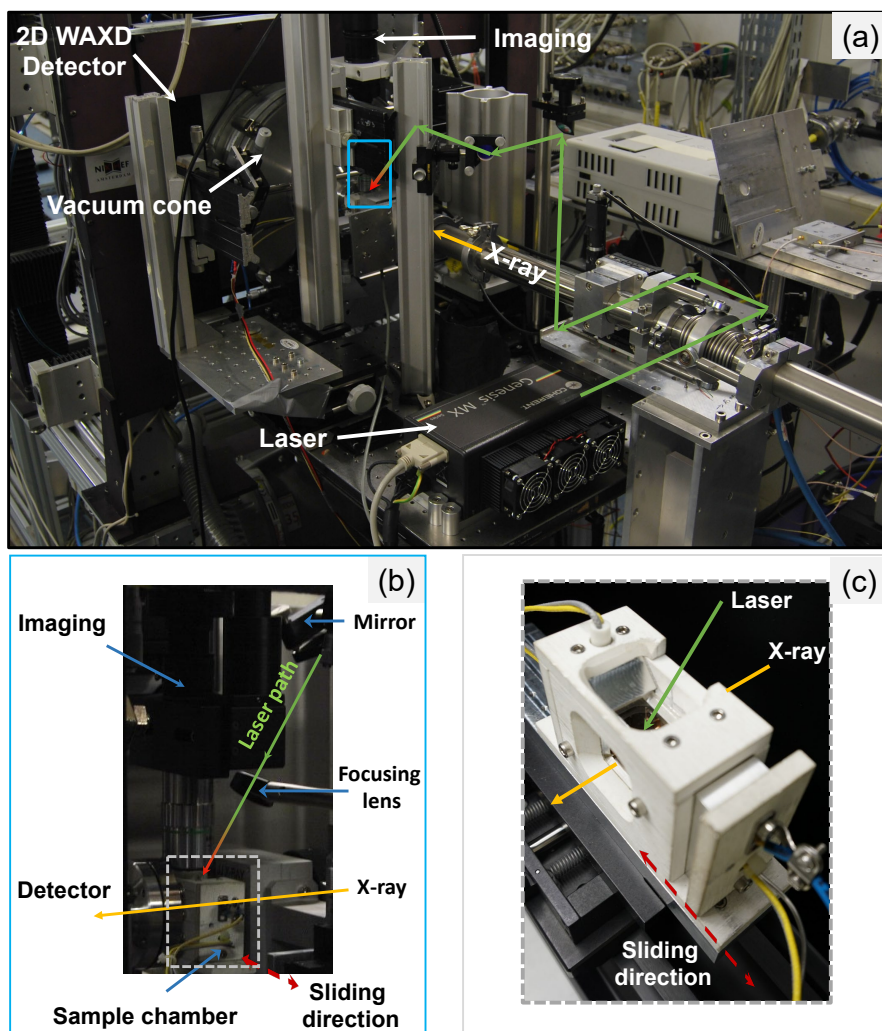


Figure 3.2: Photograph of the experimental setup installed in the BM26 beamline at ESRF. (a) The setup is mounted on a x-y-z translator for positioning relative to the 2D WAXD detector and incident X-ray beam. (b) Inset picture shows the sample chamber with objective lens and vacuum cone. (c) Sample chamber.

### 3.3 Experimental procedure

#### 3.3.1 Material

In our experiments we use spherical particles prepared from PA12 (Vestamide L-1700), which is free of flow and other additives. Before particle preparation, Nubian black dye (2 wt%) was added to the PA12 via solution mixing in benzylalcohol at 120°C. Addition of dye resulted in an absorption of 91% for visible light at 532 nm and a sample thickness of 100  $\mu\text{m}$ . This enables the laser to locally heat up the sample and cause melting of the polymer particles allowing laser sintering. This PA12 with dye has a peak melting temperature  $T_m$  of 178°C and melting enthalpy of 56.4 J/g (as determined by differential scanning calorimetry at 5°C/min). To determine the half-time of crystallization ( $t_{1/2}$ ), a

specific thermal protocol was utilized by means of differential fast scanning calorimetry (FDSC) [111]. From the endothermic peak of melting after crystallization for varying isothermal times, the normalized enthalpy of fusion is plotted as a function of annealing time [111, 112]. For PA12 with dye at 155°C, the  $t_{1/2}$  is evaluated to be 19.5 s.

Viscosity plays an important role in the sintering dynamics. The zero-shear viscosity,  $\eta_o$  is used as the main rheological parameter to determine the temperature-dependent flow behaviour. To determine  $\eta_o$ , rheological measurements were performed on a stress-controlled rotational rheometer (MCR502 from Anton Paar) with a plate-plate geometry (diameter 25 mm). Measurements were carried out in the linear viscoelastic regime, which was determined by a strain sweep test (at 1 Hz). At sufficiently high temperatures above the glass transition and melt temperature of the polymer, the viscosity of most polymers is known to show an Arrhenius dependency with respect to temperature, given by [113]:

$$\eta = \eta_{\text{ref}} \cdot \exp\left[\frac{E_a}{R \cdot T}\right] \quad (3.2)$$

where  $\eta$  is the viscosity,  $E_a$  the activation energy,  $R$  the universal gas constant,  $T$  the temperature and  $\eta_{\text{ref}}$  the pre-exponential factor.

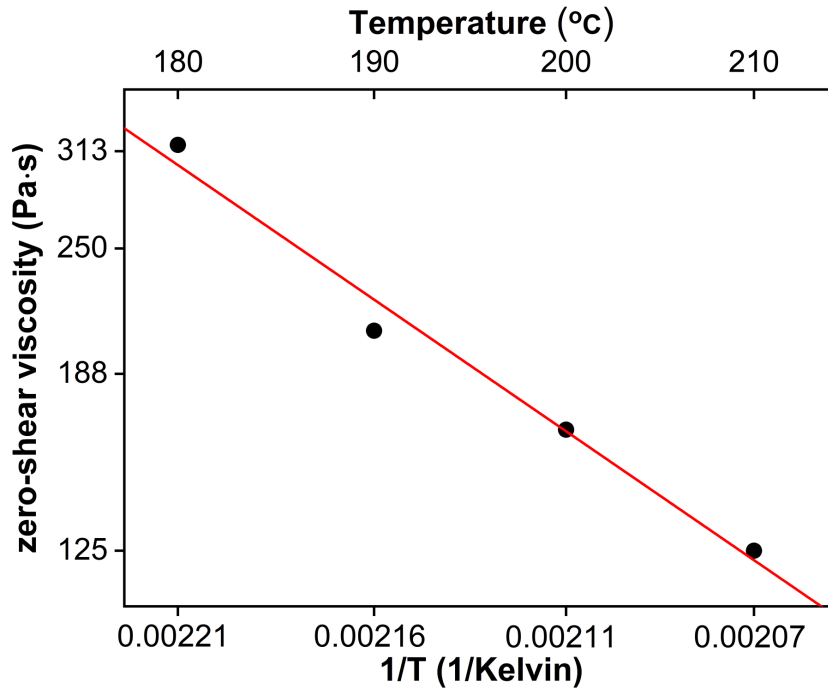


Figure 3.3: Arrhenius plot for zero-shear viscosity versus temperature. Symbols are experimental data, line is a fit with Eqn. 3.2.

Figure 3.3 shows the zero-shear viscosity data of PA12 with 2 wt% black dye at four different temperatures fitted with the Arrhenius equation. An activation energy  $E_a = 32.5$  kJ/mol was obtained, which is close to literature values for PA12, despite the difference in molecular weight [114]. The viscosity at 210°C is 125 Pa·s. The surface tension  $\Gamma$ , of PA12, which is relevant for the sintering process, is equal to 34.3 mN/m [115]. Finally, the thermal conductivity  $k$  is 0.12 W/(m·K) [116] and the heat capacity  $c_p$  is 1200 J/(kg·K), as determined from DSC measurements.

### 3.3.2 Micromanipulation of polymer particles

To perform sintering experiments, two polymer particles of the same size placed adjacent to each other, with their interfaces being in contact, are required. For this, it is important to be able to manipulate polymer particles irrespective of their size and polymer type. We have developed a manipulation technique that allows to pick and place such polymer particles, in a non-destructive manner. Thereto, the sample substrate from the sample chamber is placed in a home-built particle manipulation setup, as shown in Figure 3.4. The main components are a horizontal optical train and a manipulation probe connected to a voltage source. Each component is mounted on an x-y-z manipulator, and can thus be positioned individually. The imaging system is similar to the one described in Section 3.2.3. The illumination mode in this case is transmission, with a halogen source of 150 W power. The DC voltage source can generate voltages between 0.5 V and 90 V and its outputs are connected to a tungsten probe with a tip diameter of about 25  $\mu\text{m}$  as well as to the substrate.

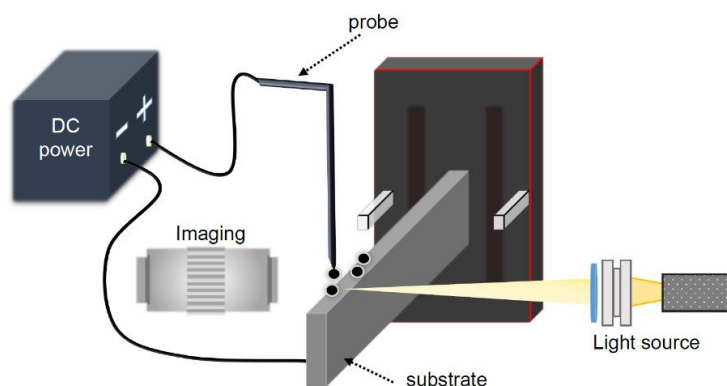


Figure 3.4: Schematic representation of the particle manipulation setup. Each component is mounted on an x-y-z translator base, which allows to position them independently.

The particle manipulation procedure is demonstrated in Figure 3.5, where PA12 particles of 115  $\mu\text{m}$  radius are manipulated before performing *in-situ* measurements. First, similarly sized particles are deposited on the mirror polished stainless steel substrate on random locations. Then the imaging system and light source are positioned in line with a particle on the substrate. The tungsten probe is then positioned within the field of view of the camera. Subsequently, a positive and negative voltage is applied to the probe and the substrate, respectively. By applying a voltage to the probe and substrate, a non-uniform electrostatic field between both is generated. When a polymer particle is present within such an electric field, a dielectrophoresis force is exerted on it [117], which in this case leads to attraction towards the tungsten probe. By translating the substrate a similar-sized particle can be found, keeping the probe with particle within focus. Once the second particle is also in focus, the probe is positioned close to the second particle. By switching off the voltage, the first particle drops from the probe onto the substrate next to the second particle. Once both particles are positioned, the substrate is carefully placed back into the sample chamber.

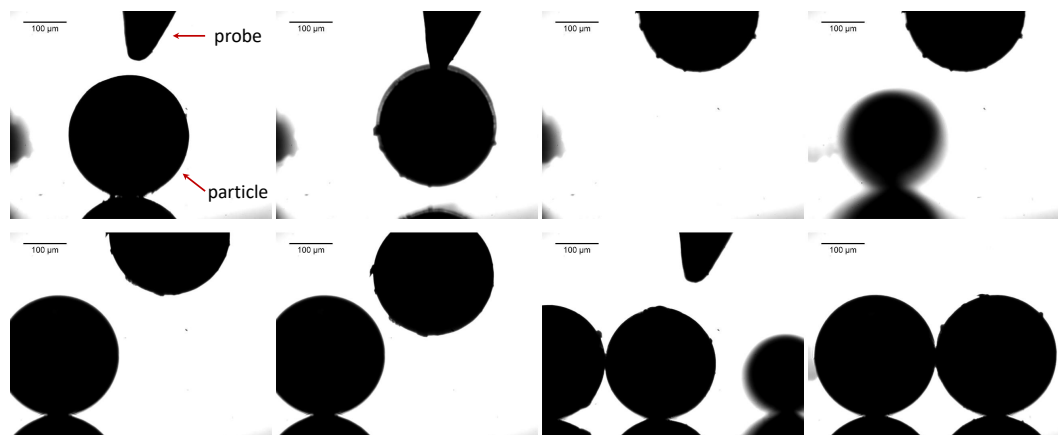


Figure 3.5: Image sequence (from top left to bottom right) shows a non-destructive way of manipulating PA12 particles of  $115\ \mu\text{m}$  radius by applying a voltage between the probe and the substrate.

### 3.3.3 Micropositioning of a particle for *in-situ* X-ray characterization

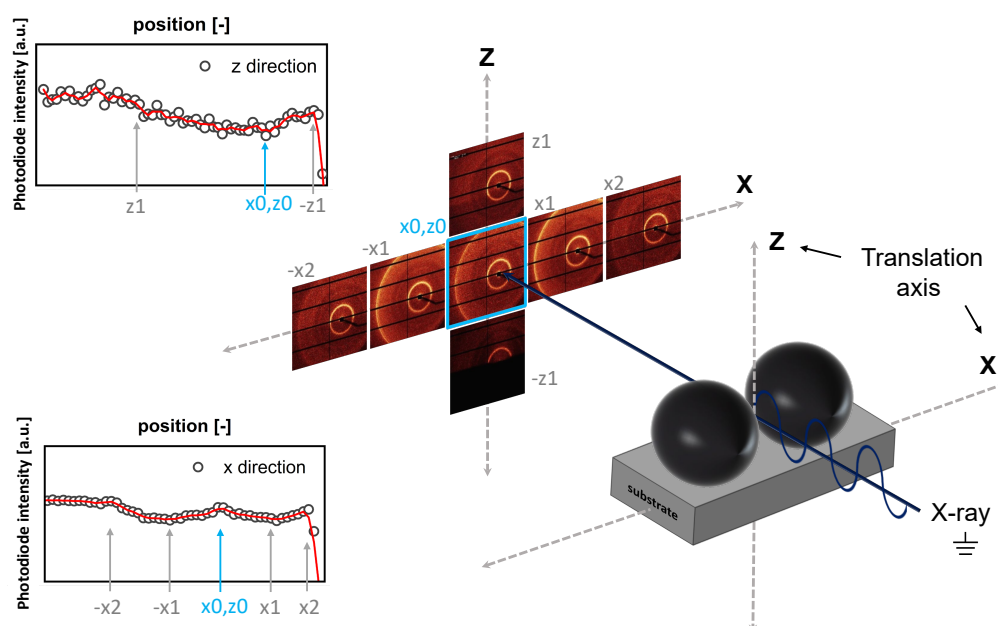


Figure 3.6: Illustration of the X-ray scanning technique to find the interface between the particles. The X-ray beam and detector are stationary. By translating the substrate in  $x$  and  $z$  direction, different X-ray patterns are obtained (indicated by  $x, z$  coordinates of the substrate). The substrate obstructs the X-ray beam whereas the presence of a particle maximizes the scattered intensity. The curves present the photo-diode intensity at the beam center. The bold red line is a guide to the eye.

To study the crystallization kinetics of the molten polymer in the sintered bridge, it is important that the interface between both particles is in-line with the X-ray source and detector. A coarse X-ray scan, performed by translating the sample chamber, along  $x$ - and  $z$ -direction enables to determine the location of the particles from the intensity



value of the photodiode aligned with the X-ray source. Once scattering patterns are obtained, ensuring that the particles are in the laser beam, finer scan steps along  $x$ - and  $z$ -direction determine the exact location of the interface between both particles. Thereto, the intensity at the characteristic scattering angle for crystalline PA12 is used. While scanning in the  $z$ -direction, the substrate below the particles blocks the X-ray beam whereas the air above the particles mainly results in transmission of the primary beam and small angle scattering. The photodiode intensity exhibits a weak minimum and the scattered intensity shows a weak maximum at a vertical distance between the X-ray beam and substrate that equals the particle radius, which corresponds to the desired beam location. In the  $x$ -direction, the center of the spherical particles exhibits more pronounced scattering as the thinner sides, which allows to determine the interface location as a weak minimum in scattered intensity and weak maximum in transmitted intensity. Figure 3.6 shows that frame  $x_o, z_o$  is the common interface location for scans along the  $x$ - and  $z$ -direction respectively. The inset graphs in Figure 3.6, showing the scattering patterns and photodiode intensity values as a function of the location of the particle pair, illustrate the method.

### 3.4 Results and discussion

To demonstrate the capabilities of the home-built laser sintering setup, as a case study, two PA12 particles with a radius of  $115 \mu\text{m}$  are sintered while performing time-resolved in-situ optical imaging and X-ray characterization. The sample chamber temperature is set sufficiently below the polymer melting temperature ( $155^\circ\text{C}$  versus  $178^\circ\text{C}$ ). Based on the melting enthalpy of PA12, the energy to completely melt one PA12 particle is calculated to be  $192 \mu\text{J}$ . Therefore, a pulse energy of  $384 \mu\text{J}$  was applied with a pulse duration of  $1 \text{ ms}$ . As expected, raising the temperature locally at the interface above the melting temperature leads to molecular mobility which allows for fast interpenetration of polymer chains from both particles followed by viscous flow, driven by the surface tension [118]. Hence, particles sinter together and subsequently the dumbbell-shaped particle doublet undergoes a further shape relaxation, until heat loss of the material and crystallization leads to cooling and thus solidification which freezes the shape, as illustrated in Figure 3.7.

To quantify the kinetics of the sintering process, the dimensionless neck radius ( $x/a_o$ ) is quantified by tracking the sintering neck  $x$ , formed between the particles with initial particle radius  $a_o$ , of both particles, as defined in Figure 3.7. To extract the neck and radii the image sequence was analyzed using Matlab<sup>®</sup>. A custom-written code was used that includes the Circle Hough Transform (CHT) for finding circles and determines the distance of the neck edge to the centerline connecting both particles. Figure 3.8 shows the tracked dimensionless neck plotted against sintering time. The laser is switched on at time  $t = 0 \text{ s}$  and the sintering kinetics in Figure 3.8 shows that the laser pulse can be considered instantaneous with respect to the sintering kinetics. The slope of the curve in Figure 3.8 provides the sintering rate, and a progressive decrease in sintering rate is observed due to heat loss which eventually leads to solidification of the material [119].

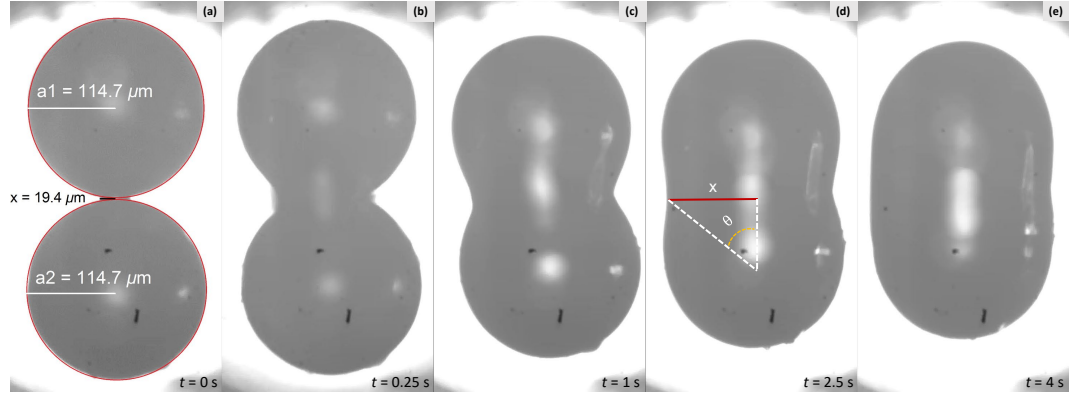


Figure 3.7: Image sequence of sintering (a to e) for PA12 particle pairs of radius  $a_o = 115 \mu\text{m}$ , wherein heating chamber temperature  $T_c = 155^\circ\text{C}$ , pulse energy  $E_p = 383 \mu\text{J}$  and pulse duration  $t_1 = 1 \text{ ms}$ . The evolution of the neck (black line) at the interface between the two particles is followed in time.

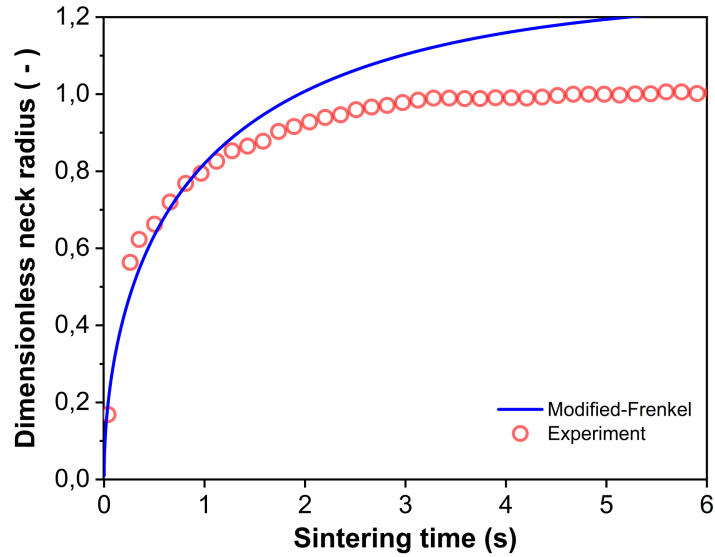


Figure 3.8: Comparison of modified-Frenkel model with sintering experimental results of PA12 for a particle radius  $a_o = 115 \mu\text{m}$ , heating chamber temperature  $T_c = 155^\circ\text{C}$ , pulse energy  $E_p = 383 \mu\text{J}$  and pulse duration  $t_1 = 1 \text{ ms}$ . Viscosity value in the modified-Frenkel model corresponds to a constant temperature of  $224^\circ\text{C}$ .

Several models are available to describe isothermal viscous sintering of liquid droplets. A model for viscous sintering of two spherical equal-sized Newtonian materials [120] was fit to the evolution of the neck, as shown in Figure 3.8. The time evolution of the angle  $\theta$  between the line connecting the particle centers and that connecting a particle center and the extreme point of the neck, represented in Figure 3.7(d), can be found from:

$$\frac{d\theta}{dt} = \frac{\Gamma}{a_0\eta} \cdot \frac{2^{-5/3}\cos\theta\sin\theta}{K_1^2(2 - \cos\theta)^{5/3}(1 + \cos\theta)^{4/3}}, \quad (3.3)$$



where  $\Gamma$  denotes the surface tension,  $\eta$  the viscosity and  $a_o$  the particle radius.  $K_1$  is given by [121]:

$$K_1 = \frac{\tan\theta}{2} - \frac{\sin\theta}{6} \cdot \left[ \frac{2 \cdot (2 - \cos\theta) + (1 + \cos\theta)}{(1 + \cos\theta) \cdot (2 - \cos\theta)} \right]. \quad (3.4)$$

From  $\theta$ , the dimensionless neck radius  $x/a_o$  is obtained [120]:

$$\frac{x}{a_o} = \sin\theta \cdot \left( \frac{4}{(1 + \cos\theta)^2 \cdot (2 - \cos\theta)} \right)^{1/3}. \quad (3.5)$$

This equation has been proven to be able to describe isothermal viscous sintering of polymer particles on a heated substrate [120]. However, in our case, isothermal conditions and a homogeneous temperature distribution across the particles are not expected due to the short laser pulse followed by cooling. Nevertheless, using a constant viscosity as a fitting parameter, the model can predict the initial sintering kinetics. The obtained viscosity value is 81 Pa·s, which according to the Arrhenius parameters for PA12, would correspond to a temperature of 224°C.

The subsequent cooling and solidification of the particle bridge is governed by a combination of heat diffusion from the laser illuminated area to the remainder of the particle as well as heat loss to the environment. From the heat diffusion time  $t$  in a semi-infinite medium ( $t = x^2/\alpha$ , with  $x$  the diffusion distance and  $\alpha$  the thermal diffusivity) it follows that the laser heat can diffuse through the complete particle over a time of approximately 0.76 s. Heat loss to the environment mainly occurs through free convection (radiation contribution is much smaller), and will lead to a reduction of the particle temperature, according to [81]:

$$T_p(t) = (T_{\max} - T_c) \cdot \exp\left(-\frac{hAt}{mc_p}\right) + T_c, \quad (3.6)$$

where  $m$  is the mass of the particle,  $c_p$  the heat capacity,  $A$  the particle surface area,  $h$  the heat transfer coefficient,  $T_{\max}$  the maximum temperature at the interface of the particles and  $T_c$  the temperature of the heating chamber. Herein, a homogeneous temperature profile throughout the particle is assumed, based on the relatively low values of the Biot number,  $Bi < 0.6$  ( $Bi = h \cdot L_c / k = h \cdot (a_o/3) / k$ , with  $a_o$  the particle radius,  $h$  the heat transfer coefficient,  $L_c$  the characteristic length and  $k$  the thermal conductivity [122]). Hence, it can be estimated that, depending on the value of  $h$  (which varies between 300 and 50 W/(m<sup>2</sup>·K) depending on the used correlation [123]) the particles take on the order of 1.5 s to 9.8 s to cool down to 160°C. This timescale corresponds approximately to that of the sintering kinetics in Figure 3.8. Hence, whereas with complete sintering of both particles and in the absence of pinning of the particles to the substrate, the equilibrium state would be a single nearly spherical droplet on the substrate with final droplet radius equal to 1.26  $a_o$ , [120] here an extended polymer shape remains after solidification. More elaborate studies combined with numerical simulations are required to fully analyze this

complex process, which involves a varying and non-homogeneous temperature as well as flow profile within the particles [97].

Apart from the optical visualization of the macrostructure of the particle doublet, wide-angle X-ray diffraction experiments allow to characterize the development of the crystalline microstructure. To demonstrate how laser sintering affects the crystal morphology, the intensity profile before sintering is compared with that after sintering. Figure 3.9(a) shows these intensity profiles, obtained from radially integrating the intensity over an azimuthal angle of  $90^\circ$  and plotting it versus scattering vector  $q$  for the situation before sintering and after 24 s, at which point steady state was reached. The integrated intensity, peak position, and peak width were obtained by fitting the curve with a double Gaussian-Lorentzian function [124]. To calculate crystallinity, an additional Gaussian-Lorentzian function was used to fit the amorphous background [125]. Thereto, the scattered intensity profile in the frame just before the polymer started to crystallize was used. The crystallinity was calculated from the deconvolution of the total intensity into the amorphous and crystalline contributions:

$$\chi_c = \frac{A_c}{A_c + A_a}, \quad (3.7)$$

where  $\chi_c$  is crystallinity,  $A_c$  is the area of the crystalline peaks and  $A_a$  is area of the amorphous halo.

For crystallization temperatures above  $130^\circ\text{C}$ , two distinct crystalline reflections are generally visible for PA12 since above this temperature it crystallizes into a combination of  $\gamma$ - and  $\alpha'$ -phase [126]. Before sintering, a distinct peak at  $q = 15.02 \text{ nm}^{-1}$  ( $d = 0.418 \text{ nm}$ ) with a shoulder can be observed, as shown in Figure 3.9(a) by the solid gray line. After sintering, this is transformed into two clear peaks with a secondary peak at  $14.6 \text{ nm}^{-1}$  ( $d = 0.430 \text{ nm}$ ). These peak positions correspond to the values given in literature for the crystalline reflections of the  $\alpha'$ - phase in PA12, which is typical for crystallization at high temperatures [112, 126]. However, some studies in literature report the opposite transition from the  $\alpha'$  phase showing two crystalline reflections to a  $\gamma$ - phase exhibiting only one reflection after sintering [127]. This phase transition is temperature sensitive and eventually forms the commonly observed  $\gamma$ - phase [124, 128]. Though there is a clear difference in crystal morphology, the crystallinity percentage as determined from the ratio of the integrated intensity of the crystalline peaks over the total integrated intensity, before and after sintering is about the same at around 21.3%. Crystallinity percentage can vary between 20% to 46% for PA12 polymer, depending on the grade and processing condition [112, 125, 129]. Whereas previous studies are limited to the overall crystal morphology of a sintered part, our data in Figure 3.9 provide the crystal details locally in the sintered particle bridge. Moreover, as local sintering parameters can be precisely controlled and flow profiles can be extracted from the growth of the neck radius [97, 120], a more detailed study of the effects of processing conditions on crystallization due to sintering can be performed with our newly developed setup. Since laser sintering and corresponding flow in the neck region can lead to molecular alignment, anisotropic crystalline structures may be generated. However, under the conditions studied in the present case study, no such anisotropy of the scattering images was noticed, indicating

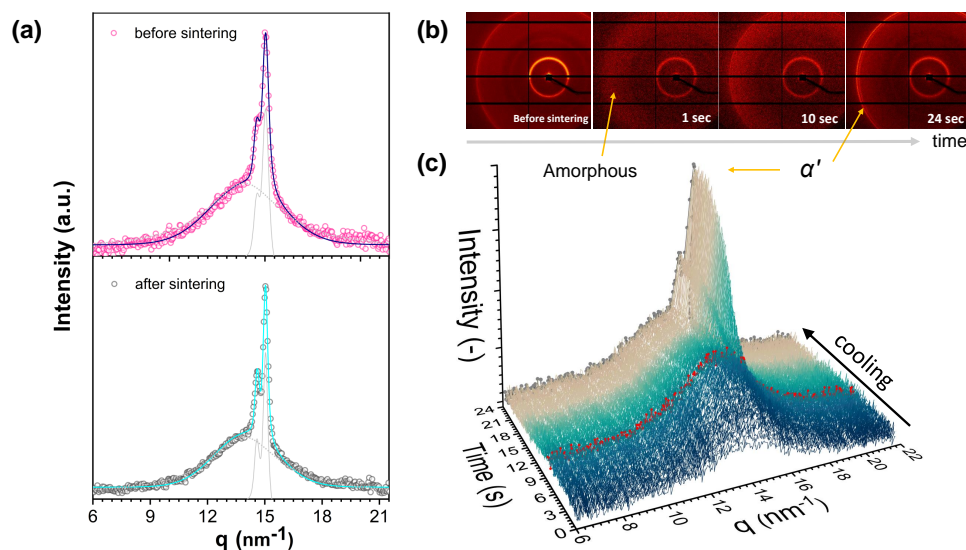


Figure 3.9: (a) Integrated intensity as a function of scattering vector  $q$ , before and after sintering. The markers represent the radially integrated pattern obtained from experiments and the lines represent the sum of fitted peaks using a Gaussian-Lorentzian function. The grey dotted line is the amorphous halo and the grey solid line is the peak fit of the crystalline peak. (b) Image sequence of time-resolved 2D-WAXD patterns of PA12, before and during sintering for PA12 particles of radius  $a_o = 115 \mu\text{m}$  with heating chamber temperature  $T_c = 155^\circ\text{C}$ , pulse energy  $E_p = 383 \mu\text{m}$  and pulse duration  $t_1 = 1 \text{ ms}$ . (c) 3D plot of the radially integrated intensity as a function of scattering vector  $q$  for the complete acquisition time. Red line represents the amorphous halo before crystallization starts.

that the flow was not strong enough to result in crystal orientation, or at least not over a substantial region of the polymer particles. It should be taken in account that the ratio of the X-ray beam diameter ( $100 \mu\text{m}$ ) to the particle diameter ( $230 \mu\text{m}$ ) is 0.43, whereby almost half of the particle area is irradiated, resulting in a convoluted image of the actual bridge and the neighbouring region.

In addition to providing local information about the crystal structure of PA12, the second major advantage of our approach is that the time-resolved evolution of the crystallization process during sintering is available as well. Figure 3.9(b) shows scattering patterns at different points in time after the laser pulse. Initially, during the short laser pulse, the material is molten as evidenced by the absence of the typical diffraction rings of the PA12 crystals. The typical phase transition time is of the order of 0.4 s. Over the course of time, this diffraction ring reappears indicating that the polymer starts to crystallize. The obtained intensity profiles were plotted versus the scattering vector  $q$ , at various times, as can be seen in the 3D plot in Figure 3.9. This figure clearly shows that the complete phase transition from the molten amorphous state at time  $t = 0 \text{ s}$ , until full solidification at  $t = 24 \text{ s}$  can be followed, at the sintering zone. By determining the degree of crystallization from the diffraction patterns collected as a function of time, the crystallization kinetics can be analyzed, as shown in Figure 3.10. Crystallinity is absent at the instant the laser pulse hits the interface of the particles, at

time  $t = 0$  s. The onset of solidification from the molten amorphous to the solid semi-crystalline state can be observed at time  $t = 8$  s as the particles undergo cooling until crystallization ends at time  $t = 24$  s. The half-time of the crystallization, as obtained from Figure 3.10, is 13 s. As mentioned before in Section III(A), under isothermal and quiescent conditions,  $t_{1/2}$  is about 19.5 s at  $155^\circ\text{C}$  and it has been shown that this time increases with temperature up to the melt temperature [112]. Since the temperature during laser sintering evolves from a relatively high temperature directly after the laser pulse to minimum  $155^\circ\text{C}$ , it is clear that the observed crystallization kinetics is faster than expected from the quiescent crystallization kinetics. This could be due to the flow originating from the bridge growth process, demonstrated in Fig. 8, which can affect the crystallization process. Similar increases in crystallization kinetics due to flow have been observed for many polymers [130]. However, for PA12 the flow-induced crystallization kinetics has not yet been systematically analyzed. Therefore, quantitative comparison of the crystallization kinetics observed here with that under standard flow conditions is not possible. Finally, by comparing the kinetics in Figs. 8 and 10, it can be seen that under the studied conditions, the macrostructural kinetics in the form of the neck growth has a much faster timescale as compared to the crystallization. By tuning the laser energy, pulse duration and chamber temperature, it will be possible to alter both timescales independently as the first one mainly depends upon the polymer viscosity whereas the second depends on a combination of shear and temperature effects. Hence, a wealth of possible processing conditions can be generated, possibly resulting in a variety of crystalline microstructures.

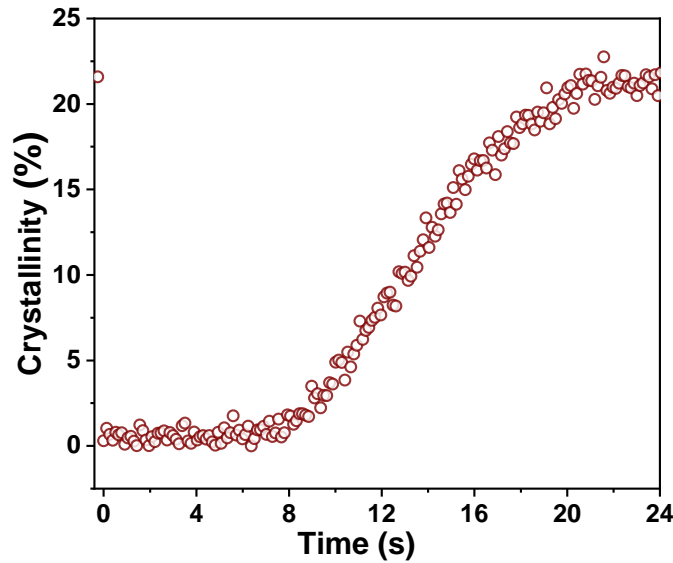


Figure 3.10: Time evolution of crystallinity during the sintering process for PA12 particles of radius  $a_o = 115 \mu\text{m}$ , heating chamber temperature  $T_c = 155^\circ\text{C}$ , pulse energy  $E_p = 383 \mu\text{m}$  and pulse duration  $t_1 = 1$  ms.

These preliminary data from a case study on PA12 particles demonstrate the unique capability of our setup to capture the kinetics of the development of the macrostructure in the form of neck-radius growth as well as the microstructure in the form of crystallinity

and crystal-type evolution during laser sintering. The results also illustrate the accuracy with which these features can be obtained. Hence, future experiments at different processing conditions will provide us with critical information about the laser sintering process. In addition, different classes of polymers ranging from commodity polymers like polystyrene to high performance polymers like polyether ether ketone can be sintered in the setup. The setup is also flexible towards the use of small angle X-ray scattering or more local characterizations using a more pronounced focusing of the X-ray beam.

### 3.5 Conclusions

A novel in-house developed experimental laser sintering setup has been designed and constructed that has the unique ability to allow in situ time-resolved microscopic and X-ray observations of laser sintering with precise control over all sintering parameters. A case study on the sintering of PA12 particle pairs demonstrates that real-time information about the sintering dynamics as well as crystallization kinetics can be obtained with a good signal-to-noise ratio and with sufficient spatial and temporal resolution. Since structure evolution and crystallization kinetics during laser sintering are complex and coupled processes involving nonisothermal, nonhomogeneous temperature profiles, and complex flow fields, this laser sintering setup provides direct access to essential local and timeresolved information about the structural processes involved. Future experiments using this setup can provide us with essential knowledge to understand the relations between sintering conditions and microstructure development. Hence, this unique device opens up new promising perspectives in the field of 3D printing by selective laser sintering.

### Acknowledgments

This work forms part of the research programme of the Brightlands Materials Center (BMC). We acknowledge the European Synchrotron Radiation Facility (ESRF) for provision of synchrotron radiation facilities and NWO for financing beamtime at ESRF. We would like to thank Dr. Daniel Hermida Merino for assistance in using the Dutch-Belgian beamline (DUBBLE) BM26 and Prof.Dr.ir. Leon E. Govaert for providing the PA12 polymer. We also thank Dr. Rob Satnik from Acal BFi for supplying components and helpful discussion on laser alignment.

## Laser sintering of polymer particle pairs studied by *in-situ* visualization

### Abstract

Merging of particle pairs during selective laser sintering (SLS) of polymers is vital in defining the final part properties. Depending on the sintering conditions, polymers can undergo full or partial sintering whereby incomplete sintering results in poor mechanical properties. At present, the underlying mechanisms and related conditions leading to various consolidation phenomena of polymer particles are not well understood. In the present work, a novel in-house developed experimental setup is used to perform laser sintering experiments on polystyrene (PS) particle doublets while performing in-situ visualization of the sintering dynamics. From the recorded images, the evolution of the growth of the neck radius formed between both particles is analyzed as a function of time. Sintering conditions such as heating chamber temperature, laser pulse energy and duration, laser spot size and particle size are precisely controlled and systematically varied. A non-isothermal viscous sintering model is developed that allows to qualitatively predict the observed effects of the various parameters. It is shown that the sintering kinetics is determined by a complex interplay between the transient rheology caused by the finite relaxation times of the polymer and the time-dependent temperature profile which also affects the polymer viscosity. The combination of a full material characterization with sintering experiments under well-defined conditions has resulted in a general understanding of the effects of material and process parameters on laser sintering. Thereby a strong foundation is laid for the route towards rational design of laser sintering.

---

*Largely reproduced from:*

1) Hejmady, P., van Breemen, L. C. A., Anderson, P. D., & Cardinaels, R. (2019). Laser sintering of polymer particle pairs studied by in situ visualization. *Soft Matter*, 15(6), 1373-1387.

## 4.1 Introduction

Selective laser sintering (SLS) is an additive manufacturing technique that offers the possibility to produce intricate geometries and freeform surfaces from polymer powder without the use of a mould [87, 131]. This provides economic benefits and opens up new options for producing complex functional parts, currently being limited by traditional techniques like injection moulding. In SLS, a bed of polymer powder is heated below the glass transition temperature ( $T_g$ ) and melting temperature ( $T_m$ ) for amorphous and semi-crystalline polymers respectively. A laser beam selectively heats and thereby sinters specific areas corresponding to the coordinates provided by a computer-aided design (CAD) model. After lowering the work platform, another layer of powder is added and the process is repeated, thus, the part geometry is created layer by layer [2, 4, 85, 132]. However, a number of limitations exist in the SLS process and associated products. Some of the commonly found defects like porosity and poor layer-to-layer adhesion lead to poor mechanical properties of the final printed parts as compared to products produced by traditional polymer processing methods [12, 13]. Furthermore, a limited control over process parameters and incomplete understanding of the effects of the processing conditions on the consolidation phenomena of the polymer powder have further hampered the production of parts with reproducible product properties [14].

In literature, different approaches have been taken to overcome these previously mentioned adversaries. Extensive research using commercial SLS machines has shown that varying the processing conditions allows to change the final part morphology and crystalline microstructure [133, 134, 135, 136]. Heating chamber temperature, particle size and size distribution, laser energy and scan speed all have been shown to affect the final properties [12]. For instance, it was observed that at constant laser speed and powder bed temperature, gradually increasing the laser power allowed to achieve better consolidation of the polymer powder whereas a low power yielded fragile parts with poor mechanical properties [2, 137]. However, due to the fact that global process parameters rather than local conditions are controlled and spatial as well as temporal variability in parameters such as temperature may occur, the reported observations are mostly specific to each machine. Furthermore, the information is limited to the final morphology obtained and insight in the actual structure development during processing is still lacking.

Another approach has been the study of the coalescence process on the scale of particle doublets, allowing a simplified representation of the complex process. When two particles in contact reach their melting point, they tend to flow with a progressively increasing contact region (neck) [94, 95, 120]. This particle sintering on the level of a particle doublet has been investigated by means of hot stage microscopy, which has enabled to study the coalescence process and to relate it with existing analytical models. It was reported that capillary forces drive an outwards polymer flow [138], which was later verified for polypropylene (PP) particles [139], by tagging the inter-particle neck and tracking the flow along the weld line. The temperature dependence of the sintering rate was experimentally verified for PMMA and PP particles showing that the rate and type of flow

depend on the sintering temperature [139, 140]. Frenkel derived a simple scaling relation allowing to describe the early sintering stages by assuming Newtonian flow and a constant strain rate [141]. The Frenkel theory was later modified by Pokluda et. al. [120] by balancing the work of surface tension and that of viscous dissipation, while taking into account volume conservation. The thus obtained model was found to be suitable to describe the complete sintering process of viscous liquids. The dependence of the sintering process on the rheological fluid parameters was shown experimentally by measuring the inter-particle neck thickness for PEEK and PEK polymer particles of different viscosity at a fixed temperature [142], indicating that the sintering rate is affected by the viscosity and elasticity of the polymer and faster coalescence was observed for the less viscous polymer [96]. A model considering the viscoelastic nature of the sintered materials was developed by Bellehumer et al. [95] by using an upper convected Maxwell model for the calculation of the work of viscous dissipation. By using a quasi-steady state approach to isolate the effects of the elastic stresses, they could show that melt elasticity slows down sintering. This was later also experimentally verified by Muller et al. [143] for a range of viscoelastic Boger fluids. Subsequently, Scribber et al. [121] applied the model of Bellehumer under full transient conditions, thereby showing that due to time effects of the viscosity, increasing the relaxation time of the material can accelerate sintering. This acceleration due to the transient rheology has also been confirmed by Balemans et al. using fully resolved numerical simulations [144].

Although the different observations and models allow to provide an understanding of sintering phenomena in processing techniques such as rotational moulding, they do not fully represent the laser sintering process. Up to now, experimental studies focusing on the laser-stimulated heating and sintering of particle doublets are lacking. Also, the available analytical models consider isothermal conditions, neglecting thermal effects on the viscosity of the polymer. However, with a laser being the heat source that locally binds particles together, in-homogeneous and non-isothermal temperature profiles are obtained [9, 10, 145]. A recent numerical study has shown that a judicious choice of the different sintering parameters would allow significant optimization of the sintering process [97]. The objective of the present work is to provide insight in the sintering dynamics during laser sintering of an amorphous polymer, in this case polystyrene. We use a novel in-house developed experimental setup which incorporates the main features of an SLS device and at the same time facilitates optical visualization of the sintering dynamics with precise control over all processing parameters. Based on a systematic experimental study of the effects of the various processing parameters, the relationships between on the one hand material properties and processing conditions and on the other hand the sintering of polymer particle doublets have been investigated.

## 4.2 Experimental setup

Figure 4.1(a) depicts the experimental setup for in-situ laser sintering experiments. It consists of a home-build heated sample chamber in which the sintering takes place while optical imaging via the top and side is possible with two separate optical trains. Laser



light is guided into the chamber from the top. A visible light ( $\lambda = 532 \text{ nm}$ ) continuous wave (CW) laser (Genesis MX) from Coherent is used, with a spatial TEM<sub>00</sub> mode, which provides a Gaussian intensity distribution. The small wavelength laser with stable beam parameters, low noise and high power-stability ensures a well-defined spot size and precise control over the laser impact energy. One of the key components in the setup is the acousto-optic modulator (AOM, Isomet), whose main functionality is to pulse the laser. The laser beam is diverted through the AOM, and by switching on and off the modulation within the AOM, the CW laser beam can be pulsed whereby excess energy is diverted to the beam dump. The precise control over the laser impact parameters namely pulse duration as well as pulse energy, allows to simulate various laser scanning speeds encountered during an actual laser sintering process. The design of the sample chamber ensures the possibility to perform in-situ laser sintering with simultaneous visualization of the sintering dynamics by incorporation of quartz windows on the top and side. A mirror polished stainless steel sample substrate holds the particle pairs to be sintered and visualized. The chamber is built from aluminum walls fitted with heating rods on each side, as well as in the substrate. A low thermal conductivity ( $0.4 \text{ W/(mK)}$  at  $400^\circ\text{C}$ ) isolation around the box limits the heat loss to the environment. Furthermore, two thermocouples measure the temperature of the substrate and the chamber air respectively. The thermocouples and heating rods are connected to a temperature-control unit (Hasco), which ensures that the sample temperature can be controlled within  $1^\circ\text{C}$ . In the present work, the temperatures of the heating chamber and the substrate were always kept at the same value. Custom made optical trains were designed, to capture the fast sintering dynamics and relatively small length scales of the formed particle bridges that dominate during the sintering process. The main components of the optical train are the Pixelink (PL-D725MU-T) CMOS camera and an infinity corrected objective lens with 20x magnification from Mitutoyo (NA 0.28). Design considerations were made as such that the heat loss from the sample chamber does not affect the performance of the imaging train and at the same time allows a minimum possible angle of incidence of the laser light ( $30^\circ$ ) with respect to the objective lens (4.1 b). A well-defined focal spot was achieved by placing a focusing lens with known focal length along the laser path, as shown in Figure 4.1 b. An animation illustrating the features of the experimental setup can be found in the electronic supplementary information (ESI).

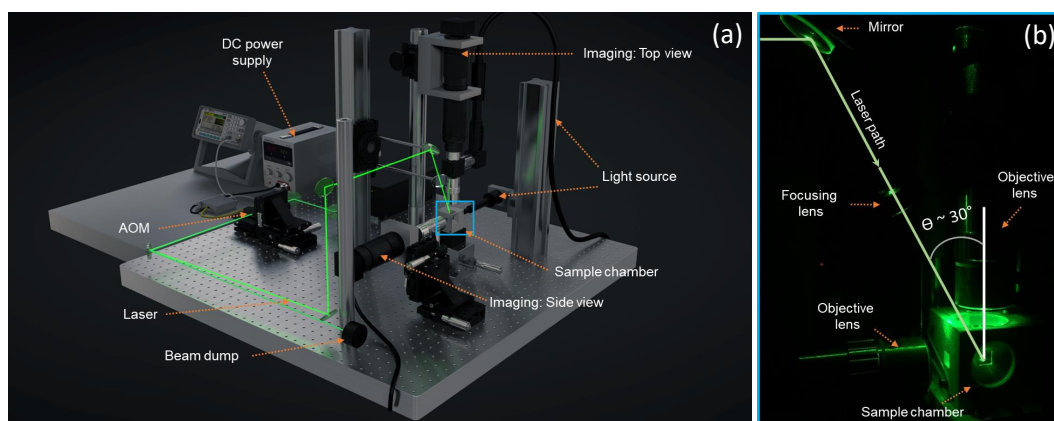


Figure 4.1: (a) Rendered image of the experimental setup highlighting the main components. (b) Close-up of the sample chamber depicting the laser path.

## 4.3 Materials and methods

### 4.3.1 Materials and materials characterization

Spherical polystyrene (PS) particles were prepared from standard low molecular weight polystyrene (Sigma Aldrich). The PS particles contained 2 wt% of nubian black PC-0870 dye (Orient Chemical Industries co., LTD), which enables visible-light laser energy to be absorbed. This dye has a molecular weight ( $M_w$ )  $\sim 397$  g/mol. The thermal conductivity  $k$ , density  $\rho$  and surface tension  $\Gamma$  of polystyrene are respectively 0.167 W/m·K, 1040 kg/m<sup>3</sup> and 35.6 mN/m at 115°C [146, 147, 148].

To select suitable sintering parameters and to analyze the sintering process, the thermal, optical and rheological properties of the used material are required. Differential scanning calorimetry measurements (Mettler Toledo 823e/700 DSC module) at a heating rate of 10°C/min were performed to determine the glass transition temperature ( $T_g$ ) and specific heat capacity ( $c_p$ ) of PS. Thereto, the DSC was calibrated for heat flux and melting enthalpy with indium. Rheological measurements were carried out on a strain-controlled rheometer (TA instruments RDAIII) equipped with a convection oven using a plate-plate geometry of 25 mm diameter. Strain sweep experiments at 1 Hz determined the linear viscoelastic regime and at temperatures sufficiently above the  $T_g$  of the polymer, frequency sweep experiments at four different temperatures were performed. The absorption properties of the dyed polymer at the laser wavelength were characterized by measuring the intensity of the transmitted and reflected light through thin polymer sheets. Thereto, polymer samples containing different concentrations of dye (0-3 wt%) were prepared by solution mixing in acetone. The required amounts of polymer and dye were dissolved in acetone by first mixing with a magnetic stirrer and subsequently using ultrasonication (each for one hour). The resulting mixture was poured in a petri dish, wherein the dyed polymer is obtained after acetone evaporation. Compression moulded disks of various thicknesses (50-230  $\mu\text{m}$ ) were prepared between glass microscope slides with a Fontyne plate press used at 10 kPa and 165°C. For the absorption experiments, the sample was placed in the laser path on a sample holder with the possibility to vary the incoming angle of the laser light on the sample. Using a continuous beam with a light intensity of 0.04 W/mm<sup>2</sup>, the intensity of both transmitted and reflected light was measured with an XLP12 thermopile at an incoming angle of 30°. Furthermore, the transmission was measured for an incoming angle of 0°.

### 4.3.2 Micromanipulation

At the start of a sintering experiment, two polymer particles of roughly the same size and in contact at their interface, should be placed on the heating bed. To accomplish this, we have developed a manipulation technique that allows to pick and place polymer particles independent of their size. Similarly sized polymer particles are selected and subsequently deposited on a mirror polished stainless steel substrate placed on an x-y-z translation

stage. A first polymer particle is brought in the field of view and in the focus of the camera. Subsequently, a tungsten probe with a tip diameter of 100  $\mu\text{m}$ , also connected to an x-y-z translation stage, is positioned within the field of view of the camera, as can be seen in Figure 4.2(a). Then, a voltage is applied between the probe and the substrate, which creates a non-uniform electrostatic field. When a dielectric polymer particle is present in this field a dielectrophoresis force is exerted on it, which attracts the particle to the probe, as illustrated in Figure 4.2(b) and Figure 4.2(c) and allows to lift it up (4.2 d). By translating the substrate in x-y-z direction, similarly sized particles can be found, as shown in Figure 4.2(e). The probe with the particle is then positioned close to the second particle and the voltage is switched off, after which the first particle is released onto the substrate next to the second particle being in contact at their interface, as shown in Figure 4.2(f-h). This particle doublet now forms the starting point for a sintering experiment.

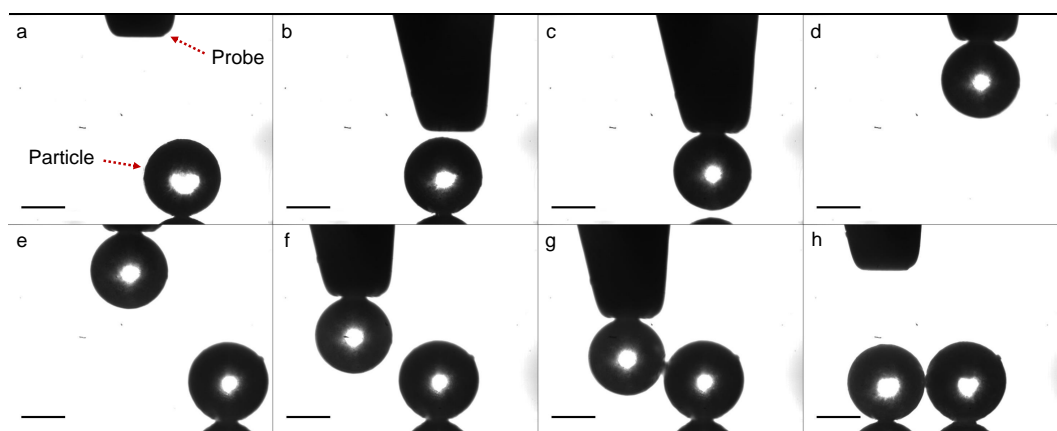


Figure 4.2: Image sequence illustrating micromanipulation of PS particles in a non-destructive manner. Scale bar represents 100  $\mu\text{m}$ .

### 4.3.3 Experimental protocol and data analysis

Before the start of the experiment, the laser-beam spot is focused at the correct location for visualization of the sintering process. In this work, the beam spot diameter is fixed at 40  $\mu\text{m}$ , as verified by optical imaging and fitting of a Gaussian profile on the spatial intensity distribution. Subsequently, the substrate with a particle pair was placed in the sample chamber and brought in focus on both camera's thereby ensuring correct alignment with respect to the laser beam. Subsequently, the chamber was heated to the required temperature (below the  $T_g$  of PS) at a relatively low heating rate, thereby avoiding temperature overshoots and allowing sufficient time to reach thermal equilibrium. Then, a single laser pulse is sent onto the particles while the sintering process is optically visualized. The obtained images are analyzed by means of a custom-made Matlab<sup>®</sup> code. The code uses the circle-Hough transform to detect circles in the images and to determine the particle diameter at each time instant [149]. For determining the size of the bridge between the polymer particles, the edge points are placed in an array and the point with the lowest distance perpendicular to the line connecting both particle centers is used to determine the neck radius.

## 4.4 Results and discussion

### 4.4.1 Determination of laser sintering parameters

To avoid sintering of the polymer particles in the absence of laser light, the temperature of the sample chamber should remain sufficiently below the glass transition temperature of the polymer, similar as in actual SLS printing. Fig. 3 shows the DSC thermograph of the used PS containing 2 wt% dye, from which the  $T_g$  was determined as the mid-point of the inflection of the thermogram. It can be concluded that the used PS has a  $T_g$  of 62°C and specific heat capacity  $c_p$  of 1320 J/(kg·K) in the liquid state. This  $T_g$  value corresponds to a molecular weight of around 3000 g/mol [150]. It should be noted that the effect of the dye on  $T_g$  was found to be minor, thereby indicating limited plasticization effects of the dye. To allow sintering, a sufficient amount of laser energy should be transferred to the particle pair. Neglecting heat losses and assuming full conversion of the visible light laser energy to heat, an estimation of the amount of laser energy required to raise the temperature of a single particle can be made using the following equation:

$$Q = mc_p\Delta T, \quad (4.1)$$

where  $Q$  is the heat energy (J),  $m$  is the particle mass (kg),  $c_p$  is the specific heat of polystyrene (J/(kgK)) and  $\Delta T$  is the temperature difference (K). For a particle radius of 60  $\mu\text{m}$ , this means the required energy  $Q$  to heat a single particle by 20 K is estimated to be 25  $\mu\text{J}$ . Based on this material information, the bed temperatures for the sintering experiments were fixed between 30°C and 53°C and the laser pulse energies were varied from 19-29  $\mu\text{J}$ .

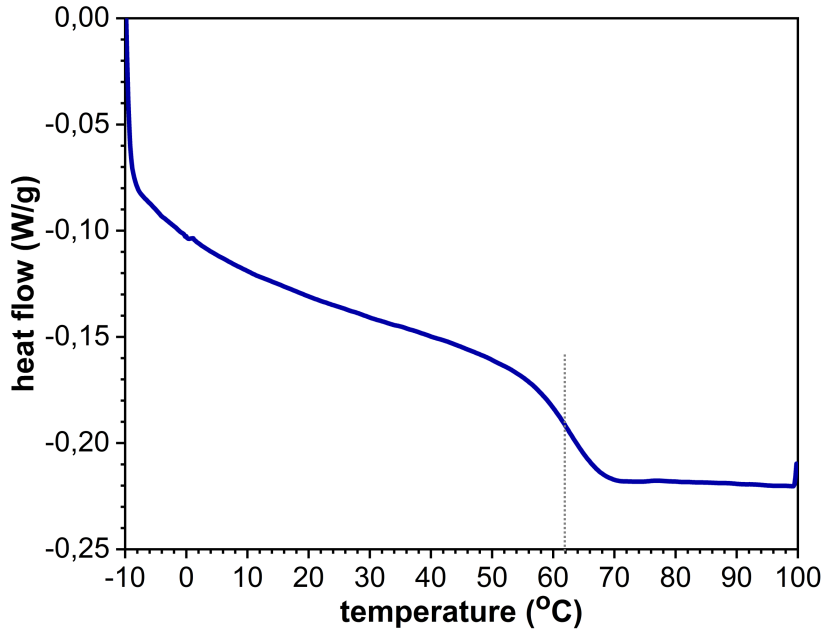


Figure 4.3: DSC thermogram (heating cycle) of PS containing 2 wt% dye using the midpoint of the inflection to determine  $T_g$ .

Viscosity plays a vital role in consolidation during laser sintering [151]. Since laser sintering is a non-isothermal process, the temperature-dependent viscosity is required to understand the sintering dynamics. Using the fact that simple polymers obey the Cox-Merz rule, the complex viscosity  $\eta^*$  is used to characterize the flow behaviour. To determine the steady state zero-shear viscosity  $\eta_{s0}$  as a function of temperature, a time-temperature superposition of the frequency-sweep experiments is first performed. This results in a master curve and shift factor  $a_T$  that obeys the Williams-Landel-Ferry (WLF) equation [152]:

$$\log(a_T) = \log\left(\frac{\eta_s(T)}{\eta_s T_{\text{ref}}}\right) = \frac{-C_1(T - T_{\text{ref}})}{C_2 + (T - T_{\text{ref}})}, \quad (4.2)$$

where  $C_1$  and  $C_2$  are constants,  $T_{\text{ref}}$  is the reference temperature,  $\eta_s(T_{\text{ref}})$  is the steady state viscosity at the reference temperature,  $T$  is the measurement temperature and  $\eta_s(T)$  is the steady state viscosity at the measurement temperature. The WLF equation is typically used to describe the time-temperature behavior of polymers near the glass transition temperature [152]. Using  $T_g$  as the reference temperature, values for  $C_1$  and  $C_2$  of respectively 13.05 and 147.1°C are obtained, which is in reasonable agreement with literature values for PS [153]. Hence, the DSC and rheology results are consistent. Figure 4.4 (a) shows the complex viscosity  $\eta^*$  versus angular frequency  $\omega$  at a reference temperature of 100°C for PS containing 2 wt% dye. With this reference temperature,  $C_1$  and  $C_2$  are equal to 10.37 and 185.07°C respectively. Subsequently, the master curve of the complex viscosity is fitted with the cross model [152]:

$$\eta_s = \eta_{s\infty} + \frac{\eta_{s0} - \eta_{s\infty}}{1 + (\lambda\dot{\gamma})^m}, \quad (4.3)$$

where  $\eta_{s\infty}$  is the steady state shear viscosity at infinite shear rate,  $\eta_{s0}$  is the steady state zero-shear viscosity,  $\dot{\gamma}$  is the shear rate,  $m$  is a constant and  $\lambda$  is the cross time constant with  $1/\lambda$  corresponding to the shear rate at the onset of shear thinning. This results in a zero-shear viscosity of 2119 Pa·s at the reference temperature of 100°C. Figure 4.4 (b) provides the zero-shear viscosity values at different temperatures together with the WLF fit that is used to determine the viscosity at other temperatures. Based on the measured viscosities, the expected timescale of the sintering process, using the characteristic timescale of the Frenkel model, which is  $(\eta_{s0} a_0)/\Gamma$  with  $\Gamma$  the surface tension of PS,  $\eta_{s0}$  the steady state zero-shear viscosity and  $a_0$  the initial particle radius [120], is on the order of 3 s for a particle radius of 60  $\mu$  and a temperature of 100°C. By fitting the small-amplitude dynamic moduli with a multimode Maxwell model (Figure 4.4 (a)) [152], the relaxation time distribution of the polymer is determined. Table 4.1 provides the different relaxation times and their respective contribution. Based on the data in Table 4.1, the viscosity average relaxation time is 6.1 s and the zero-shear viscosity is 2207 Pa·s at 100°C. From the sintering model of Bellehumeur et al. [95], which considers an upper convected Maxwell model for the polymer rheology with quasi-steady state conditions for the sintering (neglecting transient viscosity effects), it is concluded that for  $\lambda \approx 2 (\eta_{s0} a_0)/\Gamma$  as is the case here, the effect of the viscoelastic stresses on the sintering dynamics can be neglected. However, transient effects of the viscosity buildup after startup of the flow are expected to play a role [121].

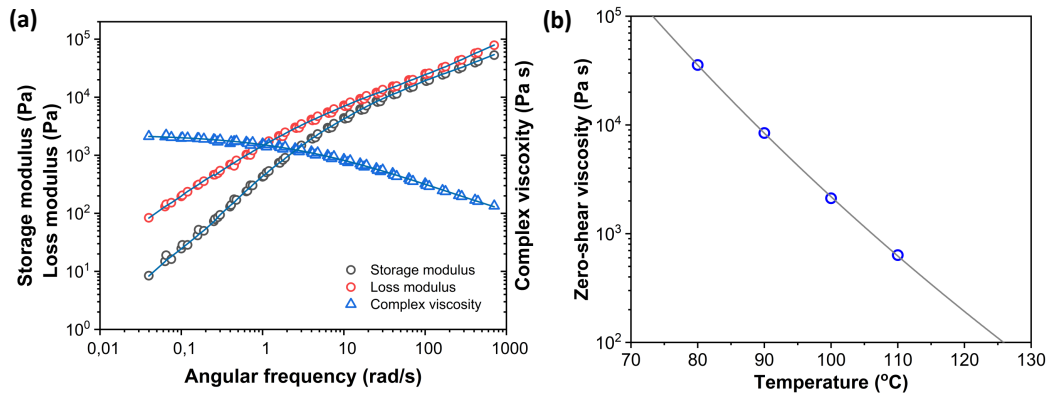


Figure 4.4: (a) Master curves for dynamic moduli and complex viscosity of PS containing 2 wt% dye at a reference temperature of 100°C obtained from frequency-sweep measurements at 80°C, 90°C, 100°C and 110°C. The viscosity is fitted with a Cross model and the dynamic moduli are fitted with a multimode Maxwell model (lines) (b) Temperature dependent zero-shear viscosity values fitted with the WLF equation (line).

To estimate the required dye content to allow for significant absorption of the laser energy, the transmission and reflection of laser light by PS sheets with various thicknesses and dye contents were analyzed. From this the absorption was determined since these three contributions together should equal the intensity of the incoming laser light. Figure 4.5

Table 4.1: Relaxation time distribution at 100°C for PS containing 2 wt% dye based on a multimode Maxwell model.

$\lambda_i$ (s)	$\eta_{si}$ (Pa·s)
0.00171	73.36
0.0104	164.32
0.0509	364.44
0.229	558.76
1.02	493.68
5.63	245.71
37.3	306.26

(a) presents the results for 100  $\mu\text{m}$  thick PS sheets as a function of the dye content. The amount of reflection is very small (around 5%) which corresponds to the prediction of Fresnel's law. Moreover, due to the nearly equal refractive indices of glass and PS (1.5 versus 1.59) the presence of the microscope slides on both sides of the sample, which was required due to sample brittleness, cannot be noticed on the reflection data, as was verified using a plane sheet of high molecular weight PS. Both the transmission  $T_I$  as a function of dye weight percent (4.5 (a)) as well as the transmission  $T_I$  as a function of sample thickness (4.5 (b)) follow the Lambert-Beer law:

$$\frac{I}{I_0} = T_I = \exp(-\epsilon lc), \quad (4.4)$$

with  $I_0$  the intensity of the incoming light,  $I$  the transmitted intensity,  $l$  the path length through the sample,  $c$  the concentration of dye and  $\epsilon$  the extinction coefficient. Fitting both data sets with this equation resulted in an extinction coefficient  $\epsilon$  of 1172  $\text{m}^2/\text{mol}$ , which makes it possible to determine the light absorption as a function of sample thickness and dye concentration. Finally, Figure 4.5(b) shows that the effect of the angle of incidence of the laser light is negligible, if the increased path length through the sample due to the sample orientation is taken into account. This is caused by the fact that reflection only constitutes a minor part of the total response. Based on the absorption values, a fixed dye content of 2 wt% was chosen for particle radii ranging from 30 to 105  $\mu\text{m}$ . This leads to an absorption value close to 90% of the incoming laser light.



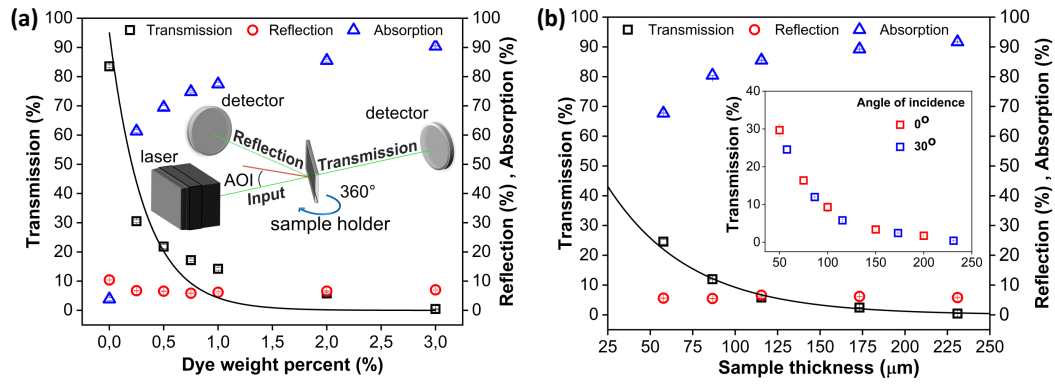


Figure 4.5: (a) Transmission, reflection and absorption of visible light (532 nm) as a function of dye wt% for a sample thickness of 100  $\mu\text{m}$  and angle of incidence (AOI) of  $30^\circ$ , (b) Transmission, reflection and absorption of visible light (532 nm) as a function of sample thickness perpendicular to the laser path for a dye-weight percent of 2% and angle of incidence of  $30^\circ$ . The inset compares the transmission at angles of incidence of  $0^\circ$  and  $30^\circ$ . Lines indicate fits with the Lambert-Beer law.

#### 4.4.2 Representative sintering behaviour

Figure 4.6 presents image sequences obtained in the top and side view during a typical sintering experiment. Movies of the sintering process in top and side view are available in the ESI. The laser pulse is applied at time  $t = 0$  s. In general, sintering consists of three stages [94]. Upon initial softening of the material due to heating above  $T_g$ , small deformation of the contact region will create a finite contact surface. Subsequently a neck is formed due to the merging of both polymer particles at the contact surface and the disappearance of the intermediate liquid-air interface. Finally, neck growth occurs during which the particle doublet transforms its shape towards a single sphere under the driving force of surface tension. Within the resolution of the optical train, we can only analyze the neck growth stage of the sintering process, starting from neck radius to particle radius ratio's ( $x/a_0$ ) of 0.2, as shown in Figure 4.6. A gradual growth of the neck radius is observed in the image sequence. The images in Figure 4.6 also show that the particles remain pinned to the substrate during the major part of the sintering process as they do not liquefy completely. Only towards the end of the sintering process, wetting of the polymer on the substrate starts to occur, which is however halted rapidly due to solidification at the end of the laser pulse. For viscous sintering of liquid droplets, it has been shown that the wetting of the polymer on the substrate can affect the sintering kinetics, whereby enhanced wetting results in an acceleration of the sintering kinetics [154]. In our case, the substrate that is relevant for the actual sintering process in laser sintering would be polystyrene. However, the mirror polished steel substrate provides a twofold advantage: it facilitates the applied particle manipulation technique and also avoids stray reflections in the optical images. The wetting behavior of liquids on solids can be estimated from the wetting parameter  $S$ [154] :

$$S = \Gamma_s - \Gamma_{sl} - \Gamma_l, \quad (4.5)$$



---

with  $\Gamma_s$  the surface energy of the substrate,  $\Gamma_{sl}$  that of the substrate-liquid interface and  $\Gamma_l$  the surface tension of the liquid. If  $S > 0$  the liquid will favorably wet the substrate. Since stainless steel is a material with a very high surface energy, good wetting will be obtained. Similarly, polystyrene droplets will wet a polystyrene substrate. Hence, the wetting behavior of polystyrene droplets on a polystyrene substrate and a stainless steel substrate are expected to be similar, which was also experimentally verified. Thus, all further experiments were performed on the steel substrate, but are also representative for sintering of polystyrene on polystyrene.

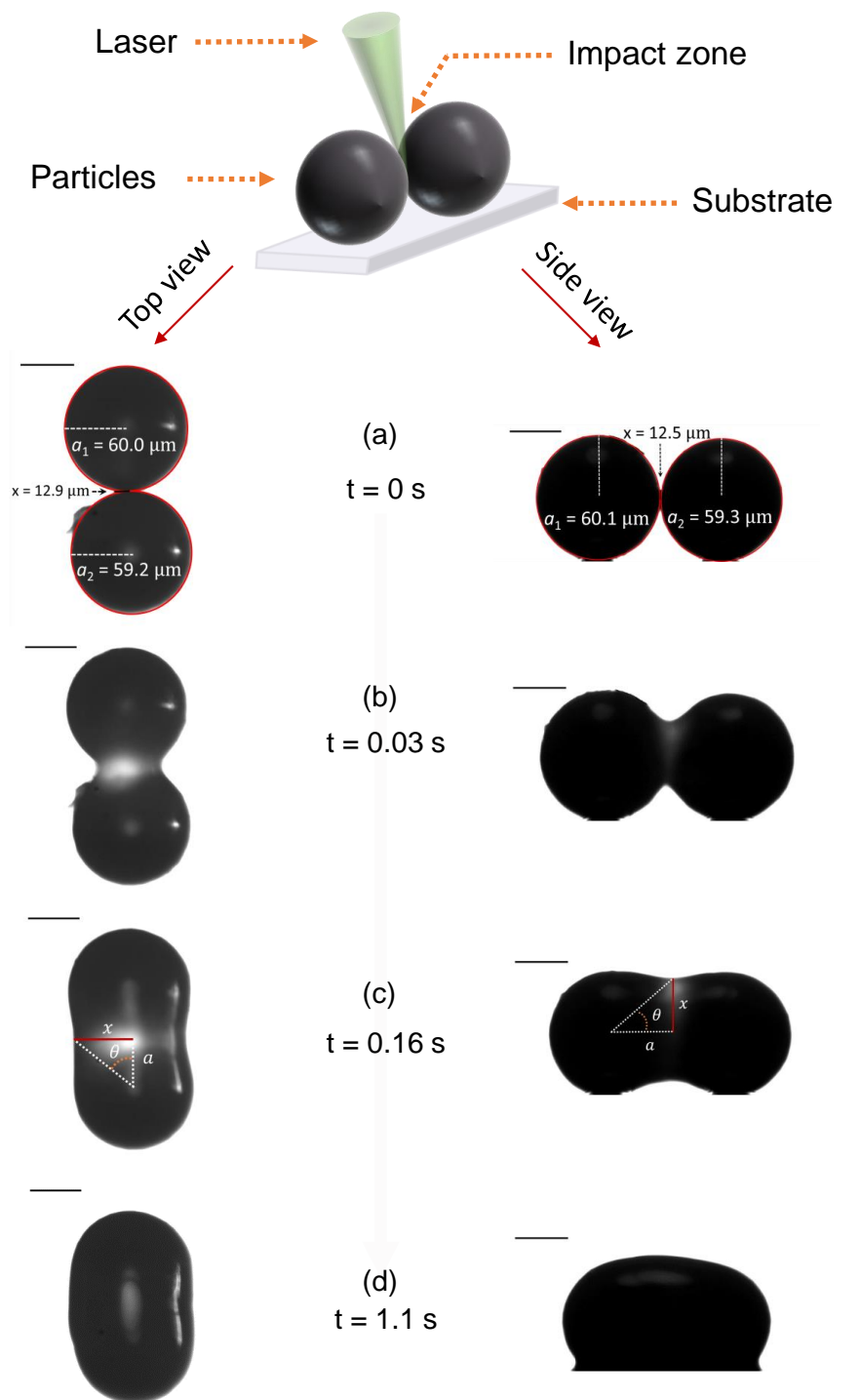


Figure 4.6: Image sequence of a typical sintering experiment with a particle radius of  $a_0 = 60 \mu\text{m}$ , heating chamber temperature of  $T_c = 53^\circ\text{C}$ , pulse energy of  $E_p = 28 \mu\text{J}$  and pulse duration of  $t_L = 800 \text{ms}$ .

Using the image sequence of Figure 4.6, the neck radius as a function of time is determined and is given in Figure 4.7(a) and Figure 4.7(b) for respectively the top and side view. The experimental reproducibility is very high, as is seen from the repeat experiments in Figure

4.7. Additional reproducibility checks at other values of the pulse energy are shown in Figure 4.15 in Appendix. Furthermore, Figure 4.7 shows that the kinetics exhibited in the top view and side view are identical. For all sintering experiments performed in this work, there was no systematic effect of analyzing the data from either the top or the side view. The final obtained neck radius was exactly the same in both cases. Therefore only the side view results are shown in the remaining part of the work, as they were captured with a faster camera. This axisymmetric behavior of the neck region and thus absence of any effects of the substrate on the sintering kinetics can most probably be attributed to the fact that the particle contact point with the substrate remains solid during the major part of the sintering process.

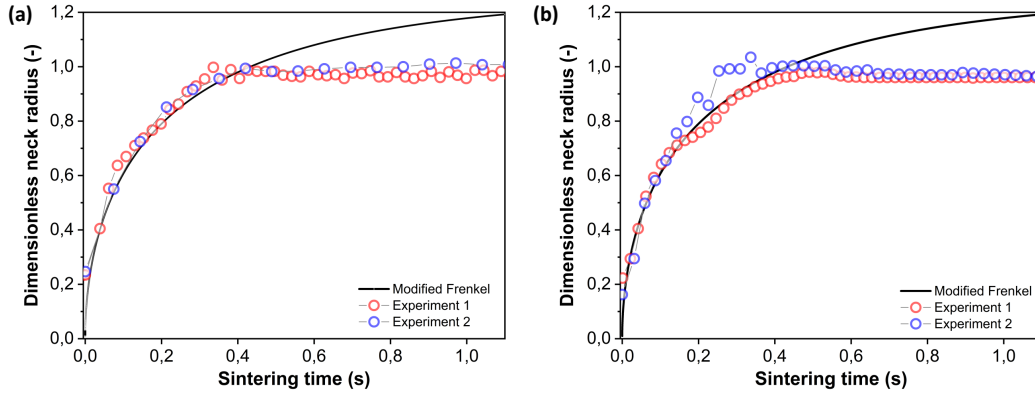


Figure 4.7: Dimensionless neck radius versus sintering time fitted with the modified Frenkel model (lines) with a particle radius of  $a_o = 60 \mu\text{m}$ , heating chamber temperature of  $T_c = 53^\circ\text{C}$ , pulse energy  $E_p = 28 \mu\text{J}$  and pulse duration of  $t_L = 800 \text{ms}$ . (a) top view, (b) side view.

The evolution of the neck radius in Figure 4.7 was fitted with the modified Frenkel model for viscous sintering of liquids under isothermal conditions, given by [120]:

$$\frac{d\theta}{dt} = \frac{\Gamma}{\eta a_o} \frac{2^{-5/3} \cos \theta \sin \theta}{K_1^2 (2 - \cos \theta)^{5/3} (1 + \cos \theta)^{4/3}}. \quad (4.6)$$

Here,  $\Gamma$  is the surface tension,  $\eta$  the viscosity,  $a_o$  the particle radius,  $\theta$  the angle between the line connecting the particle centers and that connecting a particle center with the extreme point of the neck, as indicated in Figure 4.6(c), and  $K_1$  is given by [121]:

$$K_1 = \frac{\tan \theta}{2} - \frac{\sin \theta}{6} \left[ \frac{2(2 - \cos \theta) + (1 + \cos \theta)}{(1 + \cos \theta) + (2 - \cos \theta)} \right], \quad (4.7)$$

which is the expression derived by Scribber et al. [121] for arbitrary  $\theta$  values. From  $\theta$  the dimensionless neck radius  $x/a_o$  can be obtained [120]:

$$\frac{x}{a_o} = \sin \theta \left( \frac{4}{(1 + \cos \theta)^2 (2 - \cos \theta)} \right)^{1/3}. \quad (4.8)$$

Thereby, the viscosity  $\eta$  was used as a fitting parameter. It can be seen from Figure 4.7 that this model is well suited to describe the initial sintering kinetics, even though it was developed for isothermal sintering of viscous liquids. The resulting fit value for the viscosity is 143 Pa·s, which with the given WLF parameters corresponds to a temperature of 122°C. Starting from a bed temperature of 53°C, the resulting temperature increase would require a total energy of 86  $\mu$ J per particle to heat up to 122°C, which is higher than the applied energy of 28  $\mu$ J thereby suggesting that both particles are not fully heated up to a homogeneous temperature. In addition, it suggests that the conversion from visible light energy to heat is rather efficient. At the last sintering stage, the modified Frenkel model predicts a final dimensionless neck radius of  $2^{1/3}$ , which is 1.26, and corresponds to a spherical particle with radius  $a_0 2^{1/3}$ . In the laser sintering experiment, the dimensionless neck radius levels off at a lower value since the particle doublet is not able to fully relax to a spherical droplet. This can be attributed to the limited energy supply, which hampers sufficient fluidity of the complete particles to retract into a spherical shape. During thermal sintering in a homogeneously heated chamber or upon continuous application of a three times higher laser energy, complete sintering up to a spherical droplet was observed.

It is interesting that, despite the expected non-isothermal characteristics of the sintering process, both in time as well as in space, the modified Frenkel model allows to capture the initial sintering kinetics rather well. Concerning the spatial distribution of the temperature profile, it should be noted that the ratio of laser spot radius (20  $\mu$ m) to particle radius (60  $\mu$ m) is 0.33 at this particle size, thereby a large area of the particles is illuminated. Moreover, the heat diffusion time from the laser illuminated area to the surrounding region of the particles can be estimated using the characteristic time for heat diffusion given by [122]:

$$t_c = \frac{(2a_0)^2}{\alpha} = \frac{(2a_0)^2 \rho c_p}{k}, \quad (4.9)$$

with  $\alpha$  the thermal diffusivity and  $\rho$ ,  $c_p$  and  $k$  respectively the density, heat capacity and thermal conductivity of PS. For a particle radius of 60  $\mu$ m,  $t_c$  equals 0.12 s. This indicates a relatively fast heat diffusion throughout the particles, which suggests that the neck region will most probably attain a relatively homogeneous temperature during sintering. However, even though spatial gradients within the sintering neck region are expected to be limited, temporal variations in temperature will be present due to the continuous heating of the neck region by the supplied laser energy.

#### 4.4.3 Effect of particle size

With the main characteristics of the sintering kinetics being set out in Section 4.4.2, the effects of several parameters relevant in laser sintering are systematically explored via experimental characterization of the sintering process. First, the particle size is varied, with the radii ranging between 30 and 105  $\mu$ m. This corresponds to the typical particle

size range of laser sintering materials [12]. The results for the neck growth kinetics presented in Figure 4.8 show two main effects. Firstly it can be seen that increasing the particle size substantially slows down the sintering kinetics. This is qualitatively the expected trend according to the scaling of the modified Frenkel model [120], as increasing the particle radius reduces the driving force originating from the surface tension which is maximal for a highly curved meniscus [155]. Second, Figure 4.8(a) shows that due to the slower sintering kinetics, only partial neck growth is attained by the time the laser pulse ends, which results in partially sintered doublets, as shown in Figure 4.8(b). During actual laser sintering, such partially sintered doublets would result in porosity of the printed parts.

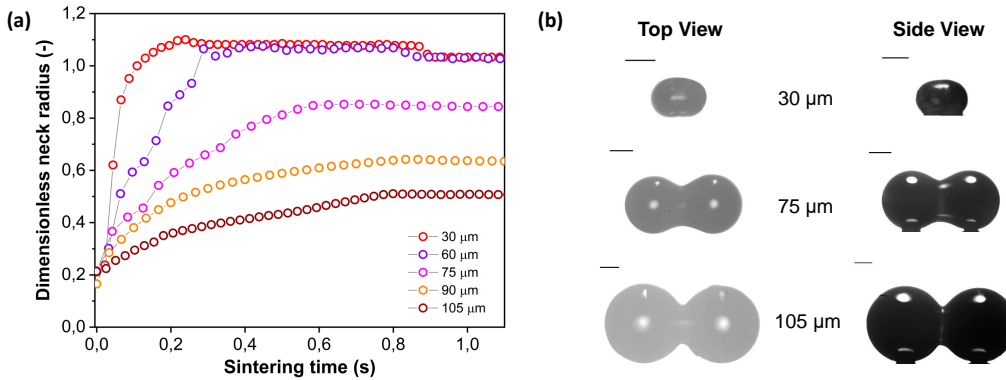


Figure 4.8: Effect of particle radius on sintering kinetics with heating chamber temperature of  $T_c = 53^\circ\text{C}$ , pulse energy  $E_p = 28 \mu\text{J}$  and pulse duration of  $t_L = 800 \text{ ms}$ . (a) Dimensionless neck radius in side view, (b) Particle doublets at the end of the sintering process.

To analyze whether the effects of particle radius follow the typical scaling of the modified Frenkel model, the sintering time is scaled with the characteristic Frenkel time ( $\eta_{s0} a_o / \Gamma$  with  $\Gamma$  the surface tension of polystyrene,  $\eta$  the viscosity and  $a_o$  the particle radius whereby  $\eta$  was kept the same as that obtained for a particle radius of  $60 \mu\text{m}$  in Figure 4.7), as shown in Figure 4.9(a). It can be seen that even after applying this scaling, the sintering of the larger particles is slower than that of the smaller ones. This indicates that the heat diffusion from the laser illuminated area to the surrounding particle region plays a significant role, as already concluded in Section 4.4.2. When increasing the particle radius from  $30$  to  $105 \mu\text{m}$ , the ratio of laser spot size to particle size decreases from  $0.66$  to  $0.19$ .

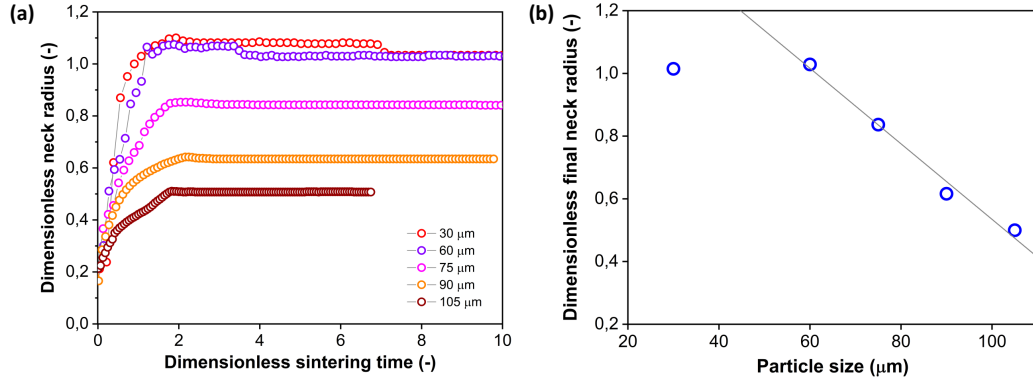


Figure 4.9: Effect of particle radius on sintering kinetics with heating chamber temperature of  $T_c = 53^\circ\text{C}$ , pulse energy  $E_p = 29 \mu\text{J}$  and pulse duration of  $t_L = 800 \text{ ms}$ . (a) Dimensionless neck radius in side view versus time rescaled with Frenkel timescale, (b) Dimensionless final neck radius versus particle size.

Since for large particles a larger part of the heat energy flows to the non-illuminated regions, the temperature increase in the neck region will be less, resulting in a higher viscosity and thus slower sintering kinetics. For the cases resulting in incomplete sintering, it can also be seen that the sintering kinetics slows down at the later sintering stages, thereby no longer allowing a description of the kinetics with the modified Frenkel model. This is caused by the effect of the transient rheology, resulting from the finite relaxation time of the polymer, which leads to a larger viscosity at later timescales, for which complete sintering is already obtained in the case of smaller particles. At the end of the laser pulse (at  $t = 800 \text{ ms}$  in Figure 4.8(a)), an almost instantaneous solidification of the neck region is noticed. This phenomenon is analyzed by an estimation of the cooling rate of the particles. First, an estimation of the Biot number [122]:

$$Bi = \frac{hL_c}{k} = \frac{h(a_o/3)}{k}, \quad (4.10)$$

with  $h$  the heat transfer coefficient,  $k$  the thermal conductivity,  $L_c$  the characteristic length scale which is defined as volume/surface area and  $a_o$  the particle radius, allows to judge the relative contributions of external convection and internal heat conduction. Due to the small length scales involved,  $Bi \ll 0.1$  and once the laser is switched off, the cooling of the particle will occur more or less homogeneously throughout the particle without the generation of additional temperature gradients within the particle. Moreover, the timescale for cooling can be estimated from an energy balance considering only heat loss due to convection:

$$mc_p \frac{dT_p}{dt} = hA(T_p - T_c), \quad (4.11)$$

in which  $m$  is the particle mass,  $c_p$  the heat capacity,  $T_p$  the particle temperature,  $h$  the heat transfer coefficient,  $A$  the particle surface area and  $T_c$  the temperature of the heating chamber. Using a typical value for  $h$  of  $50 \text{ W/m}^2\text{K}$  (Section 4.4.7), it can be

calculated that cooling from the estimated sintering temperature of 122°C occurs rather fast whereby more than 10°C temperature drop is obtained within 100 ms. Moreover, especially in case of fully sintered particles with a large contact area between the particles and the substrate, additional heat loss to the heating chamber substrate will occur. The final reached neck radius is an important characteristic of the final sintered product and the dimensionless final neck radius ( $x_f/a_o$ ) is provided as a function of the particle radius in Figure 4.9(b). It can be seen that once incomplete sintering is obtained, the final dimensionless neck radius decreases approximately linearly with the overall particle radius. The sintering process is halted when the polymer viscosity exceeds a critical value whereby the work of the surface tension becomes insufficient to overcome the viscous loss during flow [120]. Since the evolution of the polymer viscosity with time critically depends on the different rheological parameters of the material, the exact relation between the final dimensionless neck radius and the particle size will depend on the polymer rheology.

#### 4.4.4 Effect of heating chamber temperature

The optimal heating chamber temperature in selective laser sintering is generally considered to be the highest temperature that does not result in consolidation of the powder outside the laser area. This way, the required laser energy is minimal whereas thermal gradients and thermal expansion are also minimized [12]. The effect of varying the heating chamber temperature from close to  $T_g$  to far below it, keeping all other parameters fixed, is depicted in Figure 4.10. A priori, two effects of decreasing the heating chamber temperature would be expected. With a lower heating chamber temperature and at the same laser energy, the temperature in the sintering region would be lower, resulting in a higher viscosity and thus lower sintering speed. In addition, once the laser energy is not sufficient anymore to heat the polymer above the glass transition temperature, solidification and cessation of the sintering will be observed. It can be seen in Figure 4.10 that mainly at the lowest heating chamber temperature of 30°C, the initial sintering speed is significantly slowed down. However, the reduction of the sintering speed is much less as compared to what would be expected from the increase of the steady state viscosity due to a temperature reduction of 23°C in the sintering region (as can be derived from a scaling of the x axis with the Frenkel timescale taking into account the steady state viscosity effect being 143 Pa·s at 122°C versus 2094 Pa·s at 99°C, results not shown). This is caused by the fact that during the initial stages of sintering, the effect of temperature on the viscosity can be much less as compared to the temperature effect at steady state. For the other heating chamber temperatures, the lower sintering kinetics is only noticed at timescales above 200 ms, which may indicate that initially the limiting step is the distribution of heat to the particle region outside the laser spot area. Moreover, at timescales that are sufficiently short with respect to the polymer relaxation time, the effects of temperature on the viscosity can become insignificant. This is caused by the fact that increasing the temperature lowers both the steady state viscosity as well as the relaxation time [156]. The dependence of the final obtained dimensionless neck radius on the heating chamber temperature is depicted in Figure 4.10(b). It can be seen that

the sensitivity to the heating chamber temperature is rather limited within a relatively wide range of heating chamber temperatures.

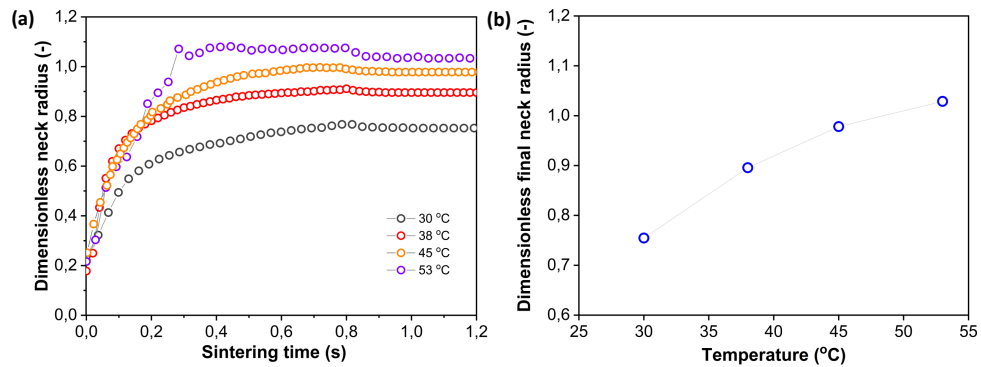


Figure 4.10: Effect of heating chamber temperature on sintering kinetics with pulse energy of  $T_c = 53^\circ\text{C}$ , pulse energy  $E_p = 29 \mu\text{J}$  and pulse duration of  $t_L = 800 \text{ ms}$ . (a) Dimensionless neck radius in side view, (b) Dimensionless final neck radius versus heating chamber temperature.

#### 4.4.5 Effect of pulse duration

A third parameter that is of relevance during laser sintering is the laser pulse duration. With typical scanning speeds ranging between 10 and 1000 mm/s and particle diameters in the range of 50 to 500  $\mu\text{m}$  [12], the typical duration of laser impact on a particle is in the range of 0.05 to 50 ms. However, since the laser scan spacing is mostly chosen about 3 to 6 times smaller than the laser beam diameter, the effective laser impact time on each location is larger [12]. To be able to perform a systematic study of the effects of laser pulse duration, we selected a range of pulse durations, ranging from much shorter than the characteristic sintering time, to longer than this time. The total energy within each pulse was kept constant. Figure 4.11(a) demonstrates that the main effect of shorter pulse durations is a premature cessation of the neck growth process occurring nearly instantaneously after switching of the laser pulse. On the other hand, even though at the same total pulse energy the longest pulse duration corresponds to a more than tenfold lower power as compared to the shortest pulse (0.036 versus 1.16 mW), the kinetics of the growth of the neck radius is relatively insensitive to this parameter. This may suggest that at the shortest pulse durations the limiting factor for the kinetics is the distribution of the heat over the sintering area rather than the effective laser power. In addition, the higher instantaneous laser power would result in larger temperature gradients within the particle doublet, thereby leading to more heat flow to the outer particle regions as compared to the case in which there is a slower heating of the sintering region. In addition, during the initial sintering stages, the effect of temperature on the polymer viscosity can be very limited, even though the steady state viscosity shows a high temperature dependence. The dependence of the final obtained neck radius as a function of laser pulse duration is shown in Figure 4.11(b). Since the sintering kinetics is relatively insensitive to the applied laser pulse duration (or correspondingly the laser power), the dependence of the final dimensionless neck radius  $x_f/a_0$  follows a similar



trend as  $x/a_0$  for the case of the longest applied pulse duration. This is caused by the fact that the final neck radius is only determined by the timepoint at which sintering was halted by the end of the laser pulse. These results clearly show that, using the same total pulse energy, distributing this energy over a longer time results in more efficient sintering.

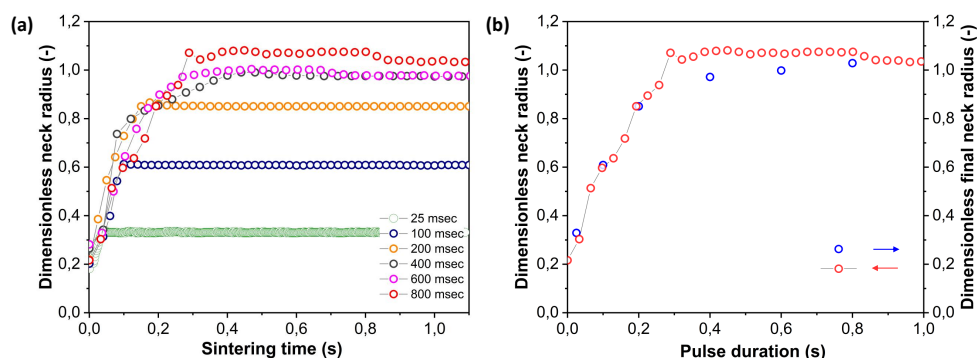


Figure 4.11: Effect of pulse duration on sintering kinetics with heating chamber temperature of  $T_c = 53^\circ\text{C}$ , pulse energy  $E_p = 29 \mu\text{J}$  and pulse duration of  $t_L = 800 \text{ ms}$ . (a) Dimensionless neck radius in side view, (b) Dimensionless final neck radius versus pulse duration.

#### 4.4.6 Effect of laser energy

Finally, the laser sintering process is affected by the laser energy. As typical spot sizes in commercial laser sintering devices are much larger than  $40 \mu\text{m}$ , the fluence or laser energy per unit area will be used for comparison purposes. In the present work, the laser energy values were varied between 19 and  $29 \mu\text{J}$ , which corresponds to fluence values of 3800 to  $5800 \text{ J/m}^2$ . For amorphous polymers such as polystyrene, typical values of the fluence can be estimated from the laser power, scan speed and scan spacing, which for instance results in a value of the order of 2000 to  $3000 \text{ J/m}^2$  for the sintering of high impact polystyrene [134]. Figure 4.12 shows that decreasing the laser energy at constant pulse duration (thus reducing the laser power from 0.036 to 0.024 mW) results in a slowing down of the sintering kinetics for the lowest pulse energies whereas for the highest values, the initial slope remains the same up to 200 ms, which corresponds to the trend observed in Figure 4.11 showing the effect of pulse duration, for values resulting in higher power values as those in Figure 4.12. This suggests that there is a critical power value above which the power is no longer the limiting factor for the initial stages of the sintering process. At the lowest applied laser energy values, the initial sintering kinetics is slower but it also appears that sintering is nearly halted already before the end of the laser pulse (at 800 ms). This suggests that the supplied energy is so low that the viscosity decrease due to the increase in temperature is less pronounced than the viscosity increase due to transient effects. Hence, sintering can only occur in the initial stages when the driving force is very large due to the high curvature and viscosity buildup is still ongoing whereas after some time, sintering slows down substantially due to the high viscosity. Figure 4.12(b) shows the evolution of the final dimensionless neck

radius with the applied laser energy. The dependence on laser energy is very strong in the studied range of energy values whereby the lowest values are clearly not enough to obtain a sufficient temperature increase for sintering. A linear relation between the laser energy and the dimensionless final neck radius is obtained for the whole range of relevant laser energies, ranging from those resulting in nearly no sintering to those leading to complete sintering. However, similar to the effects of particle size, the exact relation between both parameters depends on the complex time and temperature dependent rheology of the polymer.

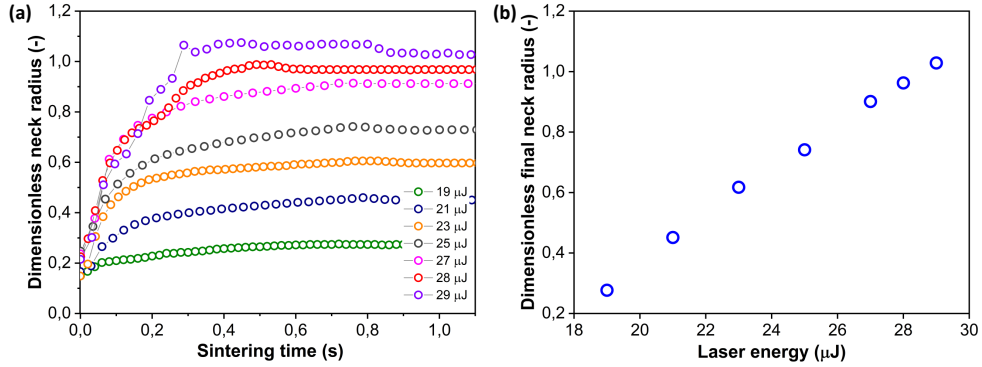


Figure 4.12: Effect of laser energy on sintering kinetics with a heating chamber temperature of  $T_c = 53^\circ\text{C}$ , pulse duration of  $t_L = 800$  ms and particle radius of  $a_o = 60$   $\mu\text{m}$ . (a) Dimensionless neck radius in side view, (b) Dimensionless final neck radius versus laser energy.

#### 4.4.7 Main physical phenomena summarized in a non-isothermal sintering model

Up to now, viscous sintering models were used to describe the sintering kinetics in case of isothermal sintering processes in a heated chamber. However, as mentioned above, during laser sintering, a continuous increase of the temperature of the neck region is expected. Since such a temperature evolution results in a changing rheological behavior during sintering, this should be taken into account in the sintering model. Scribber et al. [121] generalized the modified Frenkel model to become valid for any rheological constitutive equation, resulting in:

$$\frac{a_o 2^{2/3} K_1}{3\Gamma} (\tau_{xx} - \tau_{yy}) \frac{(1 + \cos \theta)^{4/3} (2 - \cos \theta)^{5/3}}{\cos \theta \sin \theta} - 1 = 0, \quad (4.12)$$

with  $a_o$  the particle radius,  $\Gamma$  the surface tension,  $\tau_{xx}$  and  $\tau_{yy}$  the normal stresses in two perpendicular directions and  $K_1$  as defined in Figure 4.7. In the model derivation, it was assumed that sintering results in a purely biaxial extensional flow with a homogeneous extension rate throughout the fluid volume. Hence, the extension rate  $\dot{\epsilon}$  depends on the sintering kinetics, according to [120]:

$$\dot{\epsilon} = K_1 \frac{d\theta}{dt}. \quad (4.13)$$

Since the stress values in Eqn. 4.12 depend on the rheological parameters as well as the extension rate, the rheological constitutive equation and sintering equation thus form a coupled set of equations. Based on Eqn. 4.13 and the sintering kinetics shown in Figure 4.7, extension rates in our study range up to  $4 \text{ s}^{-1}$ , depending on the applied laser sintering conditions. Hence, a full analysis of the sintering problem would require a non-linear constitutive equation, as quasi-linear models such as the upper convected Maxwell model may fail due to the fact that the extensional viscosity becomes unbounded for  $\dot{\epsilon} > 1/(s\lambda)$  [156]. However, in that case, a full numerical approach, such as applied in the work of Baemans et al. [97], using a finite element method, might be more suitable. Hence, we neglect non-linear rheological effects and describe the rheology of the polymer with the linear viscoelastic Maxwell model. Thereby, qualitative insights in the effects of the different laser sintering parameters on the neck growth process, via their effects on the polymer rheology, will be provided. In the linear viscoelastic case, the rheology and sintering kinetics is decoupled. Hence, first the evolution of the viscosity with time is calculated from the Maxwell model with temperature-dependent parameters:

$$\tau(T, t) + \lambda(T) \frac{d\tau(T, t)}{dt} = 2\eta_s(T) \mathbf{D}, \quad (4.14)$$

in which  $\tau$  is the stress tensor,  $\mathbf{D}$  the rate of deformation tensor,  $\lambda$  the relaxation time and  $\eta_s$  the steady state viscosity. As shown in Figure 4.4, the PS polymer behaves thermorheologically simple, hence the temperature dependence of  $\eta_s$  and  $\lambda$  can be described by means of the temperature shift factor  $a_T$  (Eqn. 4.2). The resulting viscosity evolution with time is governed by two counteracting effects. Gradual heating of the particles leads to a decrease of the viscosity with time. Simultaneously, the finite relaxation time of the polymer causes a viscosity buildup with time. The resulting viscosity  $\eta$  as a function of time, defined as:

$$\eta(t) = \frac{\tau_{xy}(t)}{\dot{\gamma}}, \quad (4.15)$$

with  $\dot{\gamma}$  the shear rate and  $\tau_{xy}$  the shear stress, is substituted in Eqn. 4.6, which is equivalent to Eqn. 4.12 when a linear viscoelastic constitutive equation is used.

To determine the evolution of the temperature as a function of time during the heating by means of the laser pulse, an energy balance is used. First, it should be noted that due to the limited temperature difference between the particles and the heating chamber, heat loss by radiation is negligible as compared to that by convection [122]. Hence, the temperature evolution of the particles is governed by the supplied laser energy and the heat loss to the environment by means of free convection:

$$\alpha mc_p \frac{dT_p}{dt} = \delta P - \beta hA(T_p - T_c), \quad (4.16)$$

in which  $m$  is the particle mass,  $c_p$  the heat capacity,  $T_p$  the particle temperature,  $P$  the power of the laser given by the pulse energy  $E_p$  divided by the pulse duration  $t_L$ ,  $h$  the heat transfer coefficient,  $A$  the particle surface area and  $T_c$  the temperature of the heating chamber. The parameters  $\alpha$ ,  $\delta$ , and  $\beta$  allow to correct for the facts that not the complete particle is heated, that the conversion from laser energy to heat energy is not complete and that there may be additional heat loss to the environment by conduction into the heating chamber substrate. The heat transfer coefficient can be estimated from heat transfer correlations for free convection over an object. Based on the dimensionless Rayleigh number, which is of the order of  $10^{-6}$  for the studied conditions, it is concluded that buoyancy-driven flows are negligible and heat transfer is dominated by conduction [122]. In that case, the heat transfer coefficient is obtained from the fact that the Nusselt number  $Nu$  for conduction equals two with:

$$Nu = \frac{hD}{k}, \quad (4.17)$$

and  $h$  the heat transfer coefficient,  $D$  the characteristic length scale which is in this case the particle diameter and  $k$  the thermal conductivity of air [122]. This results in a value for the heat transfer coefficient of the order of 50 W/m.K. Depending on the contact area between the particle and the heating chamber substrate, additional heat loss to the heating chamber substrate may play a role, which can be taken into account by means of parameter  $\beta$  in Eqn. 4.16. From the energy balance as stated in Eqn. 4.16, the temperature evolution in the particle can be obtained:

$$T_p(t) = \frac{\delta P}{\beta hA} \exp\left(\frac{-\beta hAt}{\alpha mc_p}\right) + T_c + \frac{\delta P}{\beta hA}, \quad (4.18)$$

Using this model, the effect of the various parameters that affect the sintering process, namely the particle size, heating chamber temperature, laser energy and laser pulse duration can be investigated. Model predictions are calculated for the sintering parameters shown in Figure 4.7, using the reference viscosity and reference relaxation time obtained in Section 4.4.1 and keeping the correction factors  $\alpha$ ,  $\beta$  and  $\delta$  in Eqn. 4.16 and Eqn. 4.18 at one. The results for the temperature and viscosity evolution as a function of time for various values of the laser pulse energy are shown in Figure 4.13(a) and Figure 4.13(b). Figure 4.13(a) demonstrates that increasing the laser energy results in a more pronounced temperature increase. Moreover, after a certain time, the particle temperature becomes so high that the heat loss equals the energy supplied by the laser and thus the temperature reaches a plateau value. The corresponding viscosity evolution is shown in Figure 4.13(b). In general, the viscosity exhibits an increasing trend as a function of time, which is caused by the transient effects from the polymer relaxation time. With increasing temperature, the rising trend of the viscosity becomes less pronounced. However, the temperature effects at initial times are clearly less pronounced than those at

later times and under steady state conditions. When the supplied energy is high enough, the viscosity even exhibits a non-monotonous trend, with first an increase due to the dominant effect of viscoelasticity followed by a decrease due to the dominant effect of the temperature rise.

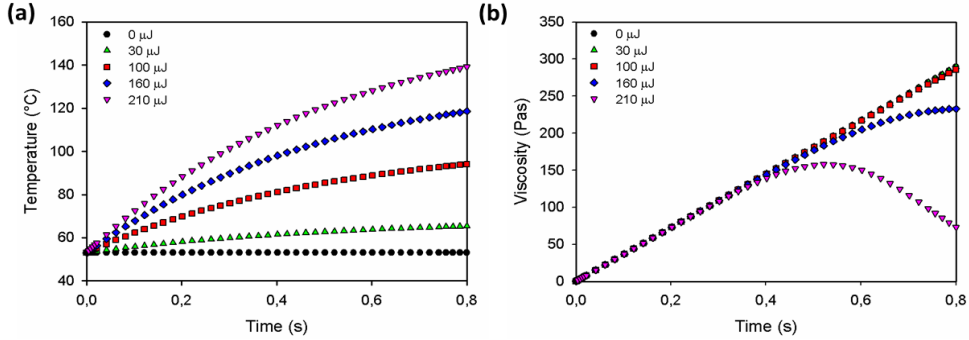


Figure 4.13: Model predictions at various laser energies for (a) temperature and (b) viscosity as a function of time for a particle radius of  $a_o = 60 \mu\text{m}$ , heating chamber temperature of  $T_c = 53^\circ\text{C}$ , pulse duration of  $t_L = 800 \text{ ms}$ ,  $\eta_{\text{ref}} = 2119 \text{ Pa}\cdot\text{s}$ ,  $\lambda_{\text{ref}} = 6.1 \text{ s}$ ,  $\alpha = 1$ ,  $\beta = 1$  and  $\gamma = 1$ .

Figure 4.14(a) shows the sintering kinetics for the parameter values for which the temperature and viscosity evolution are shown in Figure 4.13(a) and Figure 4.13(b). This figure clearly indicates that using the experimental parameter values, the obtained sintering kinetics is much faster as compared to the behavior observed in the experiments. This discrepancy can most probably be attributed to the fact that the solid polymer behavior below  $T_g$  is not incorporated in the model and the liquid behavior and corresponding viscosities and relaxation times at these temperatures are extrapolated from the WLF behavior, which does not hold below  $T_g$ . Hence, whereas our model predicts an initial viscosity of zero that builds up with a very long relaxation time, the actual polymer will be a viscoelastic solid during the initial stages of sintering. Due to the pronounced sintering at very short sintering times, the final obtained dimensionless neck radius is nearly independent of the supplied laser energy in this case. By reducing the relaxation time of the polymer, a faster increase of the viscosity results, as shown in Figure 4.14(b). This faster viscosity buildup suppresses the sintering, as shown in Figure 4.14(a). Since the model predictions do not allow to quantitatively match the experimental sintering behavior, the model can not be used to describe the experimental data but rather to indicate the relevant governing phenomena.

In conclusion, the performed model calculations indicate that the balance between the relaxation time and the temperature dependence of the viscosity has a significant contribution to the sintering behavior. Faster sintering is obtained when the polymer viscosity is low. A low viscosity can be obtained from a steady state viscosity that drops significantly with increasing temperature but also from a large relaxation time that provides slow viscosity buildup. Since in typical polymers both the viscosity and the relaxation time show a similar drop with increasing temperature, use of more complex materials,

e.g. multiphasic materials, is expected to allow enhanced optimization of the material rheology for the laser sintering process. From the point of view of process parameters, it can be concluded that the various parameters that affect the sintering kinetics all act through changes of the temperature and thereby viscosity of the material. Hence, a correct understanding and modelling of the temporal and spatial temperature profiles is crucial to capture the actual sintering kinetics. Clearly, due to the complex interaction between temperature and time-dependent rheological behavior, merely increasing the temperature by using a higher laser power or chamber temperature, does not always improve the sintering speed, which is counter-intuitive.

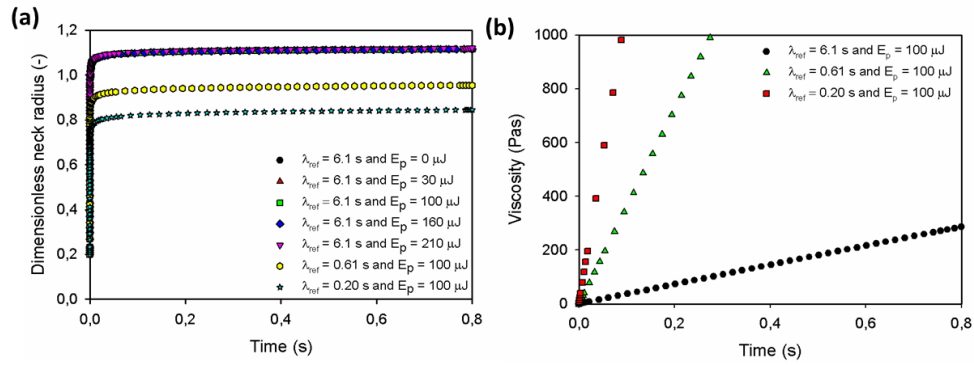


Figure 4.14: Model predictions for (a) dimensionless neck radius versus time for a particle radius of  $a_o = 60$   $\mu$ m and (b) viscosity versus time, heating chamber temperature of  $T_c = 53^\circ\text{C}$ , pulse duration of  $t_L = 800$  ms,  $\eta_{ref} = 2119$  Pa·s,  $\lambda_{ref} = 6.1$  s,  $\alpha = 1$ ,  $\beta = 1$  and  $\gamma = 1$ .

## 4.5 Conclusions

Laser sintering of polystyrene is studied on the scale of a single particle doublet by using a novel in-house developed experimental setup. This setup allowed the particle doublet to be subjected to a well-defined laser pulse while performing optical visualization of the growth of the neck radius between the particles, both from the top as well as from the sides. A visible light laser modulated with an acousto-optic modulator was used to create laser pulses focused on the particle doublet with a well-defined small spot size. Thereby, the scanning of the laser over the particles in the actual laser sintering devices can be mimicked. By using spherical polystyrene particles of various sizes the ratio of laser spot size to particle size was varied between 0.66 and 0.19. The thermal, rheological and laser light absorption properties of the used polystyrene were characterized a priori. This allowed the determination of the suitable parameter range for the heating chamber temperature, laser pulse duration and laser pulse energy. Subsequently, a systematic study of the effects of the main laser sintering parameters on the sintering dynamics, quantified as the evolution of the neck radius between both particles with time, was performed. This allowed, for the first time, the provision of time-resolved information on the laser sintering of polymer particles. The initial sintering kinetics as a function of time can be described with the modified Frenkel model for isothermal sintering of viscous

liquids, whereby the characteristic viscosity depends on the applied process conditions. However, the overall sintering kinetics is determined by a complex interplay between the temperature and time effects on the viscosity. Contrary to thermal sintering in a homogeneously heated chamber, laser induced particle sintering can slow down and even completely halt at later stages. This is caused by the viscosity build-up as a function of time due to the finite relaxation time of the material. Hence, if the supplied laser energy is not sufficient to cause a substantial temperature increase, only partial sintering occurs. Considering the complexity of the sintering process that is characterized by a non-uniform and time-dependent temperature profile as well as complex flow fields, further studies will involve a combination of experimental and numerical work to provide complementary information on the global as well as local scale. Moreover, the effects of the presence of surrounding particles on the sintering kinetics will be studied to be able to extend our results to actual sintering in a polymer powder bed. In the case of viscous sintering, it has already been shown that the sintering of nearby particles affects the kinetics[157]. Finally, since laser sintering of polymers often concerns semicrystalline materials, the experimental approach will be extended to allow in situ characterization of the crystallization process during sintering.

## Acknowledgements

This work forms part of the research programme of the Brightlands Materials Research Centre (BMC). We thank ICMS, TU Eindhoven, for providing us with the rendered image and animation of the experimental setup. Loek Trimbach is acknowledged for the development of the Matlab<sup>®</sup> code for image analysis.

## Appendix

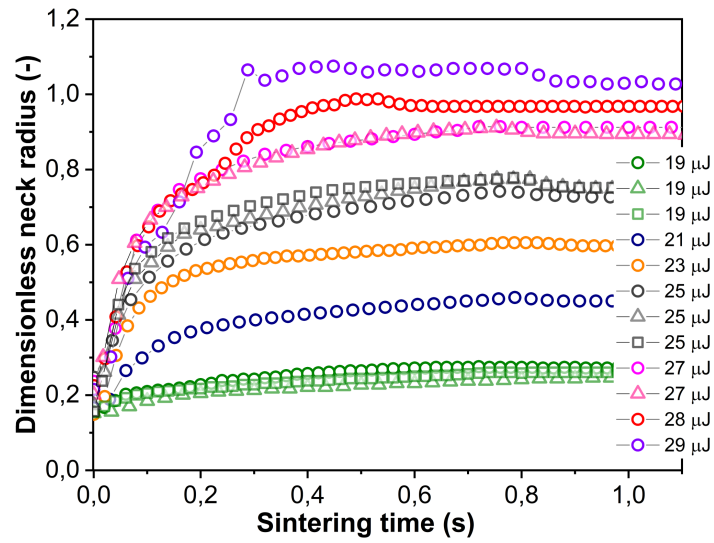


Figure 4.15: Effect of laser energy on sintering kinetics with heating chamber temperature  $53^{\circ}\text{C}$ , pulse duration 800 ms and particle radius  $60\ \mu\text{m}$ , side view data. Repeat experiments shown at 19, 25 and  $27\ \mu\text{J}$ .





## Laser sintering of PA12 particles studied by *in-situ* optical, thermal and X-ray characterization

### Abstract

Microstructure of products manufactured by selective laser sintering (SLS) are known to be highly dependent on various process and material parameters, which can influence the final part property. While most work has been focused on *ex-situ* characterization of a printed part, little is known about the time-dependent microstructure development during the sintering process. In this work, we present the direct observation of microstructural evolution during laser sintering of Polyamide 12 (PA12) particle doublets by *in-situ* synchrotron Wide Angle X-ray Diffraction (WAXD), using our in-house developed laser sintering setup. A transition from  $\alpha'$ -phase at high temperature to  $\gamma$ -phase is observed for varying chamber temperature. The complex interplay between rheology and temperature dependent effects are observed for varying particle sizes with IR imaging. We show that isothermal crystallization experiments are not sufficient to describe a non-isothermal process like SLS, and that size effects can influence the flow and crystallization kinetics. A correlation is drawn based on the critical Weissenberg number estimated for repetition and Rouse time scales. Furthermore, a microstructure survey has been carried out by microtoming thin slices of these sintered doublets.

### 5.1 Introduction

Additive manufacturing has traditionally been used for prototyping of products with specific requirements. Research and development over the past decade has shown potential in these techniques to move from prototyping towards mass manufacturing. Importance

---

*Largely reproduced from:*

1) Hejmady, P., van Breemen, L. C. A., Anderson, P. D., & Cardinaels, R. Laser sintering of PA12 particles studied by in-situ optical, thermal and X-ray characterization. *submitted to Additive Manufacturing*.

has grown in automotive, instrumentation as well bio-medical sectors where demands are specific to individual consumer's need [158, 159, 160, 161, 162]. In particular, powder-based technique for polymers, such as selective laser sintering (SLS) thus far is capable of generating parts with acceptable properties, thus gaining more interest [163, 164, 165]. Materials used in SLS are in powder form, which are spread in thin layers in a temperature controlled chamber. The process mainly uses a laser as heat source to raise the material above its melting temperature allowing to selectively melt the powder, joining powders for given predetermined size and shape of the product [77, 87, 166].

Up to now, extensive research has been done in optimizing the SLS process, to produce dense parts and understanding behind the physical process involving laser-material interaction are not well understood, considering industrial SLS setups do not allow visualization of the process.

Apart from final part property being limited by material property, it has been shown that process variables like, heating chamber temperature, laser power, scan speeds can influence the consolidation behavior of the powder particles and the resulting microstructure obtained [135, 167]. Intrinsic defects within the part, like poor layer-to-layer and porosity can arise if the process parameters are not optimized, leading to parts with poor mechanical properties [2, 134, 137]. Furthermore, powder morphology plays a significant role on the final properties and even using the same powder resulted in significant difference in part properties [168]. Therefore, fundamental information is still limited to final structure obtained after sintering process which is SLS machine dependent, since process condition vary between manufacturers. To tailor the process condition, insight on structure development during laser sintering process is desired, which is unavailable.

The range of materials suitable for processing by this technique is very much restricted to polyamide 12 (PA12) [12, 169]. Due to its narrow melting range and broad processing window, it is the ideal material for laser sintering while avoiding premature coalescence of the particles [24, 170, 171]. It has been shown, depending on the final temperature and cooling rate, PA12 undergoes a phase transition and the crystal phase obtained highly depends on cooling conditions [112]. PA12 undergoes a complex polymorphism, where under slow cooling condition  $\gamma$ -phase was the most stable phase, characterized by a hexagonal unit cell with only one strong WAXD reflection at d-spacing of 0.42 nm [124, 125]. Studies have been performed using calorimetric techniques to investigate the cooling process and its influence on crystallization kinetics [172, 173]. The  $\alpha'$ -phase was reported for the first time by Ramesh et al. [126] as the most stable crystalline phase at high temperatures. Quenching from the melt state leads to the formation of a mesomorphic structure which transforms into  $\gamma$ -phase upon annealing. But these studies do not consider the influence of flow, since polymer particles undergo deformation within short time scales during laser sintering process. It has been shown that flow and temperature can influence the crystal morphology and the resulting mechanical properties [174, 175, 176].

Thermal imaging systems have been utilized to understand a relationship between processing condition to the part properties obtained [177]. An in-homogeneous temperature profile was observed over the melt pool surface and in addition it has been reported that

particles undergo non-isothermal temperature profiles during laser sintering [9, 10, 145]. The consequence of in-homogeneous cooling can result in a varying crystal microstructure [178] along the part, and induce part warpage resulting in deviations of geometry and irreproducible properties [25]. Therefore understanding of the microstructure property can further supplement the ongoing development [10, 179].

Hot-stage microscopy experiments have been investigated, where temperature-dependent sintering rate were studied for polymer particle doublets [93, 94, 180], by tracking the neck growth between these particle doublets.

But no study has been found in literature which links, in real time, the flow and non-isothermal temperature profile observed during laser sintering process to the crystallization kinetics. Our approach is to provide fundamental understanding on the sintering process using our in-house developed setup [82], for doublets of PA12 particles. The geometric observation of a two-particle system allows a simplistic description of the SLS process and provides relevant process parameters. Fundamental underlying mechanism during sintering of two equally sized polyamide 12 particles will be provided by *in-situ* time resolved experiments, correlating flow by optical microscopy, temperature by infra red imaging to the obtained microstructure by X-ray measurements, simultaneously.

## 5.2 Materials and methods

### 5.2.1 Material

Polyamide 12 (Vestamide L-1700) was obtained in pellet form and free from additives. PA12 was colored black by adding 2 wt% of Nubian Black PC-0870 dye (Orient Chemical Industries co., Ltd) through solution mixing in benzylalcohol at 120°C. This resulted in 91% absorption of visible light at a wavelength of 532 nm for a sample thickness of 100  $\mu\text{m}$ . Subsequently, spherical PA12 particles of various diameters ranging between 100  $\mu\text{m}$  and 200  $\mu\text{m}$  were prepared by grinding followed by a thermal annealing protocol as described in Chapter 2 [181].

### 5.2.2 Material characterization

#### 5.2.2.1 DSC and Rheology

Differential scanning calorimetry (Mettler Toledo 823e/700) was performed at a heating rate of 10°C/min on PA12 with 2 wt% dye to determine the peak melting temperature and the melting enthalpy from second heating run, as shown in Figure 5.1(a). The DSC was calibrated for the heat flux and melting enthalpy with indium. PA12 has a peak melting temperature  $T_m$  of 178°C with a melting enthalpy of 56.4 J/g. Rheological measurements were performed on a stress-controlled rotational rheometer (MCR502 from Anton Paar) with a plate-plate geometry (diameter 25 mm) in a nitrogen-flushed

convection oven. Measurements were carried out in the linear viscoelastic regime, which was determined by a preliminary strain sweep test (at 1 Hz). Time-temperature superposition of data obtained over a range of temperatures, leads to a master curve at a reference temperature of 200°C, as shown in Figure 5.1(b). Since viscosity plays an important role during the sintering process [175], the complex viscosity is determined from the frequency sweep experiments, whereby the temperature dependence of the zero-shear viscosity is given by [113]:

$$a_T = \frac{\eta(T)}{\eta(T_{\text{ref}})} = \exp\left(\frac{E_a}{RT}\right). \quad (5.1)$$

With  $a_T$  the temperature shift factor,  $\eta(T)$  and  $\eta(T_{\text{ref}})$  the viscosities at the actual and reference temperature respectively,  $E_a$  the activation energy and  $R$  the universal gas constant. From the shift factors, the activation energy was calculated to be  $E_a = 32.5$  kJ/mol.

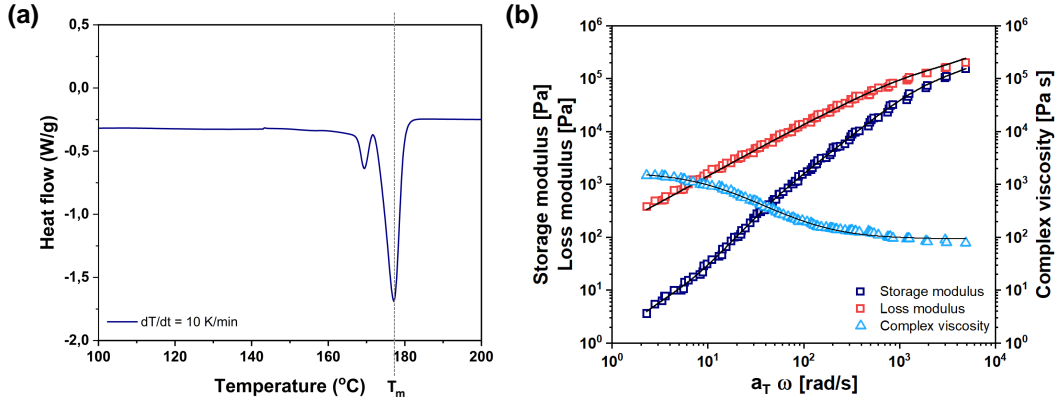


Figure 5.1: (a) DSC thermograph (heating cycle) of PA12 containing 2 wt% dye. (b) Master curve for dynamic moduli of PA12 containing 2 wt% dye at a reference temperature of 200°C obtained from frequency sweep measurements at 162°C, 170°C, 180°C, 190°C, 200°C and 210°C. The viscosity curve is fitted with a cross model and the dynamic moduli with a multimode Maxwell mode (lines).

The shear rate dependency of the viscosity is captured by the Cross model [152]:

$$\eta_s = \eta_{s,\infty} + \frac{\eta_{s0} - \eta_{s,\infty}}{1 + (\lambda\dot{\gamma})^m}, \quad (5.2)$$

with model parameters  $\eta_{s0} = 1702$  Pa·s,  $\eta_{s,\infty} = 93$  Pa·s,  $\lambda = 0.085$  and  $m = 1.22$ . Multimode Maxwell model [152] fitting of the small-amplitude dynamic moduli provides the relaxation time distribution of the polymer, as shown in Table 5.4 in Appendix I for the reference temperature of 200°C. The viscosity average relaxation time defined as:

$$\lambda = \frac{\sum_{i=1}^k \lambda_i \eta_i}{\sum_{i=1}^k \eta_i}, \quad (5.3)$$

with  $\lambda_i$  the relaxation time of mode  $i$  and  $\eta_i$  the viscosity contribution of mode  $i$ , is given in Table 5.1 for various temperatures. It ranges from 14.4 to 0.8 s in the temperature range of 162°C to 210°C whereby its temperature dependence can be described by Eqn. 5.1.

Table 5.1: Viscosity average relaxation times as obtained from small amplitude oscillatory shear rheometry experiments from 162°C to 210°C.

Temperature (°C)	Viscosity average relaxation time (s)
162	14.4
170	8.8
180	2.5
190	1.7
200	1.2
210	0.8

### 5.2.2.2 Isothermal crystallization

Isothermal crystallization experiments were carried out on PA12 with 2 wt% dye, by means of fast scanning chip calorimetry (FDSC, Mettler Toledo) combined with a Huber intracooler TC100 and differential scanning calorimetry (DSC, Mettler Toledo 823e/700) for a temperature range of 70°C to 170°C. To prevent oxidation of the sample nitrogen gas is supplied. For FDSC experiments, samples with a mass between 100 ng and 1  $\mu\text{g}$  are cut from a bulk sample. The applied thermal protocol consists of an initial heating run to 220°C for 1 s to condition the sample, followed by fast cooling to the desired temperature at 1000°C s<sup>-1</sup> where the sample is then kept for long enough time to allow full crystallization. To quantify the isothermal crystallization kinetics, the peak times were determined as the time of maximum heat flow in the exothermal crystallization peaks from Figure 5.2(a) and Figure 5.2(b). Due to the symmetry of these heat flow curves, the peak crystallization time corresponds to the half-time of crystallization  $t_{1/2}$ . Figure 5.2(c) provides the temperature dependence of the peak crystallization time, showing that the crystallization speed increases four orders of magnitude when reducing the temperature from 170°C to 70°C.

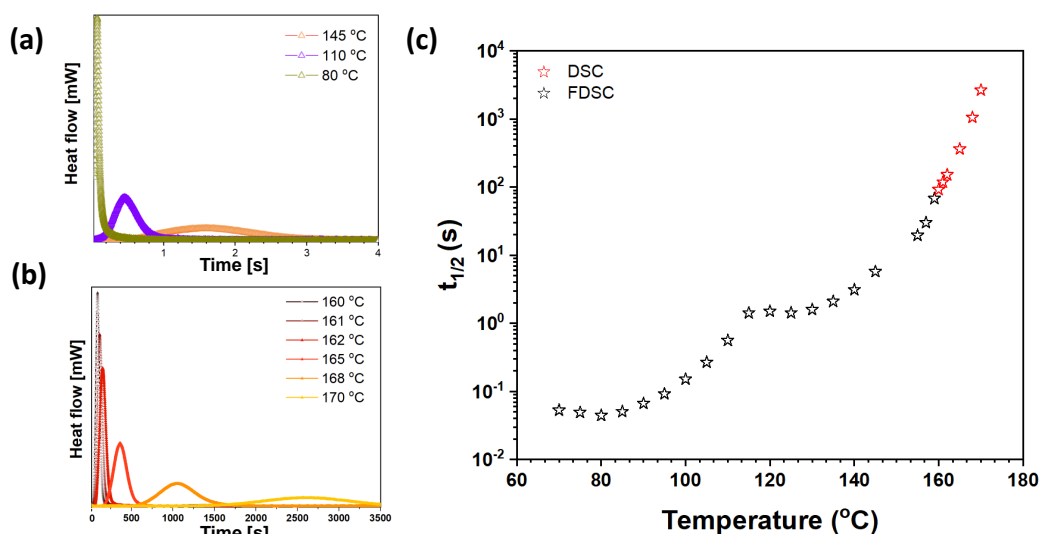


Figure 5.2: Exothermic heat flow peak during isothermal analysis at different temperatures using (a) FDSC and (b) DSC. (c) Peak time of crystallization ( $t_{1/2}$ ) as a function of crystallization temperature for PA12 with 2 wt% dye.

In Figure 5.2(c), two distinct regions can be distinguished with a transition temperature around 115°C. It has been proposed that this bimodal dependency of the crystallization rate is related to the presence of different nucleation mechanisms known as homogeneous and heterogeneous nucleation which are predominant at high and low undercooling, respectively [182, 183]. This has been shown by Rhoades et al. [182] for two grades of PA11 showing a bimodal distribution of crystallization half-time. At high temperature crystallization rates were grade dependent whereas at low temperature they were grade-independent, illustrating that crystallization at high temperatures was dominated by heterogeneous nucleation, while low temperature processes are dominated by homogeneous nucleation. Paolucci et al. found a similar trend for another grade of PA12 (PA2200, EOS) be it with an overall faster crystallization [184].

### 5.2.3 *In-situ* characterization of laser sintering

To understand the microstructure evolution at the interphase of the particle doublets, an in-house laser sintering setup [81, 82] has been utilized. This setup provides the possibility to visualize the flow dynamics and simultaneously perform time-resolved *in-situ* X-ray experiments, as shown schematically in Figure 5.3(a). Using an in-house developed micro-positioning setup [182], two similarly sized PA12 particles are placed on the substrate in a heated chamber, wherein the interface is aligned to the X-ray as well optical and laser source. X-ray with a wavelength of 0.9799 Å and beam of 100 μm x 100 μm was used. Initial conditioning was kept the same for all experiments wherein the heating chamber was heated to 155°C, which is sufficiently below the melting temperature (178°C) of the polymer, and then cooled down to the desired chamber temperature, before performing in-situ experiments. A known amount of laser energy is sent in one pulse locally at the interface of the particles and simultaneously the sintering kinetics is

captured by optical as well as X-ray scattering. Experiments were performed on PA12 particle doublets for varying particle sizes and chamber temperature, keeping the laser energy, pulse duration and radius of the laser spot fixed at 384  $\mu\text{J}$ , 1 ms and 15  $\mu\text{m}$  respectively.

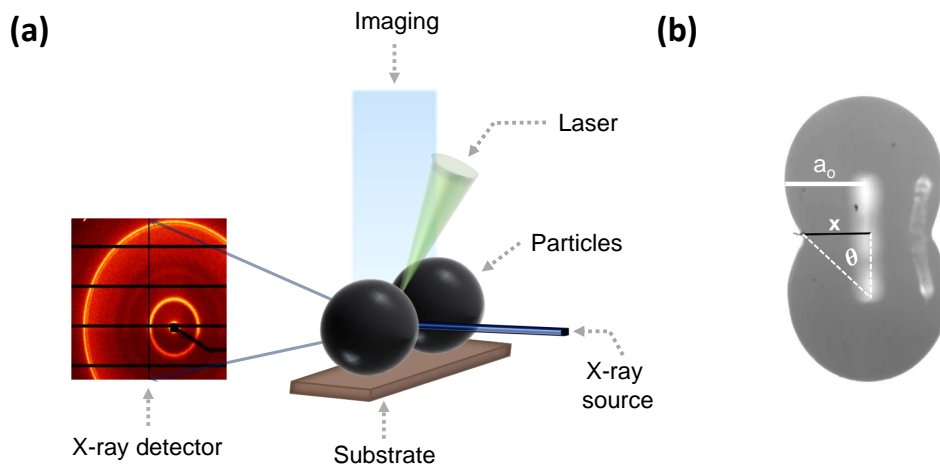


Figure 5.3: (a) Schematic representation of the experimental method. (b) Estimation of particle radii and neck (black line) at the interface between two particles.

Optical images were utilized to quantify the kinetics of the sintering process, by tracking the sintering neck formed between the particles. The image sequence was analyzed using Matlab<sup>®</sup> [82], whereby the neck radius ( $x$  in Figure 5.3(b)) growth at the interface of the particles was followed in time. The Fit2D software [110] developed by the European Synchrotron Radiation Facility was used to analyze the 2D WAXD data. The acquired images were first corrected for background noise. Then, the scattering patterns obtained from the WAXD experiments were radially integrated over an azimuthal angle of  $90^\circ\text{C}$  and the intensity was plotted versus the scattering vector  $q$ . By fitting the integrated intensity with a double Gaussian-Lorentzian function [124], the peak position and peak width can be determined. The scattered intensity profile just before the polymer starts to crystallize was fitted with an additional Gaussian-Lorentzian function to fit the amorphous background [125]. Crystallinity was calculated from the deconvolution of the total intensity in its amorphous and crystalline contributions given by:

$$\chi_c = \frac{A_c}{A_c + A_a}, \quad (5.4)$$

where,  $\chi_c$  is crystallinity,  $A_c$  is the area under the crystalline peak and  $A_a$  is the area under the amorphous halo. Infrared imaging is used to characterize the temperature profile in the particles as a function of time. For this, an Optris PI640 IR camera with lens was used from the side. This results in a pixel size of  $31 \times 31 \mu\text{m}^2$  at the used working distance. The used emissivity is 0.85 and the calibration of the camera is verified by measuring the temperature of a polymer bead on a temperature-controlled heating bed.



### 5.2.4 Characterization of morphology in sintered doublets

To study the crystal morphology created, microtomed samples of sintered PA12 doublets are prepared using a Leica RM2235 microtome, to obtain 2  $\mu\text{m}$  thin samples. Sintered doublets are embedded in epoxy resin (Sigma Aldrich), which are microtomed using a glass knife at room temperature. Sections along the long axis of the melt doublets are performed and imaged under polarized light microscope (Olympus). For atomic force microscopy (AFM) measurements, the remaining half of a doublet was further cryo-microtomed at  $-120^\circ\text{C}$  by removing several slices of around 40 nm, to achieve good flatness of the exposed surface. AFM measurements were performed using a Bruker QNA MM8 with PeakForce QNM tapping (Bruker) with a sharp tip with a diameter of 1 nm. Spherulite size and lamellar thickness were determined, by mapping out the topography as well as the stiffness at low and high resolution.

## 5.3 Results and discussion

To study the effects of particle size and processing conditions on the kinetics of the sintering process and the corresponding morphology development within the material, we study the effect of the particle size and bed temperature on the process while keeping the laser spot size, laser power and pulse duration constant. The pulse duration is fixed at 1 ms, which is an average value for the typical duration of laser impact on a fixed location in the powder bed from a scanning laser in an SLS process. Based on the energy required to completely melt one particle of PA12 with a radius of 100  $\mu\text{m}$ , which is 192  $\mu\text{J}$ , a pulse energy of 384  $\mu\text{J}$ , at a fixed laser spot with a radius of 15  $\mu\text{m}$ , is applied at the interface of the PA12 particle doublets. To investigate the effect of the particle size on the sintering dynamics, we selected doublets of equal-sized particles with radii ranging from 100  $\mu\text{m}$  to 200  $\mu\text{m}$ .

### 5.3.1 Effect of particle size

In the SLS process it is desired that the polymer particles are fully fused in the final product. Therefore the balance between sintering kinetics and time interval available for sintering plays an important role in the final part properties. To systematically study the sintering process, we probe the dynamics of the sintering process together with the temperature profile of the particles as well as the development of the internal microstructure. Figure 5.4 shows a representative set of images for particles with a radius of 125  $\mu\text{m}$ . The chamber temperature is set at  $155^\circ\text{C}$ , which is about  $23^\circ\text{C}$  below the peak melting temperature of PA12.

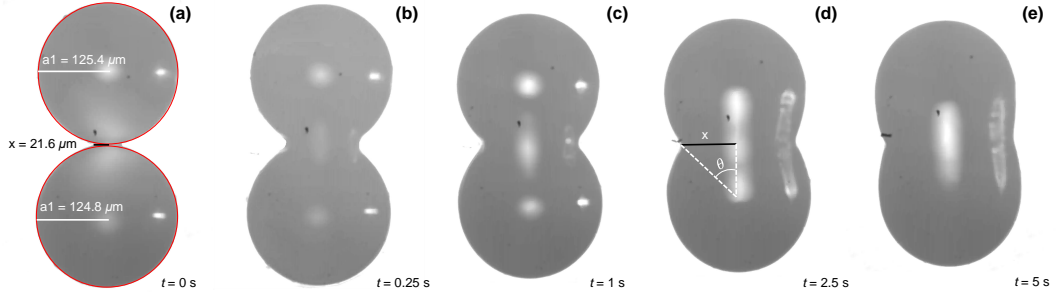


Figure 5.4: Image sequence of sintering (a to e) for PA12 particle pairs of radius  $a_o = 125 \mu\text{m}$ , wherein heating chamber temperature  $T_c = 155^\circ\text{C}$ , pulse energy  $E_p = 384 \mu\text{J}$  and pulse duration  $t_L = 1 \text{ ms}$ . The evolution of the neck (black line in Figure 5.4(c), at the interface between the two particles is followed in time.

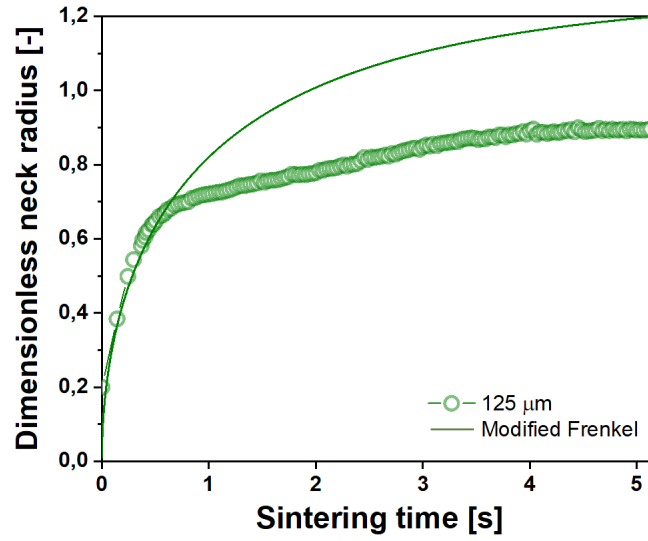


Figure 5.5: Comparison of modified-Frenkel model with sintering experimental results of PA12 for a particle radius  $a_o = 125 \mu\text{m}$ , heating chamber temperature  $T_c = 155^\circ\text{C}$ , pulse energy  $E_p = 384 \mu\text{J}$  and pulse duration  $t_L = 1 \text{ ms}$ . Viscosity value in the modified-Frenkel model corresponds to a constant temperature of  $226^\circ\text{C}$ .

From the image sequence in Figure 5.4 it can be seen that the instant the laser energy hits the interface of the polymer doublet (Figure 5.4(a)), at  $t = 0 \text{ s}$ , a neck is formed which tends to grow until sintering is completed at around  $t = 5 \text{ s}$ . The final obtained neck radius remained the same and no further flow occurred after 5 s. This sintering process is driven by the surface tension and facilitated by the local increase of the temperature at the laser-heated interface of the doublet, which increases the mobility of the polymer chains to enable viscous flow [94]. The evolution of neck radius as a function of time was determined using the image sequence in Figure 5.4 and plotted in Figure 5.5 as the dimensionless neck radius  $x/a_o$ . Subsequently, the evolution was fitted with the modified Frenkel model for viscous sintering under isothermal conditions [120]:

$$\frac{d\theta}{dt} = \frac{\Gamma}{\eta a_o K_1^2} \frac{2^{-5/3} \cos \theta \sin \theta}{[2 - \cos \theta]^{5/3} [1 + \cos \theta]^{4/3}}, \quad (5.5)$$

where  $\Gamma$  is the surface tension,  $\eta$  the viscosity,  $a_o$  the particle radius,  $\theta$  the angle between the line connecting the particle centers and that connecting a particle center with the extreme point of the neck, as indicated in Figure 5.3(b), and  $K_1$  [121]:

$$K_1 = \frac{\tan \theta}{2} - \frac{\sin \theta}{6} \left[ \frac{2(2 - \cos \theta) + (1 + \cos \theta)}{(1 + \cos \theta) + (2 - \cos \theta)} \right]. \quad (5.6)$$

From  $\theta$  the dimensionless neck radius  $x/a_o$  can be obtained, given by [120]:

$$\frac{x}{a_o} = \sin \theta \left( \frac{4}{(1 + \cos \theta)^2 (2 - \cos \theta)} \right)^{1/3}. \quad (5.7)$$

This model describes the initial sintering kinetics well, and using the viscosity  $\eta$  as a fitting parameter results in a fit value of 94 Pa·s, which corresponds to a temperature of 226°C. Obviously, the slowing down of sintering at later times due to cooling can not be described with the modified Frenkel model. Contrary to the amorphous PS studied in our previous work, it can be seen in Figures 5.4 and 5.5 that the solidification of the particle doublet and cessation of the viscous sintering does not occur immediately at the end of the laser pulse. This is probably attributed to the fact that solidification is not instantaneous but depends on the crystallization kinetics, which is studied simultaneously via X-ray characterization.

Image sequences as in Figure 5.4 were collected for a set of particle doublets with different particle radii. Figure 5.6(a) shows the dimensionless neck radius  $x/a_o$ , calculated as a function of sintering time for different particle radii. It can be observed that with increasing particle size, the sintering kinetics slows down and the final  $x/a_o$  value also substantially reduces. The final doublet morphology can be observed for varying particle sizes in Figure 5.6(b), resulting in partially sintered doublets after cessation of flow. At the later stages of sintering, surface tension is insufficient to overcome viscous loss during flow [120], thereby sintering is halted at an intermediate stage. Besides the slower sintering kinetics at the start of the process, cessation of flow also occurs slightly earlier for the larger particles. The characteristic timescale for isothermal viscous sintering from the Frenkel model, which is  $(\eta_{s,0} a_o / \Gamma)$  with  $\Gamma$  the surface tension of PA12,  $\eta_{s,0}$  the steady state zero-shear viscosity at 200°C and  $a_o$  the initial particle radius [120] is on the order of 4.6 s for a particle radius of 100  $\mu\text{m}$ . Rescaling the sintering times with this characteristic Frenkel time still reveals a slower kinetics for the larger particles, as can be seen in Figure 5.19 (Appendix I), similar to our previous work on amorphous polystyrene [81], shown in Chapter 4. By increasing the particle size, the relative volume of the region illuminated with laser energy as compared to the total particle volume decreases, whereby the unsintered sides act like a heat sink, resulting in a lower temperature at the interface of the particle doublets. Hence, the viscosity that governs the resistance to the sintering process depends on the particle size. It can thus be concluded that the final dimensionless neck radius is dependent on the evolution of the polymer viscosity as a function of time, which is mainly governed by its temperature dependence.

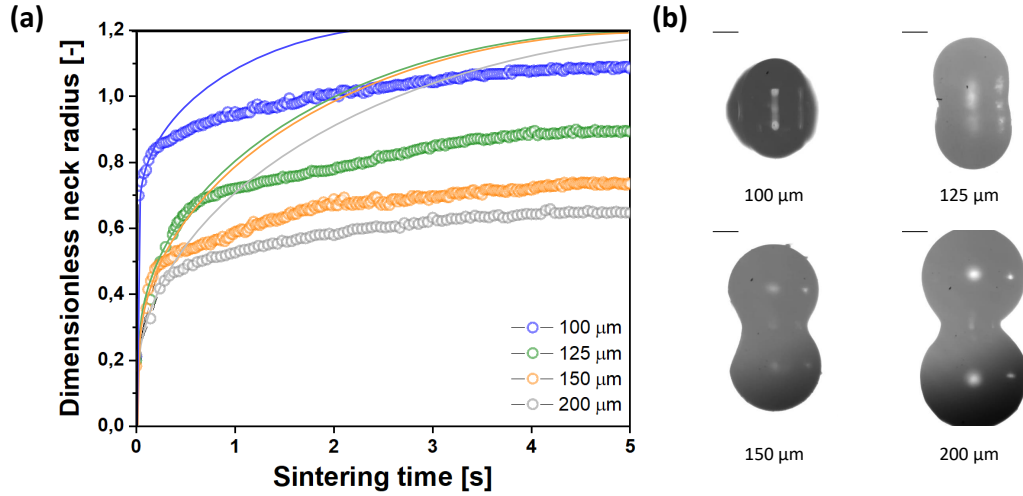


Figure 5.6: Effect of particle radius on sintering kinetics of PA12 doublet with heating chamber temperature of  $T_c = 155^\circ\text{C}$ , pulse energy of  $E_p = 384 \mu\text{J}$  and pulse duration of  $t_L = 1 \text{ ms}$ . (a) Dimensionless neck radius versus sintering time (b) particle doublets at the end of sintering process.

The sintering results clearly show that the particle size indirectly affects the sintering process through its effect on the temperature in the neck region. To investigate this further, the temperature profile during sintering was tracked with an IR camera. Figure 5.7(a) shows the thermal images obtained for particles with a size of  $125 \mu\text{m}$  at various time points during the sintering process. It can clearly be observed that the heat is dissipated from the bulk to the edges of the particle doublet. The characteristic time for heat diffusion  $t_c$  for this system:

$$t_c = \frac{2a_o^2 \rho c_p}{k}, \quad (5.8)$$

with  $a_o$  the particle radius,  $\rho$  the density,  $c_p$  the heat capacity and  $k$  the thermal conductivity, is approximately  $0.9 \text{ s}$ , which is of the same order of magnitude as the time required for the heated zone to spread out over the particle doublet in Figure 5.7(a). Based on the thermal images, the local temperature at the center of the particle doublets is determined and plotted in Figure 5.7(b) for the different particle sizes. As discussed previously, with reducing particle size, the temperature experienced locally at the interface is higher. From Figure 5.7(b) it follows that initially, at  $t = 0.01 \text{ s}$ , the temperature observed for  $100 \mu\text{m}$ ,  $125 \mu\text{m}$ ,  $150 \mu\text{m}$  and  $200 \mu\text{m}$  radius is  $230^\circ\text{C}$ ,  $210^\circ\text{C}$ ,  $198^\circ\text{C}$  and  $193^\circ\text{C}$  respectively. Fits with the modified Frenkel model of the initial sintering kinetics in Figure 5.5 provide viscosity values that correspond to a temperature of  $258^\circ\text{C}$ ,  $226^\circ\text{C}$ ,  $221^\circ\text{C}$  and  $204^\circ\text{C}$  for particle radius values ranging from  $100 \mu\text{m}$  to  $200 \mu\text{m}$ . Clearly, the isothermal model overestimates the initial sintering temperature as compared to the experimentally measured values. Based on the cooling of the particles, the opposite effect (i.e. too low temperatures from the modified Frenkel model) may be expected. However, it should be taken into account that the laser pulse duration is only  $1 \text{ ms}$  in this case and the first temperature measurement occurs after  $10 \text{ ms}$ . Therefore, the maximum measured temperatures are not the absolute maxima. The difference between the measured temperatures and the ones estimated from the modified Frenkel

model varies randomly between 11°C and 28°C thereby indicating that the model provides satisfactory estimates of the temperature but is not accurate enough to distinguish between the various particle sizes. This can partially be caused by the high sensitivity of the model to the initial data points of the sintering kinetics. In addition, the laser sintering process is a non-isothermal process and, since with different particle sizes the heat loss is different, the particles may be undergoing a different cooling rate.

To assess the cooling rate of the particles in more detail, a simple heat balance of a single particle, cooling down in quiescent air, is set up. When assuming a constant temperature of the particle, which is reasonable considering the short heat diffusion time inside the particle, and in absence of significant contributions of radiation, this leads to the following temperature profile of  $T_p$  the particle temperature:

$$T_p(t) = (T_{\max} - T_c) \cdot \exp\left(-\frac{hAt}{mc_p}\right) + T_c, \quad (5.9)$$

where  $m$  is the particle mass,  $c_p$  the heat capacity,  $h$  the heat transfer coefficient,  $A$  the particle surface area,  $T_{\max}$  the maximum temperature at the interface of the particles, and  $T_c$  the temperature of the heating chamber. This model was fitted on the temperature profiles in Figure 5.7(b). It can be seen that the model describes the temperature data relatively well, with only a slightly faster cooling than expected in the final stages for the two smallest particle sizes. The heat convection coefficient was taken as a fit parameter and varied between 175 and 300 W/m<sup>2</sup>·K, wherein  $h$  is the highest for 200 μm radii particles. Based on the consideration that buoyancy-driven flows are negligible at low values of the Rayleigh number [122], the dimensionless Nusselt number is equal to 2 [122], which results in  $h$  being proportional to  $1/a_o$  ( $Nu = h 2 a_o / k$ ) and ranging from 300 to 170 W/m<sup>2</sup> K for particle sizes between 100 μm and 200 μm. The order of magnitude of the calculated heat transfer coefficient is thus correct, but smaller particles are expected to cool faster, which is not fully confirmed by the data. However, it should be taken into account that the temperature inside the particles is not completely isothermal and that heat loss to the substrate most probably also contributes [185]. The increasing trend of the heat transfer coefficient with particle size indicates that the Nusselt number is not constant, which may indicate that convection flows are present. Overall, the measured temperature curves and extracted heat transfer coefficients provide relevant input for numerical models of the laser sintering process, which require an accurate description of the temperature evolution. In summary, it can be concluded from Figure 5.7(b) that particles reach a homogeneous temperature of 155°C after about 4.2 s for 200 μm particles and 5.3 s for 100 μm particles.

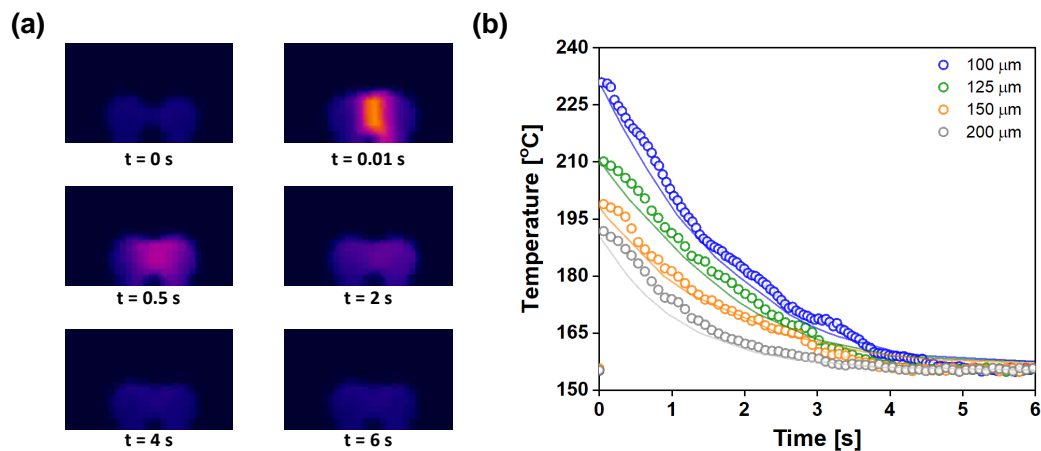


Figure 5.7: a) Image sequence of IR images for particles with radius  $a_o = 120 \mu\text{m}$ . (b) Temperature as a function of time obtained for various particle sizes for a heating chamber temperature of  $T_c = 155^\circ\text{C}$ , pulse energy of  $E_p = 384 \mu\text{J}$  and pulse duration of  $t_L = 1 \text{ ms}$ . Lines in (b) are fits with Eqn. 5.9 resulting in values for  $h$  of respectively 173, 218, 260 and  $300 \text{ W/m}^2\text{K}$  for particle sizes ranging from 100 to 200  $\mu\text{m}$ .

The results in Figure 5.6 and 5.7 clearly show that particle size has a major effect on the heating as well as cooling of the particles and hence on the kinetics of the sintering process. Apart from the viscous flow in the material, also the crystallization kinetics and thus the resulting solidification behavior, will depend on the temperature profile. Therefore, WAXD patterns of the central region of the particle doublet, around the neck region, are collected, while sintering. A representative set of images is shown as insets in Figure 5.8. No anisotropy occurs in the scattering images along the azimuthal angle, and this is the case for all experiments presented in this work. Similar images were obtained for other particle sizes (see Figure 5.18 in Appendix I). WAXD patterns were integrated over an azimuthal angle of  $90^\circ$  to plot intensity versus scattering vector  $q$ . This integrated intensity is then fitted using a double Gaussian-Lorentzian function to determine the peak positions, as shown in Figure 5.8. The first frames in Figure 5.8(a) are representative of the amorphous hallow, wherein  $t = 0 \text{ s}$  corresponds to the instant when the laser hits the polymer, until the polymer starts crystallizing at around  $t = 8 \text{ s}$ , shown by a distinct growth in peak at around  $q = 15.02 \text{ nm}^{-1}$ . Based on the peak area, the evolution of the total crystallinity with time can be determined.

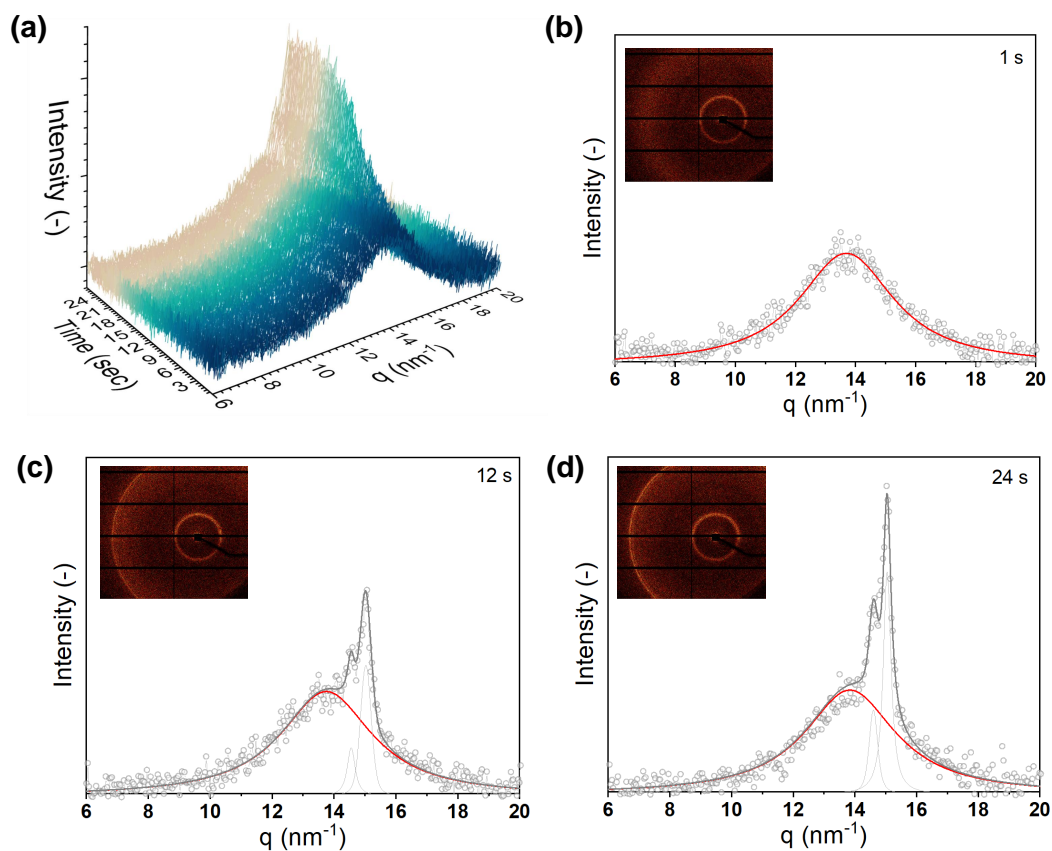


Figure 5.8: (a) 3D plot of the radially integrated intensity as a function of scattering vector  $q$  for the complete acquisition time. The plots in (b), (c) and (d) represent integrated intensity as a function of scattering vector  $q$  at 1 s, 12 s and 24 s with WAXD pattern in inset.

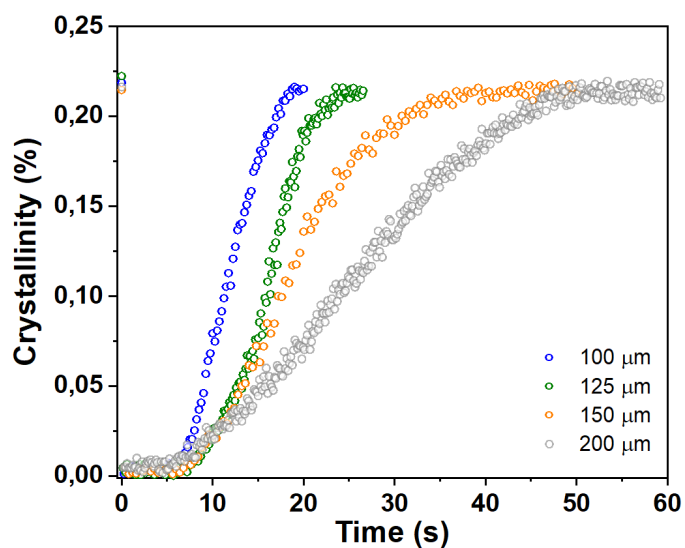


Figure 5.9: Time evolution of crystallinity during the sintering process for PA12 particles with various sizes, heating chamber temperature of  $T_c = 155^\circ\text{C}$ , pulse energy of  $E_p = 384 \mu\text{m}$  and pulse duration of  $t_L = 1 \text{ ms}$ .



Figure 5.9 shows the resulting *in-situ* time-resolved crystallization kinetics for various particles sizes. The overall crystallinity value for all the particle sizes is around 21.5 %, before and after sintering. But a pronounced difference in crystallization rate is observed, wherein with increasing particle size the crystallization rate reduces. From the time evolution it can be observed that the onset of crystallization occurs at 5 s to 7 s for particle radii between 100  $\mu\text{m}$  and 200  $\mu\text{m}$ . Comparing these time scales with the sintering kinetics in Figure 5.6 shows that crystallization starts after cessation of flow. The half time of crystallization for particle radii of 100  $\mu\text{m}$ , 125  $\mu\text{m}$ , 150  $\mu\text{m}$  and 200  $\mu\text{m}$  is about 11 s, 15.5 s, 17 s, 27 s respectively. These timescales do not correspond to the half time of crystallization estimated under isothermal conditions at 155°C (chamber temperature), which is 19.5 s. Based on the temperature profiles in Figure 5.7, the crystallization is expected to be slower than under isothermal conditions due to the larger residence time at higher temperatures. Moreover, taking into account the temperature dependence of the half time of crystallization, as shown in Figure 5.2, a slower crystallization kinetics was expected for the smaller particles, which have a higher overall temperature. However, laser sintering not only results in non-uniform and time-dependent temperature profiles, but also generates a complex flow field [186]. With varying particle size the deformation rates experienced during the initial sintering stages differ as well, as can be inferred from the sintering kinetics shown in Figure 5.6. Therefore a complex interplay between temperature and deformation kinetics can further influence the crystallization kinetics, as being observed in Figure 5.9.

The crystallization kinetics in Figure 5.9 suggests that the flow history experienced by the material during sintering has an impact on the subsequent crystallization process. It is well-known that the underlying mechanism for flow-induced crystallization processes depends on the deformation rate [187]. Different flow regimes were defined based on a critical Weissenberg number,  $Wi = \dot{\gamma}\lambda$ , where  $\dot{\gamma}$  is the deformation rate and  $\lambda$  the relaxation time. The orientation and stretch of molecules can be characterized by the reptation time,  $\lambda_{\text{rep}}$  and Rouse time  $\lambda_s$  respectively, which are correlated by [188]:

$$\lambda_s = \frac{\lambda_{\text{rep}}}{3Z}, \quad (5.10)$$

where  $Z$  is the average number of entanglements,  $Z = M_w/M_e$ . Based on these timescales two characteristic Weissenberg numbers are defined, namely  $Wi_{\text{rep}} = \dot{\gamma}\lambda_{\text{rep}}$  and  $Wi_s = \dot{\gamma}\lambda_s$ . Chains are in equilibrium if  $Wi_{\text{rep}}$  and  $Wi_s < 1$  and no effect on crystallization will be observed. Orientation of the contour path of the polymer chains occurs when  $Wi_{\text{rep}} > 1$  and  $Wi_s < 1$ , which can enhance the number density of crystal nuclei and eventually induce chain stretching when  $Wi_{\text{rep}}$  and  $Wi_s > 1$ .

The deformation rates during laser sintering can be estimated from the growth rate of the neck radius, using the generalized modified frenkel model, where a purely biaxial flow with homogeneous extension rate is assumed [121], the extension rate  $\dot{\epsilon}$  depends on the sintering kinetics, given by [120]:

$$\dot{\epsilon} = K_1 \frac{d\theta}{dt}, \quad (5.11)$$



Table 5.2: Estimated reptation and Rouse times for different temperatures estimated using Eqn. (5.1) and multimode Maxwell model fit.

Temperature ( $^{\circ}\text{C}$ )	$\lambda_{\text{rep}}$ (s)	$\lambda_{\text{s}}$ (s)
162	66.1	0.86
170	40.2	0.52
180	11.3	0.15
190	7.6	0.09
200	5.4	0.07
210	3.8	0.05

with  $K_1$  and  $\frac{d\theta}{dt}$  as defined in Eqns. (5.5) and (5.5) respectively. The sintering kinetics is fast initially and tends to slow down in time due to the reduced driving force (see Figure 5.20 in Appendix I). The maximum deformation rates estimated during the initial sintering stage from Figure 5.6(a) for 100  $\mu\text{m}$  and 200  $\mu\text{m}$  particle radii are 4.6  $\text{s}^{-1}$  and 2.8  $\text{s}^{-1}$  respectively. Using the reptation and Rouse times from Table 5.2 and the maximum deformation rate estimates, it can be concluded that the maximum  $Wi_{\text{rep}}$  is larger than 1 and  $Wi_{\text{s}}$  is smaller than 1, suggesting an enhanced number density of nuclei without polymer chain orientation. Average relaxation time from Maxwell model were utilized in estimating the  $\lambda_{\text{rep}}$ . Since the Weissenberg number dictates the flow regime, with increasing deformation rate the crystallization kinetics would be enhanced. This is in agreement with the trend observed in Figure 5.9, thereby clearly indicating that flow affects the crystallization during laser sintering. It has been observed [176, 189] that more alignment in the flow direction can enhance the nucleation density, thereby fastening the overall crystallization kinetics. Models describing the dependency of nucleation density on deformation rate have also been proposed and validated for different polymers [190, 191]. However, at present the flow-induced crystallization behaviour of PA12 has not been studied in full detail. Therefore, quantitative predictions of the trends observed in Figure 5.9 are unfortunately not possible.

### 5.3.2 Effect of chamber temperature

Apart from the material characteristics, also the processing conditions affect the crystallization process. To systematically investigate the relevance of the chamber temperature, it was varied between 70 $^{\circ}\text{C}$  and 155 $^{\circ}\text{C}$ , while keeping the particle radius constant. The maximum chamber temperature was restricted to 155 $^{\circ}\text{C}$  since a higher temperature leads to premature coalescence of the particles in absence of laser irradiation, which is ideally not desired during the SLS process. It is expected that, for a given laser energy and particle size, reducing the chamber temperature results in a lower temperature at the sintering region. This corresponds to a higher viscosity, thereby hampering the sintering process. At lower chamber temperatures the optical imaging system was not capable of capturing complete initial sintering dynamics.

For chamber temperatures of 70 $^{\circ}\text{C}$  and 110 $^{\circ}\text{C}$  solidification occurs much faster, and reaches a plateau within 3 ms respectively. This suggests that the initial sintering kinetics is faster for a lower chamber temperature. This is expected since low temperatures

leading to solidification will be reached faster. Hence, the final dimensionless neck radius decreases with decreasing chamber temperature, as shown in Figure 5.10 from the optical images as well as the neck radius values. Even though our results on amorphous PS also showed a rather limited effect of the chamber temperature on the sintering kinetics [81], faster kinetics is not expected. However, this behaviour occurs systematically, also for larger particle sizes. A possible reason could be the wetting of the doublet on the substrate, which can be more pronounced at high temperatures.

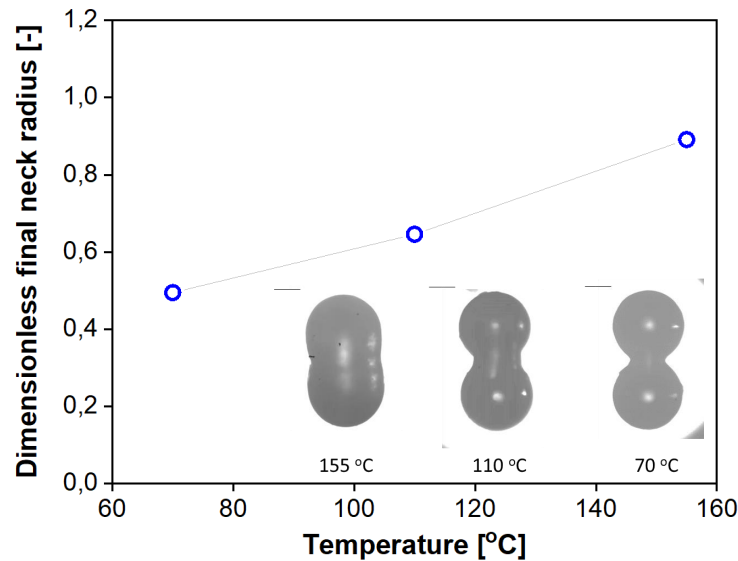


Figure 5.10: Effect of chamber temperature on sintering of PA12 particle pairs of radius  $a_o = 125 \mu\text{m}$  with pulse energy of  $E_p = 384 \mu\text{J}$  and pulse duration of  $T_L = 1 \text{ ms}$ . (a) Dimensionless neck radius versus sintering time (b) Dimensionless final neck radius versus temperatures. The inset shows the particle doublets after sintering.

The evolution of the crystallinity for conditions that correspond to those for which the neck radius growth is plotted in Figure 5.10(a), can be seen in Figure 5.11. Comparing Figure 5.10(a) and Figure 5.11 shows that similar to the situation at a chamber temperature of  $155^\circ\text{C}$ , the neck growth has a faster kinetics as compared to the crystallization. It can be observed that, even though solidification and crystallization both occur much faster with a lower chamber temperature, cessation of flow occurs before the onset of crystallization (3 ms). Hence, the interface is in the amorphous state during sintering and upon solidification crystallization starts. The half crystallization time,  $t_{1/2}$ , at chamber temperatures of  $70^\circ\text{C}$  and  $110^\circ\text{C}$ , for isothermal conditions and non-isothermal laser sintering experiments are of the same order of magnitude, about 0.2 s and 0.4 s respectively. This is different from the case at  $155^\circ\text{C}$ , for which the crystallization observed during laser sintering was faster than under isothermal conditions. At the low chamber temperatures, sintering only occurs to a very limited extent, and crystallisation is much faster. This may lead to less pronounced effects of flow-induced crystallization.

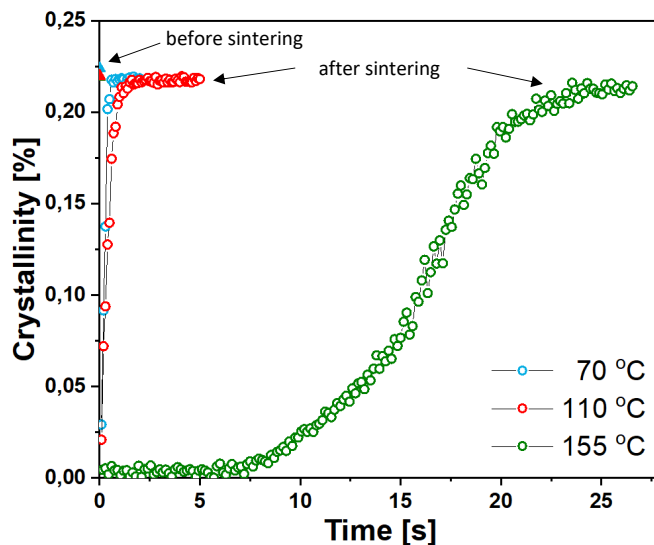


Figure 5.11: Time evolution of crystallinity during the sintering process for 125  $\mu\text{m}$  PA12 particles with heating chamber temperature of  $T_c = 155^\circ\text{C}$ , pulse energy of  $E_p = 384 \mu\text{J}$  and pulse duration of  $t_L = 1 \text{ ms}$ .

### 5.3.3 Combined effects of chamber temperature and particle size

To further study the combined effects of chamber temperature and particle size, sintering of particles with radii of 100  $\mu\text{m}$ , 125  $\mu\text{m}$ , 150  $\mu\text{m}$  and 200  $\mu\text{m}$  is studied at a reduced chamber temperature of  $110^\circ\text{C}$ . For all particle sizes the neck ceases to grow within 0.02 s. The solidification process is very fast and the time resolution of the imaging system is not sufficient to study the sintering kinetics in detail, as demonstrated in Figure 5.21 in Appendix I. Figure 5.12 shows the final dimensionless neck radius as a function of particle size for two chamber temperatures. A more or less linear decrease of the dimensionless neck radius with particle size can be observed, which is similar to the results for amorphous PS. The results suggest a slightly lower dependence on particle size for the highest chamber temperature, which may be intuitive since at higher temperatures cooling will be less. The trend is however very subtle.

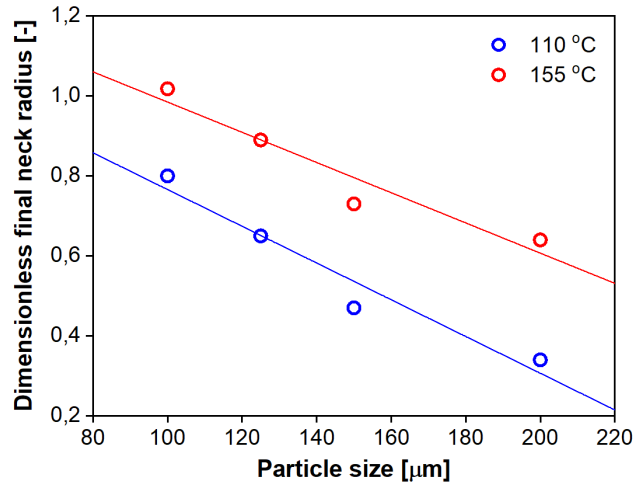


Figure 5.12: Effect of heating chamber temperature and particle radius on final dimensionless neck radius of PA12 particles for  $a_0 = 125 \mu\text{m}$ , pulse energy of  $E_p = 384 \mu\text{J}$  and pulse duration of  $t_L = 1 \text{ ms}$ .

Figure 5.13 shows the evolution of the temperature during sintering. As compared to Figure 5.7 for the higher chamber temperature, it is clear that the particle size has less effect on the temperature at lower chamber temperature. Whereas for the high chamber temperature, the diffusion of heat through the particles is faster than the cooling process, the opposite situation occurs at the low chamber temperature, the cooling occurs within 0.1 s, which does not give sufficient time for the heat to spread throughout the particles. The corresponding crystallization kinetics is shown in Figure 5.13(b). The chosen acquisition time is a compromise between capturing the crystallization kinetics and maintaining a good signal to noise ratio. Based on Figure 5.12 and Figure 5.13, it may be concluded that the effect of the particle size on the crystallization kinetics is less pronounced for the low chamber temperature. The half time of crystallization under isothermal conditions at 110°C is estimated from Figure 5.2 to be 0.57 s and from Figure 5.13(b) the half time of crystallization is between 0.3 s and 0.5 s for 100  $\mu\text{m}$  and 200  $\mu\text{m}$  particle radii whereby particles undergo complete crystallization within 1.3 s. Accurate estimates of the Weissenberg number are not possible due to the lack of high speed information about the sintering kinetics but the slightly higher temperatures observed for the smallest particles combined with a faster crystallization kinetics suggest effects of flow-induced crystallization, be it to a much smaller extent than at the high chamber temperature of 155°C. This is most probably caused by the limited flow occurring before solidification in combination with the already fast quiescent crystallization.

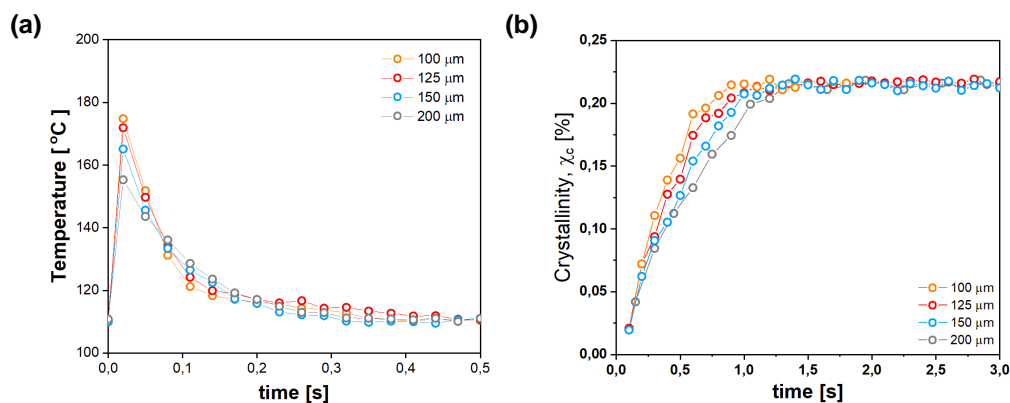


Figure 5.13: (a) Temperature evolution as a function of time from IR imaging at the interphase of a PA12 particle doublet. (b) Time evolution of crystallinity during sintering for PA12 particles. Heating chamber temperature of  $T_c = 110^\circ\text{C}$ , pulse energy of  $E_p = 384 \mu\text{J}$  and pulse duration of  $t_L = 1 \text{ ms}$ .

### 5.3.4 Effect of processing conditions on internal microstructure

Apart from providing time-resolved information about the sintering and crystallization process, the second advantage of our small-scale approach is the access to local information about the crystalline microstructure within the bridge region. Figure 5.14 shows the integrated intensity of the WAXD patterns, before and after sintering the particle doublets for chamber temperatures of  $155^\circ\text{C}$ ,  $110^\circ\text{C}$  and  $70^\circ\text{C}$ . In Figure 5.14(a) for  $155^\circ\text{C}$ , before sintering a distinct peak is observed at  $q = 15.0 \text{ nm}^{-1}$  with a shoulder at lower  $q$  values. After sintering this shoulder transforms into a secondary peak at  $q = 14.6 \text{ nm}^{-1}$ . The distinct double peaks are the characteristic of a monoclinic unit cell called the  $\alpha'$ -phase [126], having a  $d$  spacing of  $0.430 \text{ nm}$  and  $0.418 \text{ nm}$  for the small and large peak respectively. It has previously been shown that under isothermal conditions, the  $\alpha'$ -phase is the stable phase at temperatures above  $140^\circ\text{C}$ , depending on the grade of PA12 [175]. With reducing the chamber temperature to  $110^\circ\text{C}$  (Figure 5.14(b)), the shoulder disappears and the X-ray pattern develops into one sharp peak at  $q = 15.1 \text{ nm}^{-1}$ , with a small decrease in  $d$  spacing to  $0.416 \text{ nm}$ . This characteristic X-ray pattern corresponds to the  $\gamma$ -phase, with a hexagonal packing, being the most stable phase observed for PA12 [182, 183]. The two distinct reflections of the monoclinic unit cell ( $\alpha'$ -phase) result from the fact that the inter-chain and inter-sheet distance are different. For a hexagonal unit cell ( $\gamma$ -phase), the inter-chain and inter-sheet distance are the same, resulting in a single sharp peak [126]. The difference in characteristic X-ray pattern before and after sintering at  $110^\circ\text{C}$  is very subtle with the only difference being that after sintering the peak becomes sharper, while the overall crystallinity value stays around 21.5 %. At a chamber temperature of  $70^\circ\text{C}$ , the X-ray pattern already corresponds to that of the  $\gamma$ -form before sintering. This is expected since the particles were initially conditioned at  $155^\circ\text{C}$  and later slowly cooled down to  $70^\circ\text{C}$  thereby forming the stable  $\gamma$ -form [175]. After sintering a shift in the peak from  $q = 15.1 \text{ nm}^{-1}$  to  $q = 15.3 \text{ nm}^{-1}$  is observed, after the particle doublet undergoes the rapid heating and cooling process. The corresponding

$d$  spacing for the  $\gamma$ -form of 0.416 nm reduces to 0.411 nm. This shift towards higher  $q$  value and reduction in  $d$  spacing has previously been observed while cooling from the melt to room temperature [126]. Similar trends can also be observed in our laser sintering experiments, wherein the peak shifts towards higher  $q$ . Though before and after sintering the final temperature is the same namely that of the heating chamber, Figure 5.14 shows that the crystal structure can slightly reorganize during sintering at high temperature.

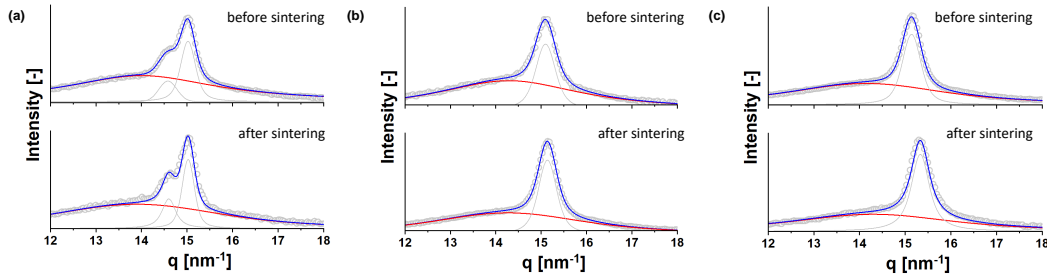


Figure 5.14: Integrated WAXD intensity and deconvolution analysis of frames before and after sintering for PA12 particle pairs of radius  $a_0 = 125 \mu\text{m}$ , wherein pulse energy  $E_p = 384 \mu\text{J}$  and pulse duration  $t_L = 1 \text{ms}$  for heating chamber temperature  $T_c$  of (a)  $155^\circ\text{C}$ , (b)  $110^\circ\text{C}$  and (c)  $70^\circ\text{C}$ .

An estimate of the mean crystal size can be made using the Scherrer equation [192]:

$$L = \frac{K\lambda}{\beta \cos(\theta)}. \quad (5.12)$$

where  $\lambda = 0.09799 \text{nm}$  is the X-ray wavelength,  $\beta$  is the peak width at full width half maximum of the diffraction peak profile in radians and  $K$  is a constant related to the crystallite shape, normally taken as 0.9 [193]. Table 5.3 shows the estimated mean crystal sizes from the WAXD intensity profiles in Figure 5.14 at varying chamber temperature for a particle radius of  $125 \mu\text{m}$ . With reducing the chamber temperature, the mean crystal size tends to reduce. This difference in mean crystal size is expected since the nucleation density in general is higher at lower temperature [194], thereby leading to more and smaller crystals. Even though the effect observed here by cooling the doublet from  $155^\circ\text{C}$  to the chamber temperature may be less pronounced than after isothermal crystallization, a clear trend is visible. In addition, the crystal size also tends to be larger after sintering as compared to before sintering. This is caused by the melting and recrystallization occurring during and after sintering, whereby the temperature protocol is different from that experienced during preparation of the particle doublets. In the latter case, the particles were quenched in water, which results in a higher cooling speed and thus smaller crystals.

Table 5.3: Mean crystal size estimated using Scherrer equation (Eqn. 5.12) before and after sintering for varying chamber temperatures.

Chamber temperature (°C)	155°C		110°C		70°C	
	Before sintering	After sintering	Before sintering	After sintering	Before sintering	After sintering
Mean crystal size (nm)	11.3	14.7	10.9	11.1	10.1	10.9

To study the crystal morphology at larger length scales than the sub-crystal scale, microtomed samples of sintered PA12 doublets are investigated via polarized light microscopy. Figure 5.15 shows images taken at the central plane of the doublets, as a function of particle size and chamber temperature. The laser illuminated zone at the interface of the particle doublets shows up as a bright zone. It can be hypothesized that the high intensity in this zone as compared to the edges of the doublet is related to a more ordered crystal structure generated during flow as compared to the unmolten zone which results from quiescent crystallization during the particle generation process. Moreover, larger objects are known to exhibit more forward scattering than small objects [195]. Hence, also the difference in crystal size can be the origin of the observed difference in brightness. It should be noted that various orientations of the set of crossed polarizers with respect to the sample were used for imaging but no orientation could be detected. The bright zone is evident for all particle sizes and chamber temperatures. Its area corresponds well to the laser heated area, as shown in Figure 5.7(a). For smaller particles, the bright zone extends over a larger part of the particle doublet, as the same amount of energy is then provided to a smaller volume of material. Similarly, the area of the bright zone reduces with reducing chamber temperature. This clearly shows that sufficient heating to cause melting and then recrystallization into a different crystal structure is at the origin of the difference in brightness.

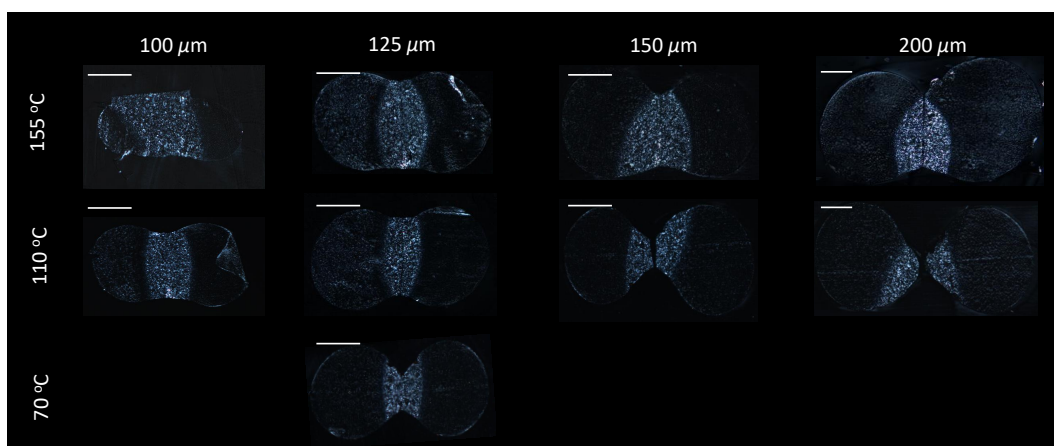


Figure 5.15: Microtomed 2  $\mu\text{m}$  thickness sample of PA12 particle doublets after sintering at heating chamber temperature  $T_c$  of 155°C, 110°C and 70°C, imaged with polarized optical microscopy. Pulse energy of  $E_p = 384 \mu\text{J}$  and pulse duration of  $t_L = 1 \text{ ms}$  with particle sizes of 100  $\mu\text{m}$ , 125  $\mu\text{m}$ , 150  $\mu\text{m}$  and 200  $\mu\text{m}$ .



Figure 5.16 shows an image sequence of sections made along the depth for 125  $\mu\text{m}$  and 200  $\mu\text{m}$  melt doublets. No clear difference is observed, except that the bright zone is visible along the thickness suggesting laser energy penetrated completely along the particle.

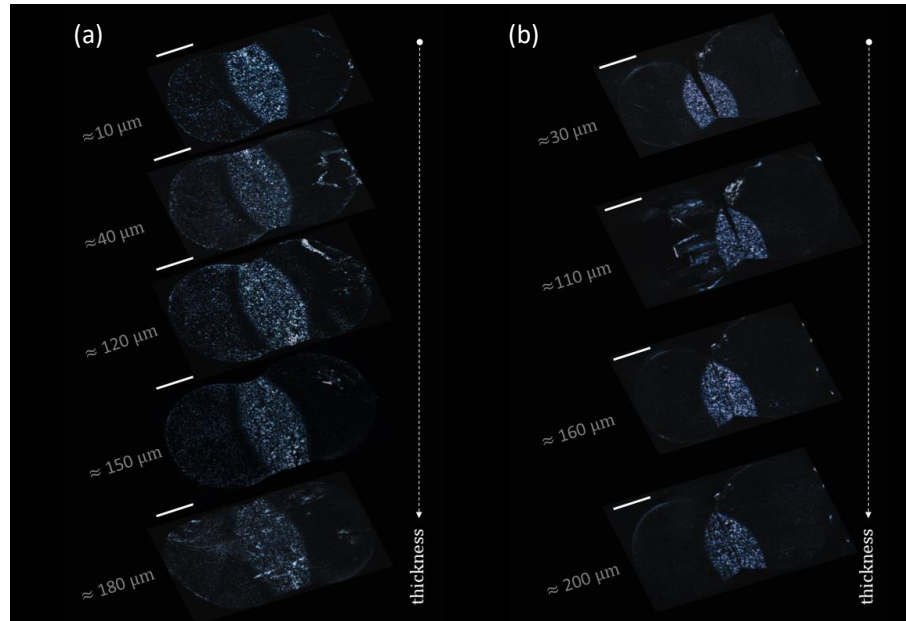


Figure 5.16: Microtomed 2  $\mu\text{m}$  thin samples of PA12 particle doublets with radius  $a_0$  of (a) 125  $\mu\text{m}$  and (b) 200  $\mu\text{m}$  imaged with polarized optical microscopy, after sintering with a heating chamber temperature of  $T_c = 155^\circ\text{C}$ , pulse energy of  $E_p = 384 \mu\text{J}$  and pulse duration of  $t_L = 1 \text{ ms}$ .

Atomic force microscopy (AFM) was performed on a microtomed doublet from 125  $\mu\text{m}$  particles. Figure 5.17 shows the topology and stiffness images performed inside and outside the laser sintered zone. The low resolution height map allows to compare the spherulite size after melt recrystallization in the laser sintered zone (Figure 5.17(a) right), to that in the unsintered zone (Figure 5.17(a) left). It can clearly be observed that the spherulite size is increased due to the sintering process, as it varied between 8  $\mu\text{m}$  and 13  $\mu\text{m}$  in the unsintered zone and between 14  $\mu\text{m}$  and 18  $\mu\text{m}$  in the laser sintered region. This is in line with the estimated mean crystal size from the Scherrer equation listed in Table 5.3, where a slightly less pronounced increase in crystallite size was observed after sintering. However, it should be noted that the size of the X-ray beam was slightly larger than the sintered region, thereby picking up differences less clear than the local AFM characterization. For the same locations, high resolution imaging is done to determine the lamellar thickness. Figure 5.17(b-c) show the topography and stiffness maps. It should be noted that the linear features that occur in both images, are mostly likely caused by defects from the microtoming. Hence, the white high stiffness lines in between the cutting defects are the crystal lamellae. On average, the observations suggest that the lamellar thickness is higher after laser sintering (Figure 5.17(c) left) as compared to before sintering (Figure 5.17(c) right).



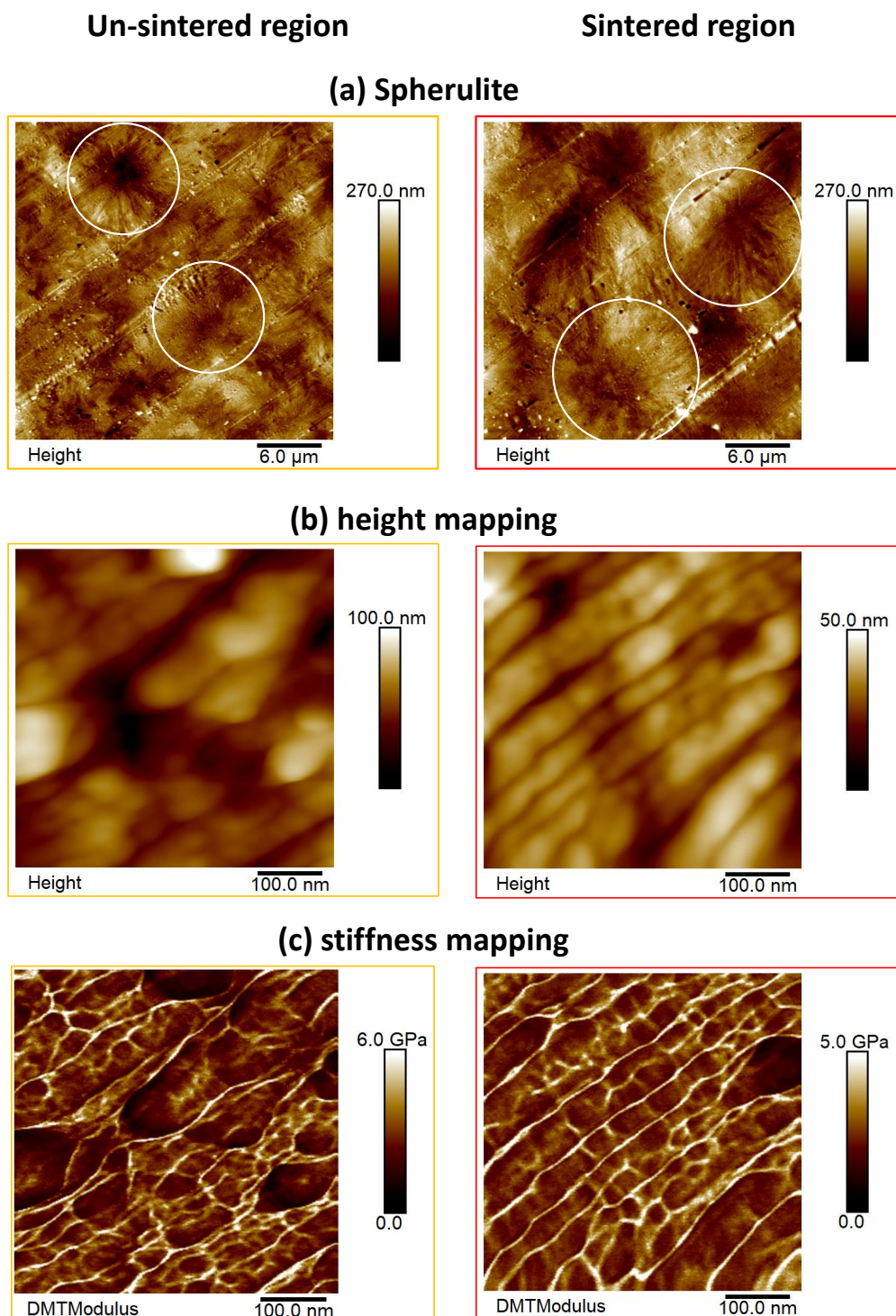


Figure 5.17: AFM images in unsintered region (left) and inside laser sintered zone (right), showing (a) low resolution height mapping with spherulites indicated by white circles, (b) high resolution height mapping and (c) high resolution stiffness mapping. Sintering of 125  $\mu\text{m}$  PA12 particle doublets at heating chamber temperature of  $T_c = 155^\circ\text{C}$ , pulse energy of  $E_p = 384 \mu\text{J}$  and pulse duration of  $t_L = 1 \text{ ms}$ .

## 5.4 Conclusions

We studied the laser sintering of PA12 particle doublets using a novel in-house developed experimental setup, which mimics the main features of an SLS machine with the capability to perform in-situ X-ray experiments. These results feature information on morphological changes during sintering process, which can only be studied by in-situ measurements. Thermal, rheological and laser light absorption properties for PA12 polymer with 2 wt% dye allowed us to determine appropriate parameter range for laser energy and chamber temperature. By simultaneous capture of flow by optical imaging and crystallization kinetics from WAXD pattern, in combination with IR imaging, a complex interplay between temperature, flow and crystallization kinetics is shown. Under the same processing condition, from flow kinetics as well as temperature evolution it was suggestive that smaller particles tend to cool down slower than bigger particles, since the local temperature experienced at the interphase of the doublet was higher. An opposite trend was observed for crystallization, where the kinetics were faster for smaller particles. Estimate of critical Weissenberg number with respect to Rouse and reptation times suggests that under given process condition, the chains could remain oriented but not stretched, which could enhance the number density of nuclei. Since deformation rates estimates for smaller particles are faster, this could explain the faster kinetics observed. In future a combination of experimental and numerical simulations will help to extend this work to an actual sintering process. Furthermore, simulations have to take into account the possibility of flow induced crystallization process during laser sintering process. Finally, several other process parameter like pulse duration and laser energy can influence the sintering as well as crystallization kinetics. In this work a systematic approach was taken to get fundamental understanding on structure development of PA12 polymer particles during sintering process.

## Acknowledgements

This work forms part of the research programme of the Brightlands Materials Center (BMC). We acknowledge the European Synchrotron Radiation Facility (ESRF) for provision of synchrotron radiation facilities and NWO for financing beam time at ESRF. We thank Dr. Daniel Hermida Merino for assistance in using the Dutch-Belgian beamline (DUBBLE) BM26 and Prof.Dr.ir. Leon E. Govaert for providing the PA12 polymer. We thank Dr.ir. Tom A.D. Engels for the discussions and Dr. Mingwen Tian from DSM for performing the AFM imaging.

## Appendix

Table 5.4: The relaxation time distribution for PA12 with 2wt% dye at 200°C.

Viscosity average relaxation time (s)
0.001
0.021
0.29
0.954
5.37

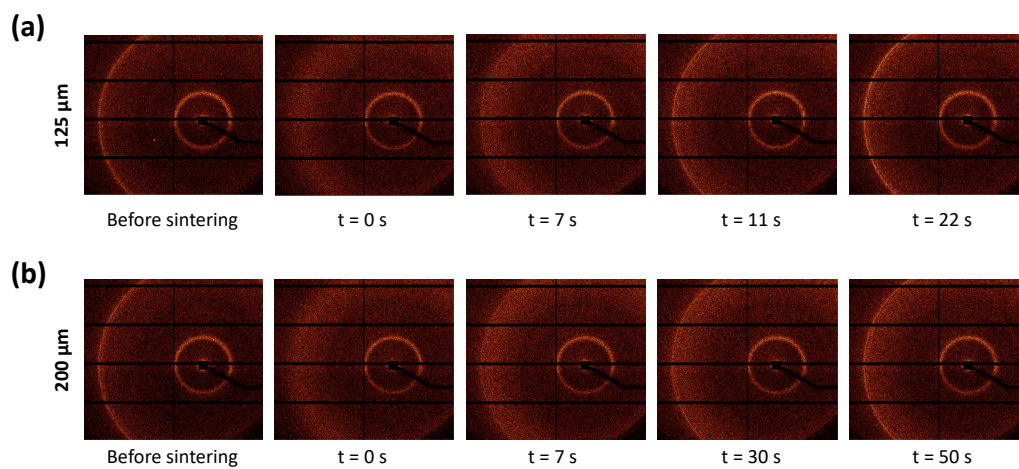


Figure 5.18: Image sequence of time-resolved 2D-WAXD patterns of PA12 particles, before and during sintering for heating chamber temperature  $T_c = 155^\circ\text{C}$ , pulse energy  $E_p = 384 \mu\text{m}$  and pulse duration  $t_L = 1 \text{ ms}$  for particle radius (a)  $125 \mu\text{m}$  and (b)  $200 \mu\text{m}$ .

The sintering kinetics for various particle sizes, whereby where by the sintering time is scaled with the characteristic Frenkel time  $\eta a_o/\Gamma$ , where  $\Gamma$ , the surface tension of PA12,  $\eta$  the viscosity and  $x/a_o$  the particle radius whereby  $\eta$  was kept the same as that obtained for a particle radius of  $125 \mu\text{m}$ .

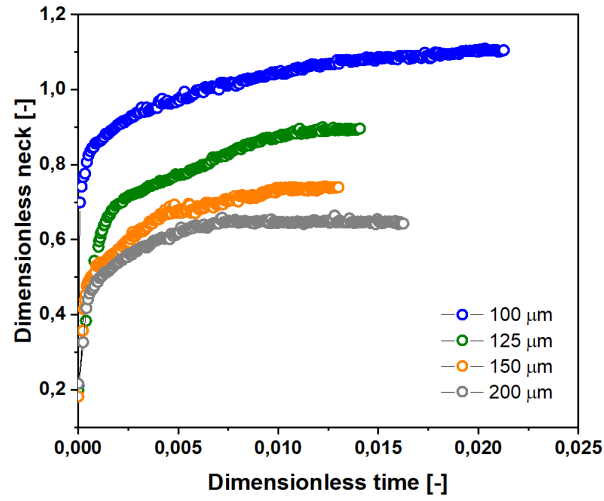


Figure 5.19: Effect of particle radius on sintering kinetics with heating chamber temperature of  $T_c$  155°C, pulse energy of  $E_p = 384 \mu\text{J}$  and pulse duration of  $t_L = 1 \text{ ms}$ . Dimensionless neck radius in side view versus time rescaled with Frenkel timescale.

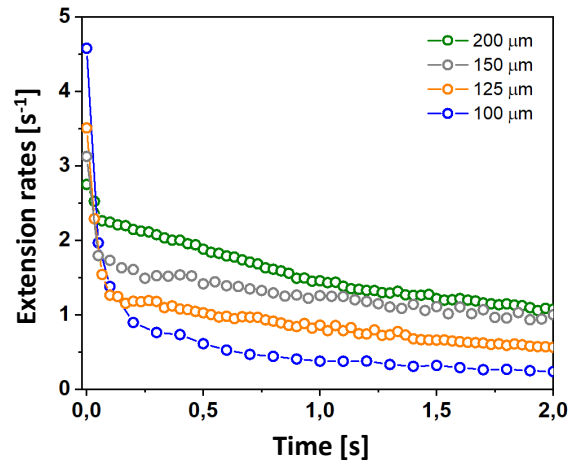


Figure 5.20: Evolution of extension rate in time for various PA12 particle sizes for heating chamber temperature of  $T_c$  155°C, pulse energy of  $E_p = 384 \mu\text{J}$  and pulse duration of  $t_L = 1 \text{ ms}$ .

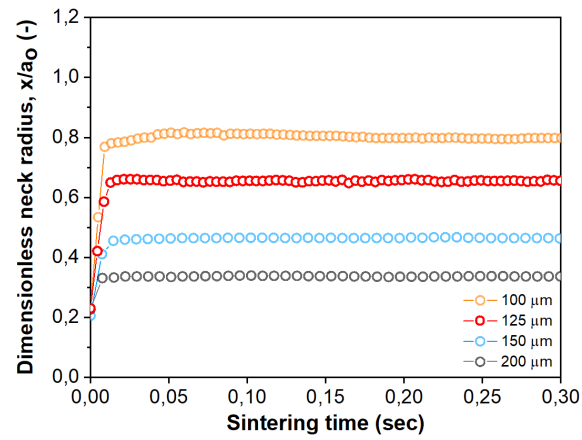


Figure 5.21: Dimensionless neck radius versus sintering time for PA12 particles on sintering kinetics with heating chamber temperature of  $T_c$  110°C, pulse energy of  $E_p = 384 \mu\text{J}$  and pulse duration of  $t_L = 1 \text{ ms}$ .

## Laser sintering of polyamide 12/carbon nanotube composite particle pairs

### Abstract

The rheological behavior of polymers is vital when producing dense parts by selective laser sintering (SLS). At the same time, the polymer rheology is very sensitive to the addition of rigid anisotropic fillers. To determine the potential influence during laser sintering, nanocomposites of carbon nanotubes (CNTs) dispersed in polyamide 12 (PA12) are characterized and then sintered, thereby starting from a spherical powder morphology to focus on the intrinsic material properties. First, we describe the effects of the addition of CNTs to PA12 on its rheological, crystallization and electrical properties. Subsequently, laser sintering of PA12/CNT particle pairs is visualized by optical microscopy and X-ray scattering. Compared to PA12, the presence of CNTs increases the viscosity and elastic moduli, including the presence of a yield stress at 2 wt% CNTs, which is shown to hinder the flow dynamics at the interface of the polymer doublets during laser sintering. For the crystallization process, the CNTs act as nucleating agents, thereby accelerating the crystallization kinetics as compared to that of PA12, both in isothermal conditions as well as during the non-isothermal laser sintering process. The electrical conductivity increased with increasing CNT content, both before and after sintering but laser sintering caused a slight loss of reduction in electrical conductivity.

### 6.1 Introduction

For applications such as electromagnetic interference (EMI) shielding, where alternatively metal based EMI shields are used, conductive nanocomposites are looked at as alternates due to their excellent corrosion resistance and light weight [196, 197, 198].

---

*Largely reproduced from:*

1) Hejmady, P., van Breemen, L. C. A., Anderson, P. D., & Cardinaels, R. Laser sintering of polyamide 12/carbon nanotube composite particle pairs. *to be submitted*.

Another application area of these nanocomposites is as antistatic materials promoting electrostatic discharge, especially in aerospace industry [199]. Polymers in general are insulators, but with addition of conductive particles, an increase in electrical conductivity is attained thereby allowing a transition from an insulator to a conducting nanocomposite at increasing filler concentrations. A minimum concentration of CNTs is required to significantly increase the conductivity [200] since inter-particle tunneling of electrons requires small inter-particle distances [201]. To achieve a high electrical conductivity in polymer nanocomposites, it is required that a 3D interconnected network of conducting fillers is formed within the polymer matrix [202]. Factors such as aspect ratio of the filler [203], orientation and dispersion within the polymer matrix [204, 205, 206, 207, 208, 209] as well as type of carbon nanofillers [206, 207, 208] play a significant role in achieving such percolation behavior, thereby defining the final properties. Carbon nanotubes (CNTs) are a unique conductive filler type with a high mechanical strength (1 GPa) and electrical conductivity of 100 S/cm [210]. Based on the development of efficient production methodologies, the production cost of CNTs has significantly dropped in the past decades, thereby enabling its usage for everyday applications and mass production [211].

Selective Laser Sintering (SLS) is an additive manufacturing technique (AM) which offers the flexibility to manufacture customized end products and has received much attention in research as well as industries in recent years [158, 165, 212, 213, 214]. The possibility to manufacture complex geometries by SLS, without a mould, paves the way to produce lightweight custom designed products from conducting polymer nanocomposites in application areas such as sensors, microelectronics and automotive sectors. SLS builds objects by sintering and fusing powder materials in a layer by layer fashion via a laser directed heat source until the target object is completely formed [11, 23, 215, 216]. Typical thermoplastic polymers being used in SLS processes are polyamide 11 (PA 11), polyamide 12 (PA 12) and thermoplastic elastomers [217], with PA12 being the most commonly used polymer in SLS, due to its narrow melting peak, wide sintering window and good processability. However, it limits the mechanical properties and functionalities [11, 23, 151, 218].

To widen the scope of the SLS process, alternative thermoplastics like PBT, iPP as well as polymer composites have been explored to enhance and diversify the properties of SLS printed parts [219, 220, 221]. Addition of filler particles has been explored as a method of producing parts with enhanced mechanical and electrical properties [222, 223]. Incorporation of such filler particles could enhance the mechanical strength, which has been attributed to the effective load transfer between the matrix and the nanotubes [224, 225]. Incorporating nanosilica particles in PA12 can enhance the mechanical properties significantly [226], whereas dispersion in PA11 showed a nonlinear behavior in properties [227]. A similar increase in mechanical properties was observed for CNTs dispersed in a PA12 polymer matrix [228]. To preserve the size and shape of PA12 powders for laser sintering, CNTs were coated on the particle surface [229]. Espera et al. [230] coated PA12 particles with carbon black and increased the concentrations up to 10wt%. However for concentrations above 3 wt% a significant drop in mechanical properties was observed due to poor adhesion of the carbon black. These previous studies show that interactions between the filler particles and the polymer matrix can significantly affect the mechanical



behavior of printed parts. Electrical properties such as dielectric constant and dissipation factor of nanocomposites processed by SLS have been studied as well [231].

Processing such nanocomposite powders by SLS provides challenges of its own. It has been observed that laser sintering is a complex thermal and flow process [114, 229, 232]. Factors such as powder composition, laser beam settings, temperature of the powder bed, and powder layer thickness can affect the outcome of the produced material. Polyamide 6 nano-clay reinforced composite materials were shown to increase the viscosity of the polymer, thereby hindering the flow behavior during laser sintering [233]. A similar problem was encountered for PA12 filled with CNTs [228]. Moreover, there have been reports of porosity in other carbon fiber reinforced polymers manufactured by SLS. For instance, Van Hooreweder et al. reported significant presence of porosity in carbon fiber reinforced PA12 parts manufactured by SLS [234]. Comparing SLS processed parts to injection moulded ones showed weaker mechanical properties. Porosity was detected by examining the cross sections of the part, postulating that voids present reduced the overall mechanical properties. Other studies on parts manufactured by SLS have indicated that porosity plays a significant role in reducing the final properties [235, 236].

Determination of the processing parameters for a newly developed polymeric material to achieve the desired properties poses a significant challenge. The main focus of this study is to understand the effects of CNTs in a PA12 polymer matrix on its flow behaviour, crystallization kinetics and electrical properties during and after laser sintering. A fundamental understanding of the effects of carbon nanotubes on the laser sintering behavior will be studied by a unique in-house developed laser sintering setup [81, 82] with the capability to perform *in-situ* visualization studies by optical microscopy and X-ray scattering.

## 6.2 Experimental procedure

### 6.2.1 Material

Polyamide 12 in pellet form (Vestamide L-1700 free from additives) was obtained from Evonik. Industrial grade multi-walled carbon nanotubes (CNT, NC7000) were procured from Nanocyl S.A. (Belgium). The nanocomposites were produced via solution mixing in benzylalcohol at 120°C by magnetic stirring followed by ultrasonication at room temperature. Two different concentrations of CNTs namely 0.5 wt% (referred to as PA12 CNT0.5) and 2.0 wt% (referred to as PA12 CNT2.0) were prepared. To the sample with 0.5 wt% CNTs Nubian black dye (PC-0870, Orient Chemical Industries co. Ltd) was added in a concentration of 1.5 wt%, whereas 2 wt% of this black dye was added to the pure PA12. This resulted in an absorption of visible light at 532 nm of 91% for PA12, 92% for PA12 CNT0.5 and 93% for PA12 CNT2, for a sample thickness of 100  $\mu\text{m}$ .



## 6.2.2 Methods

### 6.2.2.1 Calorimetry

The thermal properties of the nanocomposite materials were determined to study the effect of CNTs on the crystallization behavior. Isothermal crystallization experiments were carried out in the temperature range of 155°C to 170°C, by means of differential scanning calorimetry (DSC) (Mettler Toledo 823e/700) and Flash DSC (FDSC, Mettler Toledo). DSC measurements were performed at high temperatures, close to the peak melting temperature ( $T_m$ ) of PA12. After first heating from -25°C to 220°C, the material is cooled down to the desired temperature at 10°C/min and kept for enough time until the material fully crystallizes. The DSC was calibrated for the heat flux and melting enthalpy with indium. For FDSC experiments, before isothermal crystallization the samples were heated to 230°C, kept there for 2 seconds for conditioning and subsequently cooled down to the desired temperature at 1000°C/s. The half times of crystallization were determined as the time at maximum heat flow in the exothermal crystallization peak.

### 6.2.2.2 Rheology

To map out the flow behavior of the PA12 nanocomposites with increasing concentrations of CNTs, rheological measurements were performed. Measurements were carried out on a strain-controlled rheometer (TA instruments RDAIII) equipped with a convection oven using a plate–plate geometry of 25 mm diameter. First, time sweep experiments at 0.1 Hz and 1% strain were performed to assess the time dependency of the storage modulus ( $G'$ ). Then, the linear viscoelastic properties of the nanocomposites were determined by frequency sweep experiments for 1% strain performed at 180°C, 200°C and 220°C. Finally, strain sweep experiments were performed at a frequency of 0.1 rad/s.

### 6.2.2.3 *In-situ* visualization studies

An in-house developed experimental setup [81] was utilized for selective laser sintering. This one of a kind setup mimics selective laser sintering but also allows to visualize the process by *in-situ* optical imaging and simultaneous X-ray scattering [82]. In this setup, a visible light laser (wavelength of 532 nm) combined with an acousto-optic modulator and focussing lens allows to send laser light pulses with a well-defined pulse time, pulse energy, and spot size onto a particle doublet. The particle doublet is placed in a heated chamber, which contains three windows namely a top quartz window for the laser illumination and optical visualization and two kapton windows on the side that allow the incoming and scattered X-rays to pass without introducing any diffraction or scattering responses. A schematic and more detailed information about the experimental setup can be found in our previous work [82]. The optical images are analyzed to determine the neck growth at the interface of the particle doublets using Matlab<sup>®</sup> [81]. Simultaneously, time resolved WAXD patterns are integrated over an azimuthal angle of 90° giving intensity versus scattering vector  $q$ . After background correction, the amorphous hallow as

well as the crystalline diffraction peaks are fitted with double Gaussian-Lorentzian functions. This provides the peak width and height and the crystallinity can be calculated as the ratio of the area under the crystalline peaks and the total area under the intensity curve. Systematic *in-situ* laser sintering experiments were performed for fixed sintering conditions namely a laser spot size of 15  $\mu\text{m}$  radius, pulse duration of 1 ms, pulse energy of 384  $\mu\text{J}$  and chamber temperature of 155°C. These conditions were determined in our previous work (Chapter 5) on sintering of pure PA12 with the same setup [82]. The effects of particle size (ranging between 100 and 150  $\mu\text{m}$ ) and CNT content (0, 0.5 and 2 wt%) on the development of the crystalline microstructure in the particle doublet as well as the kinetics of the neck growth between both particles are systematically studied.

#### 6.2.2.4 Electrical conductivity

DC electrical conductivity measurements were carried out on compression molded films, spherical particles and sintered doublets. Two different measurement probes namely the linear four point probe and the two point probe were employed to compare between the bulk sample and laser sintered doublets. Conductivity measurements were performed for PA12, PA12 CNT0.5 and PA12 CNT2 compression moulded at 210°C (Fontijne Presses, Barendrecht) into rectangular films of 15 mm x 15 mm with a thickness of 0.3 mm by a four point probe (Jandel Engineering), as schematically shown in Figure 6.1(a). The measurement was performed at five different locations in random orientation for each sample, since the resistivity measured is sensitive to the sensing direction [237]. A two probe method was developed to measure the resistance of laser sintered doublets as shown in Figure 6.1(b). Two probes with 100  $\mu\text{m}$  tip radius covered with a silver coating, were connected to x-y-z translation stages to bring them in contact with the particles and melt doublets. Top and side view optical images were utilized to carefully place the probes in contact with the particle surface, ensuring accurate positioning along the center line of the doublet. Once the probes were attached, it was ensured that the particles were suspended in air, and not in contact with the substrate.

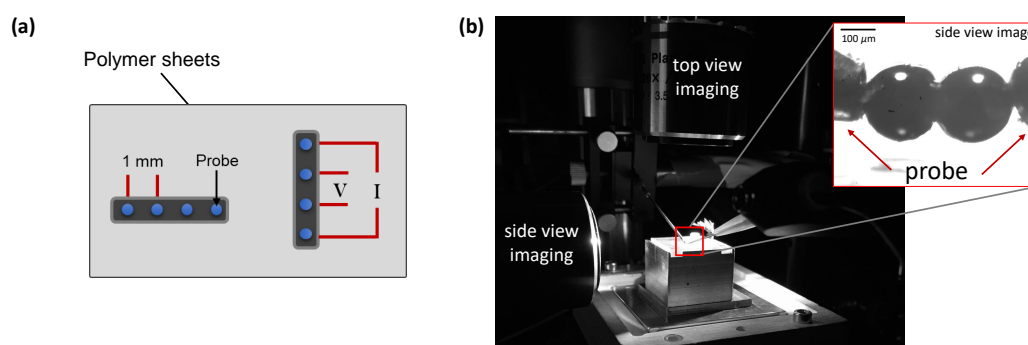


Figure 6.1: Schematic representation of conductivity measurement techniques of polymer sheets (a) linear four point probe method for polymer sheets and (b) two probe method for polymer particles and doublets. Inset shows laser sintered polymer doublet in contact with silver-covered electrode with no contact with the substrate.

In a four point probe method, a constant current ( $I$ ) is passed through the outer probes, whereas the output voltage ( $V$ ) is measured across the inner probes by a sourcemeter

(Keithley 2450, Keithley Instruments) [238]. Using ohms law,  $V = IR$ , the resistance of the material can be determined. By taking the thickness of the sample into account, the volume resistivity can be calculated from the measured sheet resistance as [239]:

$$\rho = R_s t = 2\pi \frac{V}{I} c_f t, \quad (6.1)$$

here  $\rho$  is the resistivity,  $R_s$  is the sheet resistance,  $V/I$  is the measured resistance,  $t$  is the sample thickness and  $c_f$  is a geometric correction factor for four point probe measurements. In this case,  $c_f = 1$  since the sample thickness is smaller than the distance between subsequent probes, which is 1 mm [239]. In a two probe method the current and voltage are sent and measured across the same set of probes. The disadvantage of this method is that the contact resistance at the sample-probe contacts is included in the measurement. Conductive silver paste was used to minimize the effect of contact resistance. In the setup in Figure 6.1, directly the volumetric resistance is measured, whereby volume resistivity can be calculated as [202]:

$$\rho = R \frac{A}{L}, \quad (6.2)$$

where  $\rho$  is the resistivity,  $R$  the measured resistance,  $A$  the effective cross-sectional area and  $L$  the distance between the measuring electrodes. Since the cross-sectional area is not constant for a spherical particle or doublet, it is defined here to be the largest cross-sectional area, which is  $\pi a_0^2$ . The length  $L$  is the diameter in case of a single particle and the edge-to-edge length in case of a sintered doublet. The electrical conductivity is then simply the inverse of the resistivity calculated from Eqn. (6.2). Conductivity values were measured for single particles of 150  $\mu\text{m}$  radius and laser sintered doublets of radius 100  $\mu\text{m}$  and 150  $\mu\text{m}$  for PA12 CNT0.5 and PA12 CNT2. Values were averaged over 5 measurement runs for each sample and the standard deviations were found to be within 5%.

## 6.3 Results and discussion

### 6.3.1 Thermal properties and crystallization

The onset of crystallization ( $T_c$ ), peak melting temperature ( $T_m$ ) and melting enthalpy ( $\Delta H$ ), from the second heating runs by DSC, are summarized in Table 6.1. A slightly reduced  $T_m$  and earlier onset of crystallization at a higher  $T_c$  can be observed with increasing CNTs content, but no significant change in melting enthalpy can be seen. This is consistent with other results reported for PA12 with single-walled carbon nanotubes (SWCNT) [240], PA12 with MWCNT [241, 242] and PP with SWCNT [243]. With increasing wt% of CNTs the number of nucleation points increases thereby leading to an earlier onset of  $T_c$ , which is in line with our observations.

Table 6.1: Melting enthalpy and peak melting temperature estimated from DSC experiments at  $10^\circ\text{C}/\text{min}$  heating rate for PA12, PA12 CNT0.5 and PA12 CNT2.

	PA12	PA12 CNT0.5	PA12 CNT2
$T_c$ ( $^\circ\text{C}$ )	$154.4 \pm 0.6$	$157.1 \pm 0.5$	$161.7 \pm 0.5$
$T_m$ ( $^\circ\text{C}$ )	$178.1 \pm 0.4$	$177.1 \pm 0.5$	$176.8 \pm 0.5$
$\Delta H$ (J/g)	$45.6 \pm 1.1$	$47.1 \pm 0.9$	$46.5 \pm 1.3$

To quantify the isothermal crystallization kinetics, the half time of crystallization, ( $t_{1/2}$ ), was determined as the time of maximum heat flow in the exothermal crystallization peaks from Figure 6.2(a) for PA12 CNT0.5 and Figure 6.2(b) for PA12 CNT2. Figure 6.2(c) provides the temperature dependence of the half time of crystallization comparing PA12 and PA12 nanocomposites. A common trend that can be observed for all the materials is that the further the temperature is from  $T_m$ , the shorter is the half time for crystallization. This shows the temperature dependency of the crystallization kinetics. Moreover, a distinct effect of increasing CNT content on the half time of crystallization ( $t_{1/2}$ ) can be noticed. The crystallization rates with CNTs are much faster as compared to that of PA12. This confirms that when particles, like CNTs, are added to semi-crystalline polymers, they act as heterogeneous nucleation points thereby accelerating the crystallization process, which is temperature dependent. This can clearly be observed in Figure 6.2(c), with increasing CNTs content, the half time of crystallization reduces by an order of magnitude when comparing PA12 and PA12 CNT2, at a given temperature.

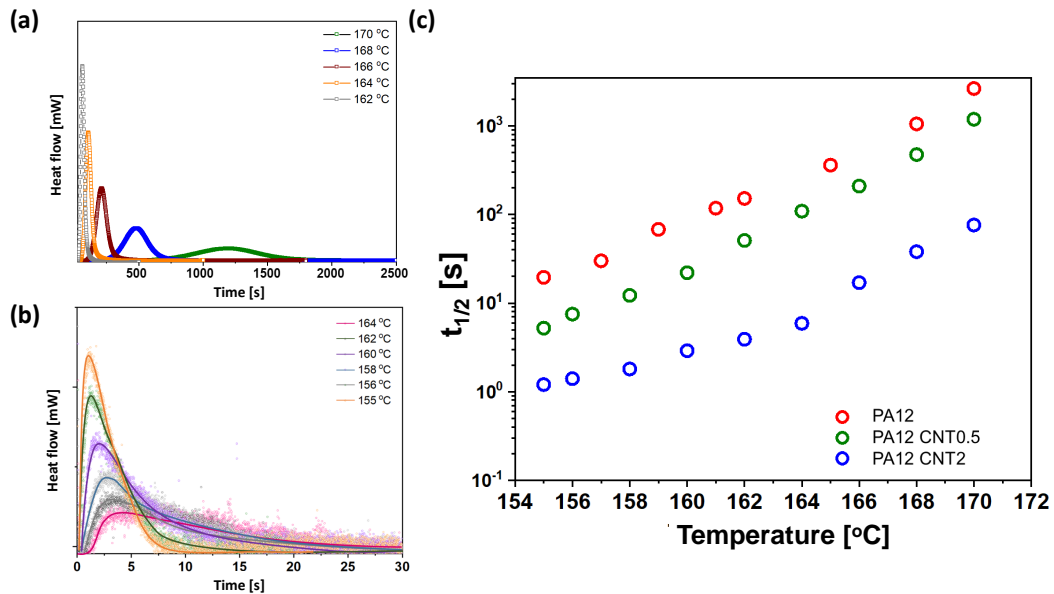


Figure 6.2: Half time of crystallization ( $t_{1/2}$ ) as a function of time at varying temperature for (a) PA12 CNT0.5, (b) PA12 CNT2 and (c) Comparison of half time of crystallization ( $t_{1/2}$ ) as a function of crystallization temperature.

### 6.3.2 Flow properties

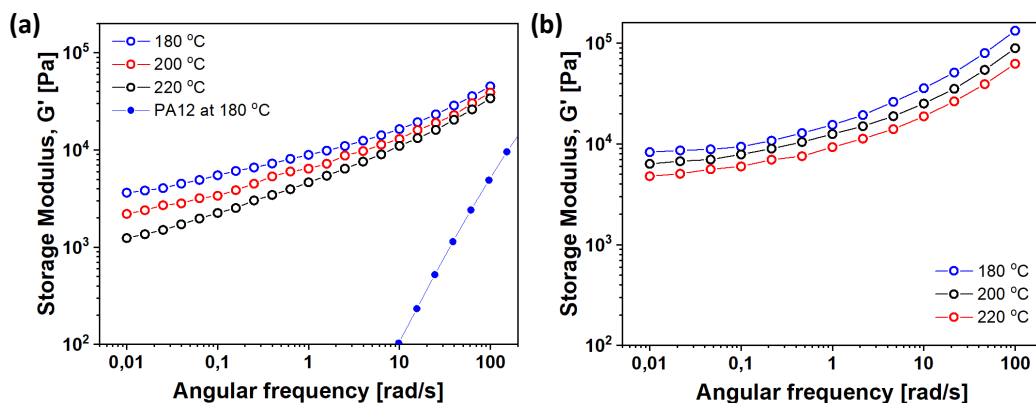


Figure 6.3: Storage modulus ( $G'$ ) response of PA12 CNT0.5 and PA12 CNT2 nanocomposites at temperatures of 180°C, 200°C and 220°C.

Frequency sweep experiments were performed for PA12 CNT0.5 and PA12 CNT2 nanocomposites, to study the elastic response ( $G'$ ) at various temperatures, as shown in Figure 6.3. A slope of 2 for  $G'$  as a function of frequency is typically indicative of terminal behavior for homopolymers [152]. This can be observed for PA12 at 180°C in Figure 6.3(a). This terminal zone behaviour is absent for both nanocomposites in presence of CNTs, for all relevant temperatures. Increasing the CNT content in PA12 brings about a higher elastic modulus and reduced frequency dependency, as can be seen by comparing Figure 6.4(a) and Figure 6.4(b). The linear dynamic moduli are a fingerprint of the microstructure of the material and more specifically, the low frequency response corresponds to relatively long structural length scales in the material. High  $G'$  values with reduced frequency dependency at low frequencies can be attributed to a more elastic structure where molecular motion is inhibited by either chain length in the case of high molecular weight single phase systems, or by a structural feature in the material such as a cocontinuous structure in immiscible polymer blends and particle network formation in well dispersed polymer nanocomposites [244, 245]. The different rheological responses of the nanocomposites as compared to that of pure PA12 and the liquid to solid transition observed when increasing the CNT content can be attributed to the network formation of CNTs in the polymer matrix in combination with a reduced mobility of the PA12 polymer chains. For PA12 CNT2, an almost frequency independent response of the storage modulus  $G'$  is apparent below 0.1 rad/s. This points to the absence of relaxations over these timescales and thus the formation of a network structure with limited mobility under quiescent conditions. With increasing temperature, the moduli slightly decrease, as a typical response to the increased mobility of the polymer chains.

The evolution of the storage modulus  $G'$  as a function of time after loading the sample in the rheometer can provide further insights in the development of the CNTs network in the polymer matrix. In Figure 6.4(a), it can be observed that PA12 CNT0.5 shows a time independent response for  $G'$  at the measurement temperatures of 180°C, 200°C and 220°C. On the other hand, for PA12 CNT2, an increase in  $G'$  for the first 2000s

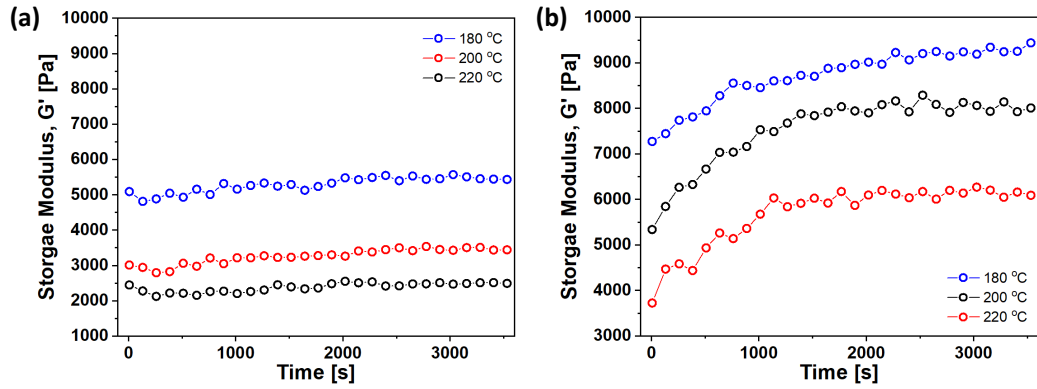


Figure 6.4: Time evolution of the linear viscoelastic storage modulus ( $G'$ ) of nanocomposites at temperatures of 180°C, 200°C and 220°C for (a) PA12 CNT0.5 and (b) PA12 CNT2.

is observed at all measured temperatures, after which  $G'$  reaches a plateau. The linear viscoelastic dynamic moduli shown in Figure 6.4 are measured after the time sweep test from Figure 6.3 to avoid any time effects in these measurements. During sample loading, care was taken to avoid squeezing the sample and no preshear was applied. Hence, the development of the elastic moduli noticeable in Figure 6.3 can be attributed to small rearrangements of the CNTs leading to enhanced interactions between them and thus more pronounced network elasticity. A time independent response of  $G'$  can be observed for PA12 CNT0.5 at all measured temperatures. However, a distinctly different behaviour can be observed for PA12 CNT2 whereby an increase in  $G'$  is observed as a function of time at all temperatures. It may be counterintuitive that the nanocomposite with the lowest mobility shows the largest amount of time evolution. However, it should also be considered that less particle movement or reorientation is required to enhance particle contacts and thus network stiffness at a high CNT content. Influence of temperature on the evolution can also be observed, wherein with increasing temperature,  $G'$  tends to saturate faster, from 3000 s to 1500 s for temperatures ranging from 180°C to 220°C. This suggests that the CNTs undergo faster network development at high temperatures since the polymer matrix chains are more mobile, whereas at lower temperatures due to a higher viscosity of the matrix network formation takes longer. The results in Figure 6.4 indicate that time-dependent network formation may play a role while melting the nanocomposites during laser sintering although the initial network state in the doublets may be quite different from that in compression moulded disks.

The effect of the CNTs is also reflected in the viscosity curves, as show in Figure 6.5 at 180°C, which shows complex viscosity curves estimated from frequency sweep measurements. PA12 without CNTs attains a constant zero shear viscosity value, whereas with addition of CNTs the viscosity increases by almost two orders of magnitude and no longer attains a low-frequency plateau within the measured frequency range. The slope of viscosity versus frequency reaches close to -1 for PA12 CNT2, which indicates the presence of a constant stress region and thus a yield stress in the material. To estimate this yield stress value, the elastic stress from oscillatory strain sweep experiments is analyzed and indeed shows a maximum for the PA12 CNT2, as illustrated in Figure 6.11 in Appendix I. This material thus behaves like a yield stress material with a yield stress

Table 6.2: Activation energy from Arrhenius plot for viscosity versus frequency at 100 rad/s for PA12, PA12 CNT0.5 and PA12 CNT2

Polymer	Activation energy, $E_a$ (KJ/mol)
PA12	32.5
PA12 CNT0.5	48.9
PA12 CNT2	61.3

of  $4.3 \times 10^4$  Pa at  $180^\circ\text{C}$ , as estimated from oscillatory experiments. Therefore during laser sintering, the stresses generated by the surface tension should overcome this yield stress, before the particles can sinter together.

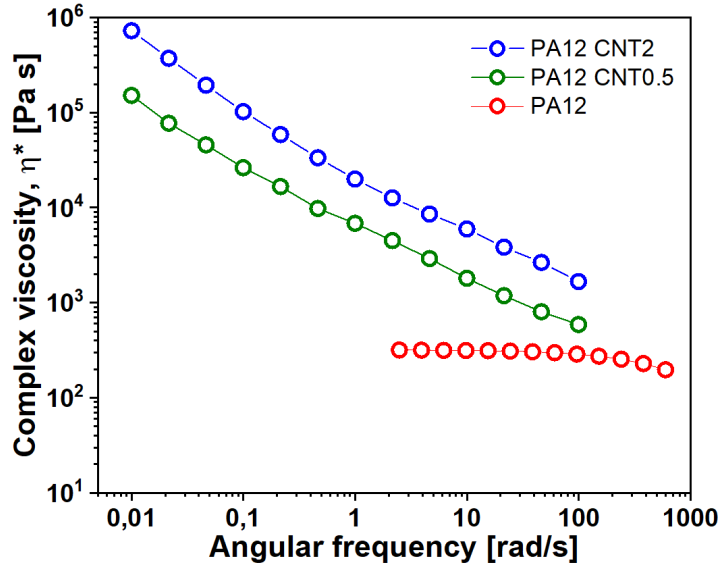


Figure 6.5: Complex viscosity of PA12, PA12 CNT0.5 and PA12 CNT2 at a temperature of  $180^\circ\text{C}$ .

To quantify the temperature dependence of the viscosity, the activation energy  $E_a$  for PA12 and PA12 nanocomposites was calculated from the slope of the viscosity  $\eta$  versus  $1/T$  at a frequency of 100 rad/s:

$$\eta = \eta_{\text{ref}} \cdot \exp\left[\frac{E_a}{R \cdot T}\right], \quad (6.3)$$

where  $\eta$  is the viscosity,  $E_a$  the activation energy,  $R$  the universal gas constant,  $T$  the temperature and  $\eta_{\text{ref}}$  the pre-exponential factor. The activation energy values (Table 6.2) of the PA12 nanocomposites increase with increasing CNTs content. A similar trend has been observed for PA6 nanocomposites wherein a CNT content of 2 wt% also increased the  $E_a$  with more than a factor 2 [246]. This suggests that incorporation of CNTs reduces the polymer mobility, thereby resulting in a higher activation energy for flow.



### 6.3.3 *In-situ* laser sintering experiments

#### 6.3.3.1 Influence of CNT content

With the main material characteristics being determined in Sections 6.3.1 and 6.3.2 and the *in-situ* sintering technique described in Section 6.2.2.3, systematic experiments are performed for particle pairs with a radius of 100  $\mu\text{m}$  and increasing CNT content. A representative experimental result for PA12 CNT0.5 is shown in Figure 6.6. Figure 6.6 shows the tracked neck growth, normalized by the particle radius, as a function of time. At the instant the laser is switched on at time  $t = 0$  s, a sudden increase in neck growth is observed, whereby the surface tension is the driving force [120]. At  $t = 1.1$  s a sharp decrease in sintering rate is observed due to heat loss leading to solidification of the material, which is complete at  $t = 4.7$  s. This can also be observed from the optical image sequence in the inset of Figure 6.6, wherein the majority of the neck growth is observed in the initial second of the process.

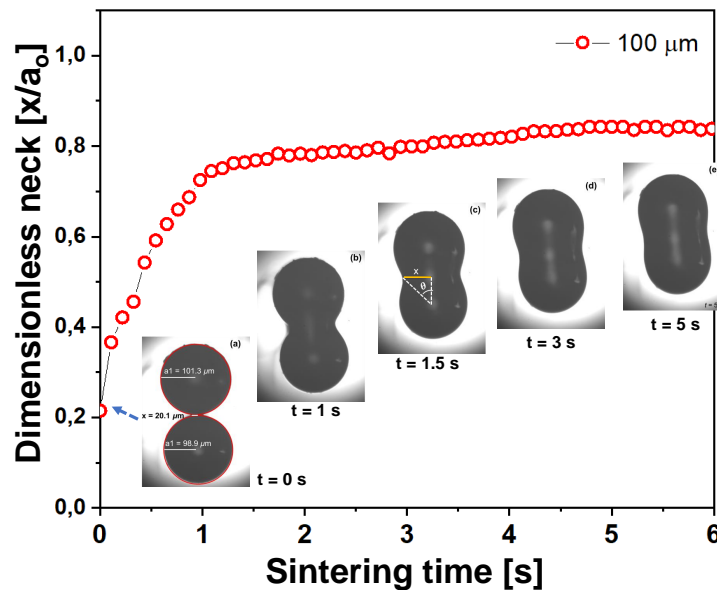


Figure 6.6: Dimensionless neck radius versus sintering time for a PA12 particle pair with 0.5 wt% CNTs, for a particle radius  $a_0 = 100 \mu\text{m}$ , chamber temperature of  $155^\circ\text{C}$  at a laser pulse energy of  $E_p = 384 \mu\text{J}$  and laser pulse duration of  $t_L = 1$  ms. Inset shows a sequence of top view images of the particle pair during sintering (a to e). The evolution of the neck radius  $x$  (yellow line in c) at the interface between the two particles is followed as a function of time.

Figure 6.7 shows the effect of increasing CNTs content on the sintering dynamics in Figure 6.7(a) as well as the corresponding crystallization kinetics in Figure 6.7(b), for a particle radius of 100  $\mu\text{m}$ . Though the overall processing conditions remain the same, different flow dynamics can be observed in Figure 6.7(a), dependent on the material. A change in the initial slope of the sintering kinetics can be observed as well as a shift in the timepoint at which sintering is halted. With increasing content of CNTs, the



sintering dynamics slows down and premature cessation of flow occurs. Thereby partial sintering of the particle doublets occurs in the case of the nanocomposite materials PA12 CNT0.5 and PA12 CNT2. This could lead to porous parts being produced in the selective laser sintering process for PA12 with CNTs. From the viscoelastic measurements in Section 6.3.2, it was observed that with increasing CNTs content, the elastic response and viscosity of the material increases. Hence, the CNTs will hinder the flow of the polymer at the interface, even though the local temperature is measured to be around 230°C (Chapter 5) at the interface of the particle doublets. Given that the particle size and laser sintering conditions are the same, the only parameter able to cause differences in temperature at the sintering zone between PA12 and PA12 nanocomposites is the thermal conductivity. Typically, the thermal conductivity increases with CNT content, in particular above the percolation threshold [247, 248]. Hence, a slightly faster heat diffusion from the sintering zone towards the exterior of the particles may be expected due to the enhanced thermal conductivity. Hence, the CNTs contribute to the slowing down of the sintering kinetics via two mechanisms. First, they will decrease flowability at a certain temperature and second they will lead to a reduction of the temperature at the sintering zone due to faster heat diffusion to the non-illuminated zone. Interestingly, even though the PA12 CNT2 nanocomposite has a relatively high yield stress, sintering can proceed initially, which indicates that the surface tension driving force is large enough to overcome the yield stress.

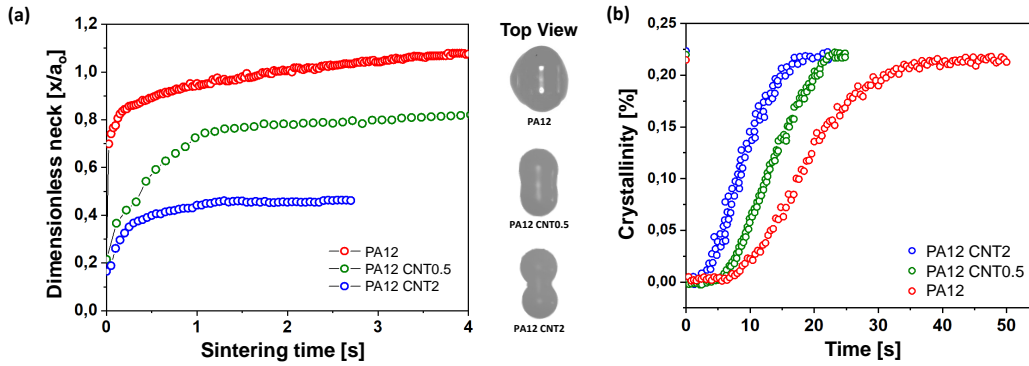


Figure 6.7: Effect of CNT content on sintering of PA12, PA12 CNT0.5 and PA12 CNT2 particle pairs of radius  $a_0 = 100 \mu\text{m}$  for a chamber temperature of 155°C, pulse energy of  $E_p = 384 \mu\text{J}$  and pulse duration of  $t_L = 1 \text{ ms}$ . (a) Dimensionless neck radius versus sintering time (b) Time evolution of crystallinity during the sintering process.

A clear difference can also be observed in the crystallization kinetics, as shown in Figure 6.7(b), wherein with increasing CNTs content the crystallization accelerates distinctly. Though the overall crystallinity remains the same at around 22%, a change in the slope of the crystallization kinetics is observed. It can be seen that with increasing CNTs content the half time of crystallization shifts from 12.5 s, over 11 s to 4.5 s, for PA12, PA12 CNT0.5 and PA12 CNT2 respectively. Furthermore, the onset of crystallization occurs earlier with increasing CNTs content, shifting from about 5.5 s, over 3.5 s to 2 s. This suggests that with increasing CNTs content, more nucleation sites are created thereby accelerating the overall crystallization kinetics. Similar effects can be observed for a bigger particle size of 150  $\mu\text{m}$  radius (see Figure 6.12 in Appendix I). To understand the importance of various effects on the crystallization kinetics, the half times of

crystallization during laser sintering can be correlated to those obtained from isothermal crystallization in calorimetric measurements (Section 6.3.1). There, the half times of crystallization at the chamber temperature of 155°C were found to be 20 s, 5 s and 1.5 s respectively for PA12, PA12 CNT0.5 and PA12 CNT2. In our previous work (Chapter 5), we already established that for pure PA12 under the given sintering conditions, flow-enhanced crystallization speeds up the crystallization (Section 5.3.1, in Chapter 5). However, for the PA12 nanocomposites, crystallization during laser sintering is slower as compared to isothermal crystallization at the chamber temperature (Section 6.3.1). This can be attributed to the non-isothermal nature of the process, whereby the temperature is on average larger than the chamber temperature and it takes around 4 s to cool down to the chamber temperature. Hence, it can not be stated with certainty whether flow-induced crystallization plays a role in the nanocomposite materials, but if present, it is dominated by the effect of the non-isothermal environmental temperature. Depending on the type of filler material, flow and particle effects are known to exhibit synergistic, additional or antagonistic effects in speeding up the crystallization kinetics [249].

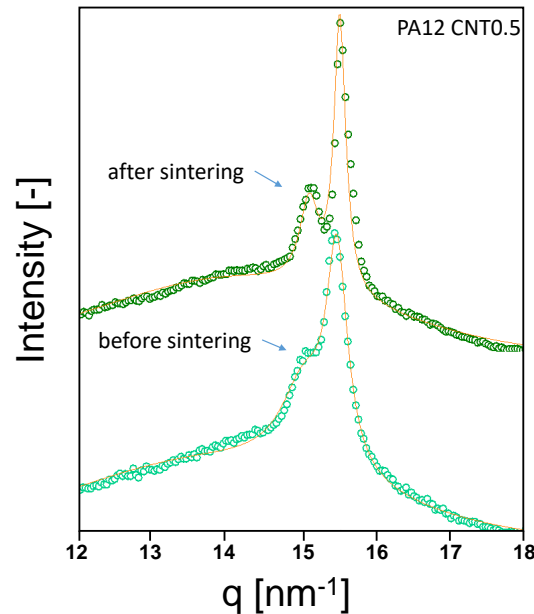


Figure 6.8: Integrated WAXD intensity and relative deconvolution analysis of before and after sintering frames for non-isothermal sintering process of PA12 CNT0.5 particle pairs of radius  $a_o = 100 \mu\text{m}$ , wherein pulse energy  $E_p = 384 \mu\text{J}$  and pulse duration  $t_L = 1 \text{ms}$  for heating chamber temperature,  $T_c$  of 155°C.

Figure 6.8 shows the integrated intensity of the WAXD patterns as a function of scattering vector  $q$ , before and after sintering for particle doublets of PA12 CNT0.5 at a chamber temperature of 155°C. The shoulder at  $q = 15.02 \text{ nm}^{-1}$  before sintering transforms into a secondary peak after sintering. The resulting two distinct peaks, namely a primary peak at  $q = 15.5 \text{ nm}^{-1}$  and a secondary peak at  $q = 15.07 \text{ nm}^{-1}$  with  $d$  spacings of 0.405 nm and 0.417 nm respectively correspond to the  $\alpha'$ -phase [126]. The latter is characteristic for PA12 at temperatures above 140°C [175]. This phase was also observed for PA12 CNT2 as well as pure PA12. After sintering, the PA12 CNT2 particle doublet

exhibited a primary diffraction peak at  $q = 15.8 \text{ nm}^{-1}$  and a secondary peak at  $q = 15.08 \text{ nm}^{-1}$  corresponding to  $d$  spacings of 0.397 and 0.416 nm respectively. The reference PA12 particle doublets (Section 5.14, in Chapter 5) resulted in  $d$  spacings after sintering of 0.418 and 0.430 nm. Therefore with increasing CNTs content,  $q$  shifts towards higher values whereas the  $d$  spacing reduces. A similar shift was observed for polyamide 6 with functionalized CNT [250].

Using the integrated WAXD pattern, the mean crystal size can be estimated from the peak width using the Scherrer equation [192]:

$$L = \frac{K\lambda}{\beta \cos \theta}, \quad (6.4)$$

where  $\lambda = 1.040880 \text{ nm}$  is the X-ray wavelength,  $\beta$  is the peak width at full width half maximum of the diffraction peak profile in radians and  $K$  is a constant related to the crystallite shape, which is normally taken as 0.9 [193]. Table 6.3 shows the estimated mean crystal size from the WAXD intensity profiles of varying CNTs content in PA12 nanocomposites for a particle radius of 100  $\mu\text{m}$ . With increasing wt% of CNTs the mean crystallite size increases. Since the addition of nanotubes increases the nucleation density while the crystal growth rate is left unaltered or slowed down [251], this is not expected. However, a lower temperature at the sintering zone can also affect the final crystal size by the enhanced crystal growth rate at lower temperatures.

Table 6.3: Mean crystal size estimated using Scherrer equation before and after sintering for varying CNTs content.

Polymer	PA12		PA12 CNT0.5		PA12 CNT2	
	Before sintering	After sintering	Before sintering	After sintering	Before sintering	After sintering
Mean crystallite size (nm)	11.3	14.7	15.1	21.6	16.28	23.2

### 6.3.3.2 Influence of PA12 particle size

Our previous work clearly demonstrated the effect of the particle size on the sintering kinetics, both directly via its effect on the driving force for sintering as well as indirectly via its effect on the temperature distribution inside the particle doublet. Figure 6.9(a) shows the neck growth kinetics for particles of PA12 CNT0.5 whereas the corresponding crystallization kinetics is plotted in Figure 6.9(b), both for three different particle sizes. From Figure 6.9(a), two main effects of the particle size can be observed. First, the final dimensionless neck radius is substantially reduced from 0.81 to 0.5 when the particle radius increases from 100  $\mu\text{m}$  to 150  $\mu\text{m}$ . This is also demonstrated by the optical images taken at  $t = 6 \text{ s}$  of the final configuration after sintering. This partial sintering is caused by a lower initial sintering rate as well as earlier reduction in the sintering speed. While the laser energy remains the same, the overall volume under irradiation increases with increasing particle radius. For the given laser spot radius of 15  $\mu\text{m}$ , with increasing particle radius a larger part of the heat energy flows to the bulk of the material. As a

result, the temperature in the neck region will be less, resulting in a higher elasticity and viscosity. This has been verified by IR imaging for laser sintering of PA12 particle doublets, where the local temperature varies from 230°C to 193°C when the particle radius is increased from 100  $\mu\text{m}$  to 150  $\mu\text{m}$  (Chapter 5). Since the activation energy for flow is higher for the PA12 nanocomposites than for PA12, this size effect may even become more pronounced for PA12 nanocomposites as compared to pure PA12. This was however not observed under the used processing conditions.

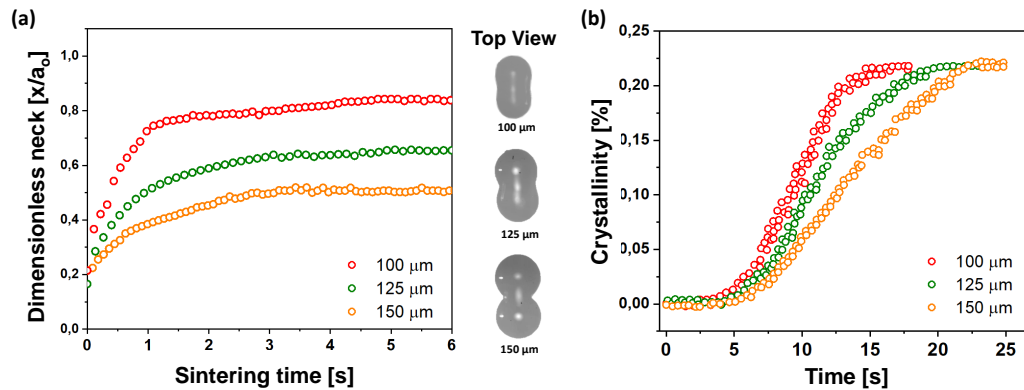


Figure 6.9: Effect of particle size on sintering process of PA12 CNT0.5 particle pairs of radius  $a_0 = 100 \mu\text{m}$ ,  $125 \mu\text{m}$  and  $150 \mu\text{m}$ , for chamber temperature of  $155^\circ\text{C}$ , pulse energy of  $E_p = 384 \mu\text{J}$  and pulse duration of  $t_L = 1 \text{ ms}$ . (a) Dimensionless neck radius versus sintering time. Top view images of melt doublet at the end of sintering process (b) Time evolution of crystallinity during the sintering process.

Figure 6.9(b) shows the corresponding in-situ time-resolved crystallization kinetics for various particle sizes of PA12 CNT0.5. It can be observed that crystallization starts after cessation of flow as shown in Figure 6.9(a). The overall crystallinity remains at around 22%, though a pronounced difference in crystallization rate is observed with varying particle size. The half time of crystallization for 100  $\mu\text{m}$ , 125  $\mu\text{m}$  and 150  $\mu\text{m}$  particles is about 9 s, 11 s and 13 s. The isothermal half time of crystallization at the chamber temperature of  $155^\circ\text{C}$  is 5 s. It was shown that smaller particles undergo faster deformation rates, which could enhance the crystallization kinetics (Section 5.3.1). Therefore the change in rate of crystallization for varying particle size (Figure 6.9(b)), could be related to the lower deformation rates with increasing particle size, which lead to a slower rate of crystallization. The effect seen here is less pronounced than for pure PA12 (Chapter 5). In addition, the time scales for crystallization during laser sintering do not correspond to the half times of crystallization obtained from isothermal calorimetry experiments, whereby the crystallization kinetics from *in-situ* experiments are slower than that in isothermal calorimetry measurements. The non-isothermal conditions experienced during laser sintering thus play a large role for the nanocomposite case. Hence, in agreement with results in the previous section, it can be concluded that enhancement of crystallization by flow is less in the nanocomposite as compared to the pure PA12.

### 6.3.4 Electrical conductivity

The addition of conductive fillers such as carbon black, carbon nanofibers, carbon nanotubes or graphene to insulating polymers induces electrical conductivity in the resulting composite. The most important factors determining the conductivity are the processing technique, processing parameters, properties of the polymer matrix, and the type of conductive filler [252, 253]. Crystallinity can greatly impact the overall electrical conductivity of polymer nanocomposites [254]. It was shown that the same resistivity could be achieved in semi-crystalline polymers as compared to amorphous materials by using a more than two times lower amount of nanofiller. CNTs would form a conductive path along the amorphous part of a semi-crystalline material, thereby the crystals provide a template to form a conducting network. Furthermore, it was shown with polypropylene that a higher crystallinity can further enhance the conductivity thereby reducing the amount of CNTs required to achieve a percolated network. This can be further enhanced with flow, wherein chain alignment in the flow direction could lead to flow-induced orientation of nano-fillers [249]. To study the effect of laser sintering on the electrical conductivity of PA12 particle doublets, the electrical conductivity of bulk nanocomposite sheets was measured by means of a linear four point probe and that of single particles and sintered doublets by means of two probes, as shown in Figure 6.1. Since the linear four point probe method can not be employed on particles and sintered doublets, a *in-situ* two probe method was developed. This method was also employed to measure and compare the conductivity of a single particle with 150  $\mu\text{m}$  radius with that of PA12 nanocomposite films characterized by the traditional four point probe. Since the geometry of the particles leads to a non-constant cross-sectional area, which complicates the analysis of the resistance data, a comparison between the volume resistivity obtained on a flat material sheet and that obtained on a single particle, forms a benchmark for the measurements of the electrical conductivity of laser sintered doublets by the two probe method.

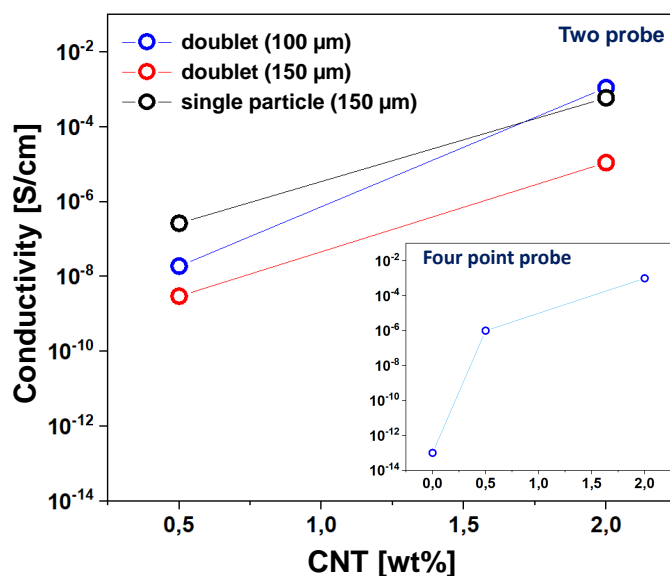


Figure 6.10: Electrical conductivity (S/cm) as a function of CNT content measured by two probe method for sintered doublets as well as a single spherical particle for PA12 CNT0.5 and PA12 CNT2. Inset shows the electrical conductivity measured by the linear four point probe for PA12, PA12 CNT0.5 and PA12 CNT2. Lines are a guide to the eye.

The inset of Figure 6.10 shows the electrical conductivity values of sheets of PA12 and P12 nanocomposites. PA12 without CNTs shows a conductivity value of 10<sup>-13</sup> S/cm, a typical value measured for polymers [255]. Addition of 0.5 wt% CNTs significantly increases this value to 10<sup>-6</sup> S/cm, and a further increase in the CNTs content to 2 wt% increases the conductivity three orders of magnitude to 10<sup>-3</sup> S/cm. The fact that these values are several orders of magnitude higher as compared to the value for pure PA12 shows that the CNTs are percolated in the polymer matrix, which was already concluded based on the high elastic moduli with low frequency dependency shown in Figure 6.3. A similar difference between the values for PA12 CNT0.5 and PA12 CNT2 could be found when measuring the conductivity of single particles by the two point probe method. However, the absolute values measured with the two point probe method are a factor 100 lower than the electrical conductivity measured on the polymer sheets. This could partially be caused by the different measurement setup, and effects of the contact resistance. However, it should also be kept in mind that apart from the geometry, both materials underwent a completely different processing history. The particles were prepared by solution mixing followed by evaporation whereas the polymer sheets underwent an additional processing step via compression moulding. This additional processing step may enhance the electrical conductivity via two different mechanisms. First, annealing at high temperature is known to cause additional structure development in nanocomposites [256, 257], as can also be seen in Figure 6.4 for the storage modulus. Second, as mentioned above, in semi-crystalline polymers the electrical conductivity can highly depend on the crystal size and structure since crystals can expel the CNTs and can thereby alter the CNT network. Hence, the different solidification processes in both cases could

have led to a different network structure in the polymer sheets as compared to the particles. Therefore, the values obtained on the particles will be used as the reference for the characterization of the electrical conductivity of the sintered doublets.

In Figure 6.10 the conductivity values of the sintered doublets are compared with that of a single particle. Apart from the 100  $\mu\text{m}$  radius particles of PA12 CNT2, the sintered doublets show electrical conductivity values that are one to two orders of magnitude lower as compared to that of the starting material. This loss of electrical conductivity may be attributed to some orientation of the CNTs in the direction of the neck growth, which is the direction perpendicular to the one for which the electrical conductivity was measured. Moreover, as it is shown in the previous sections that laser sintering leads to recrystallization resulting in larger crystals, this may also affect the network structure of the CNTs and thus the electrical conductivity in the sintered bridge. Moreover, the smallest particles, which exhibit the largest bridge width, also show a slightly larger electrical conductivity. Although the intrinsic conductivity should not depend on the geometry of the sample, in this case a smaller particle size entails changes in both the flow kinematics of the sintering process as well as the kinetics of the crystallization process which may quite well result in a different microstructure. When comparing the results of PA12 CNT0.5 and PA12 CNT2 for the single particle and the sintered particle doublets, it can be concluded that the concentration dependence of the 150  $\mu\text{m}$  particles is similar to that of the single particle whereas in the case of the 100  $\mu\text{m}$  particles, the PA12 CNT2 shows enhanced conductivity. This may be related to less pronounced flow and altered crystallization behaviour.

## 6.4 Conclusions

Laser sintering of PA12 nanocomposite particles was studied with an in-house developed setup. By means of in-situ visualization with optical microscopy and X-ray scattering, the sintering dynamics as well as the crystallization kinetics were captured for various particle radii and with CNT contents of 0.5 wt% and 2 wt%. The bulk starting material was systematically characterized for its optical, rheological, thermal and crystallization properties to be able to analyze the different phenomena occurring during the sintering process. The incorporation of carbon nanotubes (CNTs) in the semi-crystalline polymer led to a faster isothermal crystallization kinetics with crystallization half times that were reduced by an order of magnitude for PA12 CNT2 as compared to pure PA12. Furthermore, rheological measurements showed an increased viscosity for increasing CNT content, and a transition from a liquid-like to a solid-like behaviour. The sintering experiments showed that, under the same processing conditions, nanocomposites exhibit a slower sintering kinetics and faster crystallization. Hence, the doublets obtained after sintering show a less developed neck in the case of nanocomposites. This suppressed sintering behaviour is caused by the higher viscosity and more elastic behaviour of the nanocomposites as compared to pure PA12. For a given nanocomposite composition, there is also a dependence on the particle size, whereby smaller particles sinter faster and exhibit a faster crystallization kinetics. Since the smaller particles are at a higher

temperature during sintering, the trend in the crystallization kinetics suggests that flow-enhanced crystallization occurs. However, the flow effect is substantially suppressed as compared to the sintering of pure PA12. The electrical conductivity of the sintered doublets was measured with an in-house developed two probe method. With 2 wt% CNTs the electrical conductivity reaches values that are high enough for applications such as EM shielding while the surface tension is still strong enough to overcome the yield stress of the material and allows sintering. The sintering process itself slightly reduces the electrical conductivity as compared to that of the starting material, which can be attributed to an altered orientation and distribution of the CNTs in the material due to the flow and recrystallization of the material. From our study, it can be concluded that the presence of carbon nanotubes in PA12 affects the sintering and crystallization kinetics via several mechanisms. First, the nanotubes clearly suppress the flow behaviour of the polymer thereby slowing down the sintering kinetics. Second, they alter the temperature distribution in the doublet by enhancing the thermal conductivity. And last, they have a clear effect on the crystallization kinetics whereby both particle and flow effects can interact with each other. When considering the final electrical conductivity of the sintered doublet, again both the flow as well as the thermal history are relevant for the final conductivity values, which are affected by the microstructure of the material. Therefore, it is clear from our work that a rational design of laser sintered polymer nanocomposites is a non-trivial task and should take into account the interaction between flow, thermal history and microstructure development on the level of the particles as well as that of the crystals.

## Acknowledgements

This work forms part of the research programme of the Brightlands Materials Center (BMC). We acknowledge the European Synchrotron Radiation Facility (ESRF) for provision of synchrotron radiation facilities and NWO for financing beam time at ESRF. We thank Dr. Daniel Hermida Merino for assistance in using the Dutch-Belgian beamline (DUBBLE) BM26 and Prof.Dr.ir. Leon E. Govaert for providing the PA12 polymer.



## Appendix

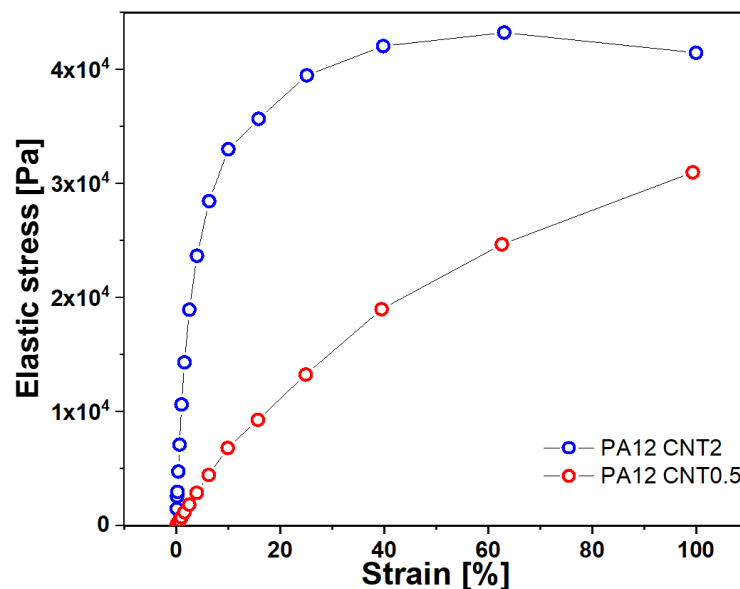


Figure 6.11: Elastic stress from strain sweep experiments for PA12 CNT0.5 and PA12 CNT2 at 180°C.

Strain sweep experiments were performed for the nanocomposites. The storage modulus response was multiplied by corresponding strain % to get a elastic stress.

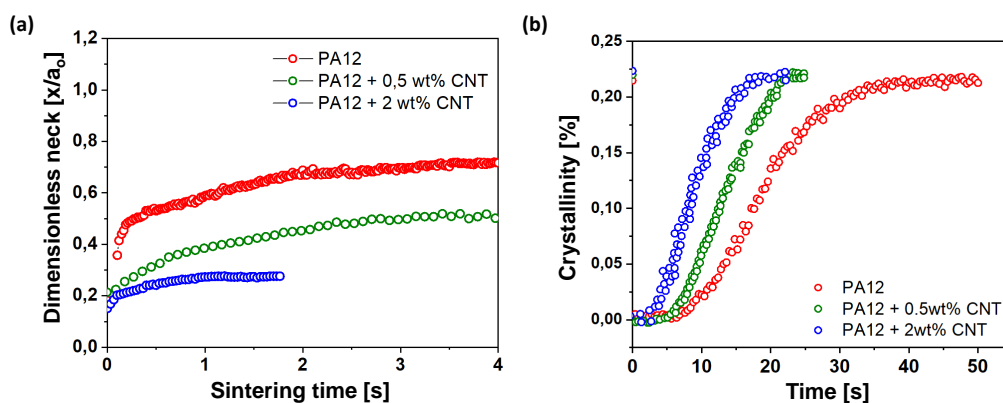


Figure 6.12: Effect of CNT content on sintering process of PA12, PA12 CNT0.5 and PA12 CNT2 particle pairs of radius  $a_0 = 150 \mu\text{m}$  for a chamber temperature of 155°C, pulse energy of  $E_p = 384 \mu\text{J}$  and pulse duration of  $t_L = 1 \text{ ms}$ . (a) Dimensionless neck radius versus sintering time (b) Time evolution of crystallinity during the sintering process.

## Conclusions and Recommendations

### 7.1 Conclusions

Fundamental insights in the sintering kinetics of amorphous and semi-crystalline polymer powder particles during selective laser sintering (SLS) are developed. Simplifying this complex process by studying only a single polymer particle pair allows us to relate the essential processing conditions to the observed sintering dynamics. To exclude the effects of ill-defined powder particle shapes, be it for amorphous or semi-crystalline polymers, an economic and simple method is described to make the powder particles perfectly spherical. A unique in-house experimental setup is developed to perform laser sintering experiments on a single particle pair. This setup gives us the opportunity to in-situ study the actual sintering process by optical, infrared (IR) and X-ray imaging. Optics provide information on the flow response during melting, neck formation and solidification of the particle pair. Also having access to X-ray during laser sintering of semi-crystalline polymer particles reveals the crystallization kinetics and microstructure development. IR imaging further supplements in providing temperature evolution and heat diffusion. With this setup, the sintering of amorphous polystyrene as well as semi-crystalline polyamide 12 (PA12) and polyamide 12 conductive nanocomposites containing carbon nanotubes was studied. This research adds to the understanding on the intrinsic mechanisms that influence an actual laser sintering process, to eventually be able to optimize this process and tailor it so as to obtain desired properties.

#### 7.1.1 Chapter 2: A processing route to spherical polymer particles via controlled drop retraction

- A methodology based on the shape retraction of liquid droplets is developed to transform randomly shaped powder particles to a perfectly spherical shape. Versatility of the method is described for various thermoplastic polymers and a comparison of shape factors between the starting material and particles after the rounding process shows the potential of the method.
- Optimization of the process is possible by considering the time required for shape retraction and choosing processing conditions to reduce undesired droplet dynamics

processes such as breakup, collision, coalescence and sedimentation. The temperature is crucial to shift the characteristic retraction time of the droplet within a time frame that largely excludes particle interactions.

### 7.1.2 Chapter 3: A novel experimental setup for *in-situ* optical and X-ray imaging of laser sintering of polymer particles

- A unique in-house developed experimental laser sintering setup has been designed and constructed that has the ability to allow in-situ time-resolved microscopic and X-ray observations of laser sintering with precise control over all sintering parameters.
- A case study on the sintering of PA12 particle pairs demonstrates that real-time information on the sintering dynamics as well as crystallization kinetics can be obtained with a good signal-to-noise ratio and sufficient spatial and temporal resolution.
- Structure evolution and crystallization kinetics during laser sintering are complex and coupled processes involving non-isothermal, non-homogeneous temperature profiles and complex flow fields. This laser sintering setup provides direct access to essential local and time-resolved information about the structural processes involved, which cannot be obtained from commercially available SLS machines.

### 7.1.3 Chapter 4: Laser sintering of polymer particle pairs studied by *in-situ* visualization

- Laser sintering experiments are performed on amorphous spherical polystyrene particle pairs of various sizes, such that the ratio of laser spot size to particle size is varied between 0.19 and 0.66. The thermal, rheological and laser-light absorption properties of the used polystyrene are characterized a priori. This allows to determine the suitable parameter range for the heating chamber temperature, laser pulse duration and laser pulse energy.
- A systematic study of the effects of the main laser sintering parameters on the sintering dynamics, quantified as the evolution of the neck radius between both particles with time, is performed. This provided time-resolved information on the laser sintering of polymer particles. The initial sintering kinetics as a function of time could be described with the modified Frenkel model for isothermal sintering of viscous liquids, whereby the characteristic viscosity depends on the applied processing conditions.
- The overall sintering kinetics is determined by a complex interplay between temperature and time effects on the viscosity. Contrary to thermal sintering in a homogeneously heated chamber, laser-induced particle sintering can slow down and even completely halt at later stages. This is caused by the viscosity build-up as a function of time due to the cooling down of the particles and the finite relaxation time of the material. Hence, if the supplied laser energy is not sufficient to cause a substantial temperature increase, only partial sintering occurs.

#### 7.1.4 Chapter 5: Laser sintering of PA12 particles studied by *in-situ* optical, thermal and X-ray characterization

- Characterisation of the thermal, rheological and laser light absorption properties of PA12 polymer with 2 wt% dye allowed us to derive the appropriate parameter range for laser energy and chamber temperature.
- Simultaneously capturing the flow by optical imaging and the crystallization kinetics from WAXD patterns, in combination with IR imaging, a complex interplay between temperature, flow and crystallization kinetics is shown.
- Under the same processing conditions, the local temperature experienced at the interphase of the doublets is higher for smaller particles. This is caused by the fact that the same amount of laser energy is available for a smaller volume of material. An opposite trend is observed for crystallization, where the kinetics is faster for smaller particles, which would not be expected based on the higher temperature.
- Since the deformation rates experienced during sintering are higher for smaller particles, flow-induced crystallization can explain the faster crystallization kinetics of small particles. An estimate of the critical Weissenberg numbers based on the Rouse and reptation times suggests that under the studied process conditions the polymer chains can orient but not stretch. This can enhance the number density of nuclei, thereby speeding up crystallization.

#### 7.1.5 Chapter 6: Laser sintering of polyamide 12/carbon nanotube composite particle pairs

- The incorporation of MWCNTs in the semi-crystalline polymer increased the crystallization kinetics, since the MWCNTs act as nucleation sites. Furthermore, rheological measurements show an increase in elastic modulus and viscosity with an increase in MWCNT content, eventually leading to a solid-like material at 2 wt% MWCNTs.
- Under identical processing conditions for various particle sizes, smaller particles show faster sintering and crystallization kinetics, similar to the results for pure PA12. Smaller particles undergo higher deformation rates, which enhances the rate of crystallization.
- Increasing particle size leads to premature cessation of flow, since the local temperature at the interface is lower thereby increasing the viscosity. A similar trend is observed for PA12 with increasing MWCNT content, whereby the flow properties of the material are reduced due to the presence of the MWCNTs.
- In general, the electrical conductivity increases with increasing concentrations of MWCNTs in the nanocomposites. Sintered doublets showed a higher electrical conductivity with increased neck width at the interface of the particles.

## 7.2 Recommendations

In the present work, the focus has been on understanding fundamental aspects defining the sintering kinetics of polymer particle pairs. In reality during an actual 3D SLS printing process a bed of polymer powder particles is utilized. A step towards approaching this aspect is to start from stacking two layers of particles in height direction. This will provide more insight in the penetration depth of the laser energy through this multi-layer construct of particles. Simultaneous IR imaging can provide information on the heat-diffusion process and correlate this to the observed sintering kinetics obtained from optical microscopy. It can be hypothesized that the neck growth could be slower due to presence of a larger material volume; thereby laser energy and spot size, together with pulse duration will be critical parameters to take into account. These experimental results can further be correlated to simulations [144]. Stacking of particles could ideally be approached by increasing the voltage in the micromanipulator[81, 117].

The current experimental setup is designed with manual control. Automation of the translation stages and replacing the stand-alone laser by a scanning system (Galvo mirror) can further bring this setup closer to an actual SLS machine. This could allow probing a string of monolayer particles to visualize and understand the sintering dynamics by optical microscopy from top and IR imaging from the side view, as implemented in our current setup. This methodology would certainly work with a large field of view of IR as well as *in-situ* optical visualization through scanner. *in-situ* X-ray visualization would be possible, but restricted to a fixed location of interest, since a high energy X-ray source is required to achieve a high signal-to-noise ratio which are usually fixed standalone setups.

In-situ X-ray experiments showed a shift in crystallization of PA12 particles. Weissenberg numbers estimated showed an increase in orientation of chain can lead fastening of the crystallization kinetics. Ideally this could be observed with change in intensity of rings in the diffraction pattern by WAXD, though this could not be realized since the X-ray source had a spot size of 100  $\mu\text{m}$ . For the given size of PA12 particles used and the X-ray spot size, yield averaged information on time resolved crystallization kinetics. Ex-situ measurements with micro/nano X-ray beam on the final melt doublets can provide more detailed information on structure formation along the melt doublet. Performing in-situ experiments with smaller spot size of X-ray beam can provide time resolved local change in orientation, at the interface of the polymer particles during and after sintering.

Temperature of the powder bed before laser sintering is critical in achieving complete sintering and avoiding porosity within the part. Current usage of an IR heater in an SLS machine is not efficient in doing so. Using a dual laser during the print process could circumvent this issue. First the laser source is utilized in scanning the desired path by locally raising the temperature and a simultaneous scan along the same path by the second laser allows to sinter the polymer powder. This can be a better mechanism in controlling the heat distribution during the process. Furthermore, polymer powder which has no prior heat treatment can be reused with a reduced to no aging effect.

Printing parts with functional properties (Chapter 6) is an upcoming potential area from a research as well final product point of view. This requires materials specific to end product requirements. It was shown that introducing filler particles to enhance mechanical and/or conducting properties can drastically influence the flow as well as crystallization kinetics. A clever approach would be to use a compatibilizer which can enhance the flow and at the same time enhances the dispersion of the filler particles in a cocontinuous morphology [258]. As a start this can be done by developing blends, either by extrusion or solution casting, and later producing spherical particles (Chapter 2) to be tested with the in-house developed laser sintering setup (Chapter 3). The polarity of the thermoplastic polymer used would have an influence on the eventual dispersion.

One of the future attempts would be to connect the experimentally observed laser sintering process of polymer particles (this Thesis) with predictions of a numerical framework for laser sintering of semi-crystalline and amorphous polymers [16]. This can be taken a step further by studying the mechanical strength of the interface of a sintered doublet. This micro-scale testing could be in-part connected to the bulk mechanical measurements done on laser sintered products [17].



## Bibliography

- [1] G. N. Levy, R. Schindel, and J. P. Kruth. Rapid manufacturing and rapid tooling with layer manufacturing (lm) technologies, state of the art and future perspectives. *CIRP annals*, 52(2):589–609, 2003.
- [2] I. Gibson and D. Shi. Material properties and fabrication parameters in selective laser sintering process. *Rapid prototyping journal*, 1997.
- [3] X. Yan and P. Gu. A review of rapid prototyping technologies and systems. *Computer-aided design*, 28(4):307–318, 1996.
- [4] S. Kumar. Selective laser sintering: a qualitative and objective approach. *Jom*, 55(10):43–47, 2003.
- [5] I. Yadroitsev and I. Smurov. Selective laser melting technology: from the single laser melted track stability to 3d parts of complex shape. *Physics Procedia*, 5: 551–560, 2010.
- [6] C. Yan, Y. Shi, J. Yang, and J. Liu. Investigation into the selective laser sintering of styrene–acrylonitrile copolymer and postprocessing. *The International journal of advanced manufacturing technology*, 51(9-12):973–982, 2010.
- [7] M. Schmid, A. Amado, and K. Wegener. Polymer powders for selective laser sintering (sls). In *AIP Conference proceedings*, volume 1664, page 160009. AIP Publishing LLC, 2015.
- [8] H. Scholten and W. Christoph. Use of a nylon-12 for selective laser sintering, June 12 2001. US Patent 6,245,281.
- [9] N. K. Tolochko, Y. V. Khlopkov, S. E. Mozzharov, M. B. Ignatiev, T. Laoui, and V. I. Titov. Absorptance of powder materials suitable for laser sintering. *Rapid Prototyping Journal*, 2000.
- [10] C. W. Buckley and T. L. Bergman. An experimental investigation of heat affected zone formation and morphology development during laser processing of metal powder mixtures. *J. Heat Transfer*, 123(3):586–592, 2001.
- [11] I. S. Kinstlinger, A. Bastian, S. J. Paulsen, D. H. Hwang, A. H. Ta, D. R. Yalacki, Tim Schmidt, and J. S. Miller. Open-source selective laser sintering (opensls) of nylon and biocompatible polycaprolactone. *PloS one*, 11(2):e0147399, 2016.
- [12] R. D. Goodridge, C. J. Tuck, and R. J. M. Hague. Laser sintering of polyamides and other polymers. *Progress in Materials science*, 57(2):229–267, 2012.



- [13] Y. Shi, Z. Li, H. Sun, S. Huang, and F. Zeng. Effect of the properties of the polymer materials on the quality of selective laser sintering parts. *Proceedings of the Institution of Mechanical Engineers, Part L: Journal of Materials: Design and Applications*, 218(3):247–252, 2004.
- [14] N. Hopkinson, C. E. Majewski, and H. Zarringhalam. Quantifying the degree of particle melt in selective laser sintering<sup>®</sup>(<sup>®</sup>). *CIRP annals*, 58(1):197–200, 2009.
- [15] P. Hejmady, L. C. A. Van Breemen, P. D. Anderson, and R. Cardinaels. Selective laser sintering of polymeric particles: Experimental visualization. December 2017.
- [16] C. Balemans. *Computational analysis of polymer powder sintering for 3D printing*. PhD thesis, Department of Mechanical Engineering, Technische Universiteit Eindhoven, October 2019. PhD Thesis.
- [17] F. Paolucci. *Characterisation of crystallisation kinetics and mechanical properties of Polyamide 12*. PhD thesis, Department of Mechanical Engineering, Technische Universiteit Eindhoven, July 2019. PhD Theis.
- [18] M. Schmid. *Laser Sintering with Plastics: Technology, Processes, and Materials*. Carl Hanser Verlag GmbH Co KG, 2018.
- [19] W. H. Suh, A. R. Jang, Y-H Suh, and K. S. Suslick. Porous, hollow, and ball-in-ball metal oxide microspheres: preparation, endocytosis, and cytotoxicity. *Advanced Materials*, 18(14):1832–1837, 2006.
- [20] H. K. Chan. Dry powder aerosol drug delivery—opportunities for colloid and surface scientists. *Colloids and Surfaces A: Physicochemical and Engineering Aspects*, 284:50–55, 2006.
- [21] F. Iskandar. Nanoparticle processing for optical applications—a review. *Advanced Powder Technology*, 20(4):283–292, 2009.
- [22] C. Gath and D. Drummer. Circuit board application to additive manufactured components by laser-direct-structuring. In *2016 12th International Congress Molded Interconnect Devices (MID)*, pages 1–6. IEEE, 2016.
- [23] J. P. Kruth, X. Wang, T. Laoui, and L. Froyen. Lasers and materials in selective laser sintering. *Assembly Automation*, 2003.
- [24] D. Drummer and F. Rietzel, D.and Kühnlein. Development of a characterization approach for the sintering behavior of new thermoplastics for selective laser sintering. *Physics Procedia*, 5:533–542, 2010.
- [25] M. Schmid, A. Amado, and K. Wegener. Materials perspective of polymers for additive manufacturing with selective laser sintering. *Journal of Materials Research*, 29(17):1824–1832, 2014.
- [26] M. Schmid and K. Wegener. Additive manufacturing: polymers applicable for laser sintering (ls). *Procedia Engineering*, 149:457–464, 2016.

- [27] A. Wegner. New polymer materials for the laser sintering process: Polypropylene and others. *Physics Procedia*, 83:1003–1012, 2016.
- [28] D. L. Bourell, T. J. Watt, D. K. Leigh, and B. Fulcher. Performance limitations in polymer laser sintering. *Physics Procedia*, 56:147–156, 2014.
- [29] A. B. D. Nandiyanto and K. Okuyama. Progress in developing spray-drying methods for the production of controlled morphology particles: From the nanometer to submicrometer size ranges. *Advanced Powder Technology*, 22(1):1–19, 2011.
- [30] F. E. Baumann and N. Wilczok. Preparation of precipitated polyamide powders of narrow particle size distribution and low porosity, August 3 1999. US Patent 5,932,687.
- [31] S. J. Wang, J. Y. Liu, L. Q. Chu, H. Zou, S. J. Zhang, and C. J. Wu. Preparation of polypropylene microspheres for selective laser sintering via thermal-induced phase separation: Roles of liquid–liquid phase separation and crystallization. *Journal of Polymer Science Part B: Polymer Physics*, 55(4):320–329, 2017.
- [32] H. Matsuyama, M. Teramoto, M. Kuwana, and Y. Kitamura. Formation of polypropylene particles via thermally induced phase separation. *Polymer*, 41(24):8673–8679, 2000.
- [33] P. Schaaf, B. Lotz, and J. C. Wittmann. Liquid-liquid phase separation and crystallization in binary polymer systems. *Polymer*, 28(2):193–200, 1987.
- [34] S. Kloos, M. A. Dechet, W. Peukert, and J. Schmidt. Production of spherical semi-crystalline polycarbonate microparticles for additive manufacturing by liquid-liquid phase separation. *Powder Technology*, 335:275–284, 2018.
- [35] W. H. Hou and T. B. Lloyd. A new technique for preparing monodisperse polymer particles. *Journal of applied polymer science*, 45(10):1783–1788, 1992.
- [36] M. A. Dechet, A. Goblirsch, S. Romeis, M. Zhao, F. J. Lanyi, J. Kaschta, D. W. Schubert, D. Drummer, W. Peukert, and J. Schmidt. Production of polyamide 11 microparticles for additive manufacturing by liquid-liquid phase separation and precipitation. *Chemical Engineering Science*, 197:11–25, 2019.
- [37] J. J. Blaker, J. C. Knowles, and R. M. Day. Novel fabrication techniques to produce microspheres by thermally induced phase separation for tissue engineering and drug delivery. *Acta biomaterialia*, 4(2):264–272, 2008.
- [38] M. E. Nichols and R. E. Robertson. Preparation of small poly (butylene terephthalate) spheres by crystallization from solution. *Journal of Polymer Science Part B: Polymer Physics*, 32(3):573–577, 1994.
- [39] M. A. Dechet, A. Demina, L. Roemling, J. S. G. Bonilla, F. J. Lanyi, D. W. Schubert, A. Bueck, W. Peukert, and J. Schmidt. Development of poly (l-lactide)(plla) microspheres precipitated from triacetin for application in powder bed fusion of polymers. *Additive Manufacturing*, 32:100966, 2020.

- [40] M. A. Dechet, I. Baumeister, and J. Schmidt. Development of polyoxymethylene particles via the solution-dissolution process and application to the powder bed fusion of polymers. *Materials*, 13(7):1535, 2020.
- [41] G. Wang, P. Wang, Z. Zhen, W. Zhang, and J. Ji. Preparation of pa12 microspheres with tunable morphology and size for use in sls processing. *Materials & Design*, 87:656–662, 2015.
- [42] M. A. Dechet, A. Demina, L. Roemling, J. S. G. Bonilla, F. J. Lanyi, D. W. Schubert, A. Bueck, W. Peukert, and J. Schmidt. Development of poly (l-lactide)(plla) microspheres precipitated from triacetin for application in powder bed fusion of polymers. *Additive Manufacturing*, 32:100966, 2020.
- [43] E. Reverchon. Supercritical antisolvent precipitation of micro-and nano-particles. *The journal of supercritical fluids*, 15(1):1–21, 1999.
- [44] J. Yang, D. Katagiri, S. Mao, H. Zeng, H. Nakajima, and K. Uchiyama. Generation of controlled monodisperse porous polymer particles by dipped inkjet injection. *RSC advances*, 5(10):7297–7303, 2015.
- [45] I. H. Choi and J. Kim. A pneumatically driven inkjet printing system for highly viscous microdroplet formation. *Micro and Nano Systems Letters*, 4(1):4, 2016.
- [46] J. Schmidt, M. Sachs, S. Fanselow, M. Zhao, S. Romeis, D. Drummer, Karl-Ernst Wirth, and W. Peukert. Optimized polybutylene terephthalate powders for selective laser beam melting. *Chemical Engineering Science*, 156:1–10, 2016.
- [47] Y. He, Y. Y. Li, T. J. Evans, A. B. Yu, and R. Y. Yang. Effects of particle characteristics and consolidation pressure on the compaction of non-spherical particles. *Minerals Engineering*, 137:241–249, 2019.
- [48] D. Drummer, M. Medina-Hernández, M. Drexler, and K. Wudy. Polymer powder production for laser melting through immiscible blends. *Procedia engineering*, 102:1918–1925, 2015.
- [49] S. Fanselow, S. E. Emamjomeh, K. E. Wirth, J. Schmidt, and W. Peukert. Production of spherical wax and polyolefin microparticles by melt emulsification for additive manufacturing. *Chemical Engineering Science*, 141:282–292, 2016.
- [50] Y. Zhou, S. Xi, Y. Huang, Miqiu Kong, Q. Yang, and G. Li. Preparation of near-spherical pa12 particles for selective laser sintering via plateau-rayleigh instability of molten fibers. *Materials & Design*, 190:108578, 2020.
- [51] S. B. Liang, D. P. Hu, C. Zhu, and A. B. Yu. Production of fine polymer powder under cryogenic conditions. *Chemical engineering & technology*, 25(4):401–405, 2002.
- [52] P. J. Brunner, J. M. Torkelson, and K. Wakabayashi. Toward better understanding of solid-state shear pulverization. *Society of Plastics Engineers (SPE)*, 10, 2012.
- [53] H. Kawaguchi. Functional polymer microspheres. *Progress in polymer science*, 25(8):1171–1210, 2000.

- [54] M. Liang, C. Lu, Y. Huang, and C. Zhang. Morphological and structural development of poly (ether ether ketone) during mechanical pulverization. *Journal of applied polymer science*, 106(6):3895–3902, 2007.
- [55] M. Wilczek, J. Bertling, and Hintemann. D. Optimised technologies for cryogenic grinding. *Int. J. Miner. Process*, 74(8):425, 2004.
- [56] K. Khait, S. H. Carr, and M. H. Mack. *Solid-state shear pulverization*. CRC Press, 2001.
- [57] S. Xi, P. Zhang, Y. Huang, M. Kong, Q. Yang, and G. Li. Laser sintering of cryogenically ground polymer powders into high-performance parts: The role of dry particle coating with a conductive flow agent. *Polymer*, 186:122044, 2020.
- [58] N. Mys, R. Van De Sande, A. Verberckmoes, and L. Cardon. Processing of polysulfone to free flowing powder by mechanical milling and spray drying techniques for use in selective laser sintering. *Polymers*, 8(4):150, 2016.
- [59] J. Schmidt, M. Sachs, C. Blümel, B. Winzer, F. Toni, Karl-Ernst Wirth, and W. Peukert. A novel process route for the production of spherical lbm polymer powders with small size and good flowability. *Powder technology*, 261:78–86, 2014.
- [60] S. Wu. Calculation of interfacial tension in polymer systems. In *Journal of Polymer Science Part C: Polymer Symposia*, volume 34, pages 19–30. Wiley Online Library, 1971.
- [61] D. R. Paul and S. Newman. Polymer blends academic press. *Inc. New York*, 1:65, 1978.
- [62] S. Wu. Interfacial and surface tensions of polymers. *Journal of Macromolecular Science—Reviews in Macromolecular Chemistry*, 10(1):1–73, 1974.
- [63] B. Esteban, J. R. Riba, G. Baquero, R. Puig, and A. Rius. Characterization of the surface tension of vegetable oils to be used as fuel in diesel engines. *Fuel*, 102: 231–238, 2012.
- [64] S. J. Underwood and J. M. Gorham. Challenges and approaches for particle size analysis on micrographs of nanoparticles loaded onto textile surfaces. *NIST Special Publication*, 1200:22, 2017.
- [65] Representation of results of particle size analysis — Part 6: Descriptive and quantitative representation of particle shape and morphology. Technical report, 2008. URL <https://www.iso.org/standard/39389.html>.
- [66] S. Berretta, O. Ghita, and K. E. Evans. Morphology of polymeric powders in laser sintering (ls): From polyamide to new peek powders. *European Polymer Journal*, 59:218–229, 2014.
- [67] B. Chen, Y. Wang, S. Berretta, and O. Ghita. Poly aryl ether ketones (paeks) and carbon-reinforced paek powders for laser sintering. *Journal of Materials Science*, 52(10):6004–6019, 2017.

- [68] T. Chatterjee and R. Krishnamoorti. Rheology of polymer carbon nanotubes composites. *Soft Matter*, 9(40):9515–9529, 2013.
- [69] R. Cardinaels and P. Moldenaers. Morphology development in immiscible polymer blends. *Polymer Morphology. Principles, Characterization and Properties*; Guo, Q., Ed, pages 348–373, 2016.
- [70] P. Van Puyvelde, A. Vananroye, R. Cardinaels, and P. Moldenaers. Review on morphology development of immiscible blends in confined shear flow. *Polymer*, 49(25):5363–5372, 2008.
- [71] M. Saito and A. Yabe. Dispersion and polar force components of surface tension of oily soils. *Textile Research Journal*, 54(1):18–22, 1984.
- [72] C. M. Hansen. *Hansen solubility parameters: a user’s handbook*. CRC press, 2007.
- [73] H. P. Grace. Dispersion phenomena in high viscosity immiscible fluid systems and application of static mixers as dispersion devices in such systems. *Chemical Engineering Communications*, 14(3-6):225–277, 1982.
- [74] M. Spoerk, J. Gonzalez-Gutierrez, C. Lichal, H. Cajner, G. R. Berger, S. Schuschnigg, L. Cardon, and C. Holzer. Optimisation of the adhesion of polypropylene-based materials during extrusion-based additive manufacturing. *Polymers*, 10(5):490, 2018.
- [75] J. S. G. Bonilla, M. A. Dechet, J. Schmidt, W. Peukert, and A. Bück. Thermal rounding of micron-sized polymer particles in a downer reactor: direct vs indirect heating. *Rapid Prototyping Journal*, 2020.
- [76] M. Sachs, M. Friedle, J. Schmidt, W. Peukert, and Karl-Ernst Wirth. Characterization of a downer reactor for particle rounding. *Powder Technology*, 316:357–366, 2017.
- [77] N. P. Karapatis, J. P. S. Van Griethuysen, and R. Glardon. Direct rapid tooling: a review of current research. *Rapid prototyping journal*, 1998.
- [78] S. Dadbakhsh, L. Verbelen, T. Vandeputte, D. Strobbe, P. Van Puyvelde, and J. P. Kruth. Effect of powder size and shape on the sls processability and mechanical properties of a tpu elastomer. *Physics Procedia*, 83:971–980, 2016.
- [79] S. Ziegelmeier, F. Wöllecke, C. Tuck, R. Goodridge, and R. Hague. Characterizing the bulk & flow behaviour of ls polymer powders. In *Proceedings SFF Symposium, Austin (TX), USA*, 2013.
- [80] S. Ziegelmeier, P. Christou, F. Wöllecke, C. Tuck, R. Goodridge, R. Hague, E. Krampe, and E. Wintermantel. An experimental study into the effects of bulk and flow behaviour of laser sintering polymer powders on resulting part properties. *Journal of Materials Processing Technology*, 215:239–250, 2015.
- [81] P. Hejmady, L. C. A. Van Breemen, P. D. Anderson, and R. Cardinaels. Laser sintering of polymer particle pairs studied by in situ visualization. *Soft matter*, 15(6):1373–1387, 2019.

- [82] P. Hejmady, L. C. Cleven, L. C. A. Van Breemen, P. D. Anderson, and R. Cardinaels. A novel experimental setup for in situ optical and x-ray imaging of laser sintering of polymer particles. *Review of Scientific Instruments*, 90(8):083905, 2019.
- [83] S. Haeri, Y. Wang, O. Ghita, and J. Sun. Discrete element simulation and experimental study of powder spreading process in additive manufacturing. *Powder Technology*, 306:45–54, 2017.
- [84] S. Haeri. Optimisation of blade type spreaders for powder bed preparation in additive manufacturing using dem simulations. *Powder Technology*, 321:94–104, 2017.
- [85] C. R. Deckard. Method and apparatus for producing parts by selective sintering, September 5 1989. US Patent 4,863,538.
- [86] K. H. Tan, C. K. Chua, K. F. Leong, C. M. Cheah, W. S. Gui, W. S. Tan, and F. E. Wiria. Selective laser sintering of biocompatible polymers for applications in tissue engineering. *Bio-medical materials and engineering*, 15(1, 2):113–124, 2005.
- [87] E. Radstok. Rapid tooling. *Rapid Prototyping Journal*, 1999.
- [88] E. MacDonald and R. Wicker. Multiprocess 3d printing for increasing component functionality. *Science*, 353(6307), 2016.
- [89] F. S. Fogliatto and G. J. C. Da Silveira. *Mass customization: engineering and managing global operations*. Springer Science & Business Media, 2010.
- [90] I. Gibson, D. W. Rosen, and B. Stucker. Design for additive manufacturing. In *Additive manufacturing technologies*, pages 299–332. Springer, 2010.
- [91] H. Zarringhalam, C. Majewski, and N. Hopkinson. Degree of particle melt in nylon-12 selective laser-sintered parts. *Rapid Prototyping Journal*, 2009.
- [92] E. Moeskops, N. Kamperman, B. van de Vorst, and R. Knoppers. Creep behaviour of polyamide in selective laser sintering 60. In *2004 International Solid Freeform Fabrication Symposium*, 2004.
- [93] M. Vasquez, B. Haworth, and N. Hopkinson. Methods for quantifying the stable sintering region in laser sintered polyamide-12. *Polymer Engineering & Science*, 53(6):1230–1240, 2013.
- [94] C. T. Bellehumeur, M. K. Bisaria, and J. Vlachopoulos. An experimental study and model assessment of polymer sintering. *Polymer Engineering & Science*, 36(17):2198–2207, 1996.
- [95] C. T. Bellehumeur, M. Kontopoulou, and J. Vlachopoulos. The role of viscoelasticity in polymer sintering. *Rheologica acta*, 37(3):270–278, 1998.
- [96] S. Aid, A. Eddhahak, Z. Ortega, D. Froelich, and A. Tcharkhtchi. Predictive coalescence modeling of particles from different polymers: application to pvdf and pmma pair. *Journal of Materials Science*, 52(19):11725–11736, 2017.

- [97] C. Balemans, N. O. Jaensson, M. A. Hulsen, and P. D. Anderson. Temperature-dependent sintering of two viscous particles. *Additive Manufacturing*, 24:528–542, 2018.
- [98] R. J. Roe and R. J. Roe. *Methods of X-ray and neutron scattering in polymer science*, volume 739. Oxford University Press New York, 2000.
- [99] W. Zhu, C. Yan, Y. Shi, S. Wen, J. Liu, and Y. Shi. Investigation into mechanical and microstructural properties of polypropylene manufactured by selective laser sintering in comparison with injection molding counterparts. *Materials & Design*, 82:37–45, 2015.
- [100] J. Chang, Z. Wang, X. Tang, F. Tian, K. Ye, and L. Li. A portable extruder for in situ wide angle x-ray scattering study on multi-dimensional flow field induced crystallization of polymer. *Review of Scientific Instruments*, 89(2):025101, 2018.
- [101] S. Rendon, J. Fang, W. R. Burghardt, and R. A. Bubeck. An apparatus for in situ x-ray scattering measurements during polymer injection molding. *Review of Scientific Instruments*, 80(4):043902, 2009.
- [102] E. M. Troisi, M. Van Drongelen, H. J. M. Caelers, G. Portale, and G. W. M. Peters. Structure evolution during film blowing: An experimental study using in-situ small angle x-ray scattering. *European polymer journal*, 74:190–208, 2016.
- [103] J. E. Seppala and K. D. Migler. Infrared thermography of welding zones produced by polymer extrusion additive manufacturing. *Additive manufacturing*, 12:71–76, 2016.
- [104] L. A. Northcutt, S. V. Orski, K. B. Migler, and A. P. Kotula. Effect of processing conditions on crystallization kinetics during materials extrusion additive manufacturing. *Polymer*, 154:182–187, 2018.
- [105] C. L. A. Leung, S. Marussi, Robert C. Atwood, M. Towrie, P. J. Withers, and P. D. Lee. In situ x-ray imaging of defect and molten pool dynamics in laser additive manufacturing. *Nature communications*, 9(1):1–9, 2018.
- [106] Q. Guo, C. Zhao, L. I. Escano, Z. Young, L. X., K. Fezzaa, W. Everhart, B. Brown, T. Sun, and L. Chen. Transient dynamics of powder spattering in laser powder bed fusion additive manufacturing process revealed by in-situ high-speed high-energy x-ray imaging. *Acta Materialia*, 151:169–180, 2018.
- [107] C. Zhao, K. Fezzaa, R. W. Cunningham, H. Wen, F. De Carlo, L. Chen, A. D. Rollett, and T. Sun. Real-time monitoring of laser powder bed fusion process using high-speed x-ray imaging and diffraction. *Scientific reports*, 7(1):1–11, 2017.
- [108] W. M. Steen and J. Mazumder. *Laser material processing*. springer science & business media, 2010.
- [109] G. Portale, D. Cavallo, G. C. Alfonso, D. Hermida-Merino, M. Van Drongelen, L. Balzano, G. W. M. Peters, J. G. P. Goossens, and W. Bras. Polymer crystallization studies under processing-relevant conditions at the saxs/waxs dubble beamline at the esrf. *Journal of applied crystallography*, 46(6):1681–1689, 2013.

- [110] A. P. Hammersley. Fit2d: an introduction and overview. *European Synchrotron Radiation Facility Internal Report ESRF97HA02T*, 68:58, 1997.
- [111] R. Androsch, M. L. Di Lorenzo, and C. Schick. Effect of molar mass on enthalpy relaxation and crystal nucleation of poly (l-lactic acid). *European Polymer Journal*, 96:361–369, 2017.
- [112] F. Paolucci, D. Baeten, P. C. Roozmond, B. Goderis, and G. W. M. Peters. Quantification of isothermal crystallization of polyamide 12: Modelling of crystallization kinetics and phase composition. *Polymer*, 155:187–198, 2018.
- [113] C. Y. Liu, J. He, R. Keunings, and C. Bailly. New linearized relation for the universal viscosity- temperature behavior of polymer melts. *Macromolecules*, 39 (25):8867–8869, 2006.
- [114] L. Verbelen, S. Dadbakhsh, M. Van den Eynde, J. P. Kruth, B. Goderis, and P. Van Puyvelde. Characterization of polyamide powders for determination of laser sintering processability. *European Polymer Journal*, 75:163–174, 2016.
- [115] B. B. Sauer and Gregory T. Dee. Surface tension and melt cohesive energy density of polymer melts including high melting and high glass transition polymers. *Macromolecules*, 35(18):7024–7030, 2002.
- [116] M. Yuan, T. T. Diller, D. Bourell, and J. Beaman. Thermal conductivity of polyamide 12 powder for use in laser sintering. *Rapid Prototyping Journal*, 2013.
- [117] H. Kawamoto and K. Tsuji. Manipulation of small particles utilizing electrostatic force. *Advanced Powder Technology*, 22(5):602–607, 2011.
- [118] M. Wu, T. Cubaud, and Chih-Ming Ho. Scaling law in liquid drop coalescence driven by surface tension. *Physics of Fluids*, 16(7):L51–L54, 2004.
- [119] A. J. Shaler. Seminar on the kinetics of sintering. *JOM*, 1(11):796–813, 1949.
- [120] O. Pokluda, C. T. Bellehumeur, and J. Vlachopoulos. Modification of frenkel’s model for sintering. *AIChE journal*, 43(12):3253–3256, 1997.
- [121] E. Scribber, D. Baird, and P. Wapperom. The role of transient rheology in polymeric sintering. *Rheologica acta*, 45(6):825–839, 2006.
- [122] W. M. Rohsenow, J. P. Hartnett, Y. I. Cho, et al. *Handbook of heat transfer*, volume 3. McGraw-Hill New York, 1998.
- [123] F. P. Incropera, Adrienne S. Lavine, T. L. Bergman, and D. P. DeWitt. *Fundamentals of heat and mass transfer*. Wiley, 2007.
- [124] L. Li, Michel H. J. Koch, and Wim H. de Jeu. Crystalline structure and morphology in nylon-12: A small-and wide-angle x-ray scattering study. *Macromolecules*, 36 (5):1626–1632, 2003.
- [125] N. Dencheva, T. G. Nunes, M. J. Oliveira, and Z. Denchev. Crystalline structure of polyamide 12 as revealed by solid-state  $^{13}\text{C}$  nmr and synchrotron waxes and saxs. *Journal of Polymer Science Part B: Polymer Physics*, 43(24):3720–3733, 2005.



- [126] C. Ramesh. Crystalline transitions in nylon 12. *Macromolecules*, 32(17):5704–5706, 1999.
- [127] S. Dadbakhsh, L. Verbelen, O. Verkinderen, D. Strobbe, P. Van Puyvelde, and J. P. Kruth. Effect of pa12 powder reuse on coalescence behaviour and microstructure of sls parts. *European Polymer Journal*, 92:250–262, 2017.
- [128] N. Hiramatsu, K. Haraguchi, and S. Hirakawa. Study of transformations among  $\alpha$ ,  $\gamma$  and  $\gamma'$  forms in nylon 12 by x-ray and dsc. *Japanese Journal of Applied Physics*, 22(2R):335, 1983.
- [129] S. Dupin, O. Lame, C. Barrès, and J. Y. Charneau. Microstructural origin of physical and mechanical properties of polyamide 12 processed by laser sintering. *European Polymer Journal*, 48(9):1611–1621, 2012.
- [130] E. M. Troisi, H. J. M. Caelers, and G. W. M. Peters. Full characterization of multiphase, multimorphological kinetics in flow-induced crystallization of ipp at elevated pressure. *Macromolecules*, 50(10):3868–3882, 2017.
- [131] J. P. Kruth, M. C. Leu, and T. Nakagawa. Progress in additive manufacturing and rapid prototyping. *CIRP Annals-Manufacturing Technology*, 47(2):525–540, 1998.
- [132] J. P. Kruth, P. Mercelis, J. Van Vaerenbergh, L. Froyen, and M. Rombouts. Binding mechanisms in selective laser sintering and selective laser melting. *Rapid prototyping journal*, 11(1):26–36, 2005.
- [133] T. H. C. Childs, M. Berzins, G. R. Ryder, and A. Tontowi. Selective laser sintering of an amorphous polymer—simulations and experiments. *Proceedings of the Institution of Mechanical Engineers, Part B: Journal of Engineering Manufacture*, 213(4):333–349, 1999.
- [134] Z. L. Lu, Y. S. Shi, J. H. Liu, Y. Chen, and S. H. Huang. Manufacturing aisi304 metal parts by indirect selective laser sintering combined with isostatic pressing. *The International Journal of Advanced Manufacturing Technology*, 39(11-12):1157–1163, 2008.
- [135] M. Schmidt, D. Pohle, and T. Rechtenwald. Selective laser sintering of peek. *CIRP annals*, 56(1):205–208, 2007.
- [136] D. Drummer, K. Wudy, F. Kühnlein, and M. Drexler. Polymer blends for selective laser sintering: material and process requirements. *Physics Procedia*, 39:509–517, 2012.
- [137] K. H. Tan, C.K. Chua, K. F. Leong, C. M. Cheah, P. Cheang, M. S. A. Bakar, and S. W. Cha. Scaffold development using selective laser sintering of polyetheretherketone–hydroxyapatite biocomposite blends. *Biomaterials*, 24(18):3115–3123, 2003.
- [138] N. Rosenzweig et al. Coalescence phenomenology of spherical polymer particles by sintering. 1980.

- [139] P. R. Hornsby and A. S. Maxwell. Mechanism of sintering between polypropylene beads. *Journal of materials science*, 27(9):2525–2533, 1992.
- [140] G. C. Kuczynski, B. Neuville, and H. P. Toner. Study of sintering of poly (methyl methacrylate). *Journal of Applied Polymer Science*, 14(8):2069–2077, 1970.
- [141] J. J. Frenkel. Viscous flow of crystalline bodies under the action of surface tension. *Journal of Physics*, 9:385, 1945.
- [142] S. Berretta, Y. Wang, R. Davies, and O. R. Ghita. Polymer viscosity, particle coalescence and mechanical performance in high-temperature laser sintering. *Journal of Materials Science*, 51(10):4778–4794, 2016.
- [143] J. D. Muller, M. Bousmina, and A. Maazouz. 2d-sintering kinetics of two model fluids as drops. *Macromolecules*, 41(6):2096–2103, 2008.
- [144] C. Balemans, M. A. Hulsen, and P. D. Anderson. Sintering of two viscoelastic particles: a computational approach. *Applied Sciences*, 7(5):516, 2017.
- [145] D. T. Pham and R. S. Gault. A comparison of rapid prototyping technologies. *International Journal of machine tools and manufacture*, 38(10-11):1257–1287, 1998.
- [146] A. D. Pasquino and M. N. Pilsworth Jr. The thermal conductivity of polystyrene, oriented and unoriented, with measurements of the glass-transition temperature. *Journal of Polymer Science Part B: Polymer Letters*, 2(3):253–255, 1964.
- [147] H. Höcker, G. J. Blake, and P. J. Flory. Equation-of-state parameters for polystyrene. *Transactions of the Faraday Society*, 67:2251–2257, 1971.
- [148] S. Wu. Polymer interface and adhesion. 1982.
- [149] D. H. Ballard. Generalizing the hough transform to detect arbitrary shapes. *Pattern recognition*, 13(2):111–122, 1981.
- [150] J. Hintermeyer, A. Herrmann, R. Kahlau, C. Goiceanu, and E. A. Rossler. Molecular weight dependence of glassy dynamics in linear polymers revisited. *Macromolecules*, 41(23):9335–9344, 2008.
- [151] J. P. Kruth, G. Levy, F. Klocke, and T. H. C. Childs. Consolidation phenomena in laser and powder-bed based layered manufacturing. *CIRP annals*, 56(2):730–759, 2007.
- [152] C. W. Macosko. Rheology principles. *Measurements and Applications*, 1994.
- [153] P. Lomellini. Williams-landel-ferry versus arrhenius behaviour: polystyrene melt viscoelasticity revised. *Polymer*, 33(23):4983–4989, 1992.
- [154] J. D. Muller, K. Lamnawar, and A. Maazouz. Relationship between rheological and surface properties for the sintering process of polymers. *Journal of Materials Science*, 47(1):121–131, 2012.
- [155] J. Eggers, J. R. Lister, and H. A. Stone. Coalescence of liquid drops. *arXiv preprint physics/9903017*, 1999.

- [156] F. A. Morrison et al. *Understanding rheology*. Oxford University Press, USA, 2001.
- [157] F. Varnik, A. Rios, M. Gross, and I. Steinbach. Simulation of viscous sintering using the lattice boltzmann method. *Modelling and Simulation in Materials Science and Engineering*, 21(2):025003, 2013.
- [158] E. O. Olakanmi, R. F. Cochrane, and K. W. Dalgarno. A review on selective laser sintering/melting (sls/slm) of aluminium alloy powders: Processing, microstructure, and properties. *Progress in Materials Science*, 74:401–477, 2015.
- [159] J. P. Kruth, G. Levy, R. Schindel, T. Craeghs, and E. Yasa. Consolidation of polymer powders by selective laser sintering. In *Proceedings of the 3rd International Conference on Polymers and Moulds Innovations*, pages 15–30, 2008.
- [160] B. Wendel, D. Rietzel, F. Kühnlein, R. Feulner, G. Hülder, and E. Schmachtenberg. Additive processing of polymers. *Macromolecular materials and engineering*, 293(10):799–809, 2008.
- [161] E. Berry, J. M. Brown, M. Connell, C. M. Craven, N. D. Efford, A. Radjenovic, and M. A. Smith. Preliminary experience with medical applications of rapid prototyping by selective laser sintering. *Medical engineering & physics*, 19(1):90–96, 1997.
- [162] D. Rietzel, F. Kühnlein, R. Feulner, G. Hülder, C. Von Wilmowsky, C. Fruth, E. Nkenke, and E. Schmachtenberg. Breaking material limitations in selective laser sintering-an opportunity for medical additive processing. In *SPE European Conference on Medical Polymers, Belfast, UK*, pages 61–65, 2008.
- [163] B. Pukánszky, Is. Mudra, and P. Staniek. Relation of crystalline structure and mechanical properties of nucleated polypropylene. *Journal of Vinyl and Additive Technology*, 3(1):53–57, 1997.
- [164] S. Josupeit, Hans-Joachim Schmid, S. Tutzschky, and M. Gessler. Powder ageing and material properties of laser sintered polyamide 12 using low refresh rates. In *Neue Entwicklungen in der Additiven Fertigung*, pages 63–78. Springer, 2015.
- [165] F. Fina, A. Goyanes, S. Gaisford, and A. W. Basit. Selective laser sintering (sls) 3d printing of medicines. *International journal of pharmaceutics*, 529(1-2):285–293, 2017.
- [166] H. J. Niu and I. T. H. Chang. Selective laser sintering of gas atomized m2 high speed steel powder. *Journal of materials science*, 35(1):31–38, 2000.
- [167] T. S. Böhmer. *Characterisation of a prototype solar three-dimensional printer*. PhD thesis, University of Pretoria, 2018.
- [168] A. Franco and L. Romoli. Characterization of laser energy consumption in sintering of polymer based powders. *Journal of Materials Processing Technology*, 212(4): 917–926, 2012.

- [169] E. Schmachtenberg, M. Schoenfeld, and T. Seul. Material optimization of pa12 laser sintering powder to improve surface quality. In *ANTEC Annual Technical Conference, Charlotte/USA*, 2006.
- [170] P. Peyre, Y. Rouchausse, D. Defauchy, and G. Régnier. Experimental and numerical analysis of the selective laser sintering (sls) of pa12 and pekk semi-crystalline polymers. *Journal of Materials Processing Technology*, 225:326–336, 2015.
- [171] D. King and T. Tansey. Alternative materials for rapid tooling. *Journal of Materials Processing Technology*, 121(2-3):313–317, 2002.
- [172] M. Zhao, K. Wudy, and D. Drummer. Crystallization kinetics of polyamide 12 during selective laser sintering. *Polymers*, 10(2):168, 2018.
- [173] C. J. G. Plummer, J. E. Zanetto, P. E. Bourban, and J. A. E Månson. The crystallization kinetics of polyamide-12. *Colloid and Polymer Science*, 279(4):312–322, 2001.
- [174] M. Van Drongelen, P. C. Roozmond, E. M. Troisi, A. K. Doufas, and G. W. M. Peters. Characterization of the primary and secondary crystallization kinetics of a linear low-density polyethylene in quiescent-and flow-conditions. *Polymer*, 76: 254–270, 2015.
- [175] F. Paolucci, L. E. Govaert, and G. W. M. Peters. In situ waxd and saxs during tensile deformation of moulded and sintered polyamide 12. *Polymers*, 11(6):1001, 2019.
- [176] R. Massaro, P. C. Roozmond, M. D’Haese, and P. Van Puyvelde. Flow-induced crystallization of polyamide-6. *International Polymer Processing*, 33(3):327–335, 2018.
- [177] A. Wegner and G. Witt. Process monitoring in laser sintering using thermal imaging. In *SFF Symposium, Austin, Texas, USA*, pages 8–10, 2011.
- [178] M. Schmid, R. Kleijnen, M. Vetterli, and K. Wegener. Influence of the origin of polyamide 12 powder on the laser sintering process and laser sintered parts. *Applied Sciences*, 7(5):462, 2017.
- [179] H. C. H. Ho, I. Gibson, and W. L. Cheung. Effects of energy density on morphology and properties of selective laser sintered polycarbonate. *Journal of Materials Processing Technology*, 89:204–210, 1999.
- [180] M. Zhao, D. Drummer, K. Wudy, and M. Drexler. Sintering study of polyamide 12 particles for selective laser melting. *International Journal of Recent Contributions from Engineering, Science & IT (iJES)*, 3(1):28–33, 2015.
- [181] P. Hejmady, L. C Cleven, L. C. A. Van Breemen, P. D. Anderson, and R. Cardinaels. Polymer spheres, April 2020. 19156044.0-1102.
- [182] A. M. Rhoades, N. Wonderling, C. Schick, and R. Androsch. Supercooling-controlled heterogeneous and homogenous crystal nucleation of polyamide 11 and its effect onto the crystal/mesophase polymorphism. *Polymer*, 106:29–34, 2016.

- [183] A. Mollova, R. Androsch, D. Mileva, C. Schick, and A. Benhamida. Effect of supercooling on crystallization of polyamide 11. *Macromolecules*, 46(3):828–835, 2013.
- [184] F. Paolucci, M. J. H. van Mook, L. E. Govaert, and G. W. M. Peters. Influence of post-condensation on the crystallization kinetics of pa12: from virgin to reused powder. *Polymer*, 175:161–170, 2019.
- [185] C. Balemans, P. Hejmady, R. Cardinaels, and P. D. Anderson. Towards unraveling the sintering process of two polystyrene particles by numerical simulations. *Korea-Australia Rheology Journal*, 31(4):285–295, 2019.
- [186] C. Balemans, M. A. Hulsen, and P. D. Anderson. On the validity of 2d analysis of non-isothermal sintering in sls. *Chemical Engineering Science*, 213:115365, 2020.
- [187] J. van Meerveld, G. W. M. Peters, and M. Hütter. Towards a rheological classification of flow induced crystallization experiments of polymer melts. *Rheologica Acta*, 44(2):119–134, 2004.
- [188] M. Doi, S. F. Edwards, and S. F. Edwards. *The theory of polymer dynamics*, volume 73. oxford university press, 1988.
- [189] D. Cavallo, F. Azzurri, L. Balzano, S. S. Funari, and G. C. Alfonso. Flow memory and stability of shear-induced nucleation precursors in isotactic polypropylene. *Macromolecules*, 43(22):9394–9400, 2010.
- [190] P. C. Roozmond, R. J. A. Steenbakkens, and G. W. M. Peters. A model for flow-enhanced nucleation based on fibrillar dormant precursors. *Macromolecular Theory and Simulations*, 20(2):93–109, 2011.
- [191] G. Grosso, E. M. Troisi, N. O. Jaensson, G. W. M. Peters, and P. D. Anderson. Modelling flow induced crystallization of ipp: Multiple crystal phases and morphologies. *Polymer*, 182:121806, 2019.
- [192] P. Scherrer. Bestimmung der inneren struktur und der gröÙe von kolloidteilchen mittels röntgenstrahlen. In *Kolloidchemie Ein Lehrbuch*, pages 387–409. Springer, 1912.
- [193] A. Monshi, M. R. Foroughi, and M. R. Monshi. Modified scherrer equation to estimate more accurately nano-crystallite size using xrd. *World journal of nano science and engineering*, 2(3):154–160, 2012.
- [194] R. Androsch and C. Schick. Crystal nucleation of polymers at high supercooling of the melt. In *Polymer Crystallization I*, pages 257–288. Springer, 2015.
- [195] Q. Zhang, D. Myers, J. Lan, S. A. Jenekhe, and G. Cao. Applications of light scattering in dye-sensitized solar cells. *Physical Chemistry Chemical Physics*, 14(43):14982–14998, 2012.
- [196] H. B. Zhang, Q. Yan, W. G. Zheng, Z. He, and Z. Z. Yu. Tough graphene- polymer microcellular foams for electromagnetic interference shielding. *ACS applied materials & interfaces*, 3(3):918–924, 2011.

- [197] N. Yousefi, X. Sun, X. Lin, X. Shen, J. Jia, B. Zhang, B. Tang, M. Chan, and J. K. Kim. Highly aligned graphene/polymer nanocomposites with excellent dielectric properties for high-performance electromagnetic interference shielding. *Advanced Materials*, 26(31):5480–5487, 2014.
- [198] M. H. Al-Saleh, W. H. Saadeh, and U. Sundararaj. EMI shielding effectiveness of carbon based nanostructured polymeric materials: a comparative study. *Carbon*, 60:146–156, 2013.
- [199] R. Yadav, M. Tirumali, X. Wang, M. Naebe, and B. Kandasubramanian. Polymer composite for antistatic application in aerospace. *Defence Technology*, 16:107–118, 2020.
- [200] H. Munstedt and Z. Stary. Is electrical percolation in carbon-filled polymers reflected by rheological properties? *Polymer*, 98:51–60, 2016.
- [201] W. Bauhofer and J. Z. Kovacs. A review and analysis of electrical percolation in carbon nanotube polymer composites. *Composites Science and Technology*, 69(10):1486–1498, 2009.
- [202] Z. Li, Z. Wang, X. Gan, D. Fu, G. Fei, and H. Xia. Selective laser sintering 3d printing: A way to construct 3d electrically conductive segregated network in polymer matrix. *Macromolecular Materials and Engineering*, 302(11):1700211, 2017.
- [203] F. Deng, Q. S. Zheng, L. F. Wang, and C. W. Nan. Effects of anisotropy, aspect ratio, and nonstraightness of carbon nanotubes on thermal conductivity of carbon nanotube composites. *Applied Physics Letters*, 90(2):021914, 2007.
- [204] R. Zhang, A. Dowden, H. Deng, M. Baxendale, and T. Peijs. Conductive network formation in the melt of carbon nanotube/thermoplastic polyurethane composite. *Composites Science and Technology*, 69(10):1499–1504, 2009.
- [205] P. V. Kodgire, A. R. Bhattacharyya, S. Bose, N. Gupta, A. R. Kulkarni, and A. Misra. Control of multiwall carbon nanotubes dispersion in polyamide6 matrix: An assessment through electrical conductivity. *Chemical physics letters*, 432(4-6):480–485, 2006.
- [206] M. Moniruzzaman and K. I. Winey. Polymer nanocomposites containing carbon nanotubes. *Macromolecules*, 39(16):5194–5205, 2006.
- [207] P. Pötschke, A. R. Bhattacharyya, A. Janke, S. Pegel, A. Leonhardt, C. Täschner, M. Ritschel, S. Roth, B. Hornbostel, and J. Cech. Melt mixing as method to disperse carbon nanotubes into thermoplastic polymers. *Fullerenes, nanotubes, and carbon nanostructures*, 13(S1):211–224, 2005.
- [208] V. Choudhary and A. Gupta. Polymer/carbon nanotube nanocomposites. *Carbon nanotubes-polymer nanocomposites*, 2011:65–90, 2011.
- [209] S. Chatterjee, F. A. Nüesch, and Bryan T. T. Chu. Comparing carbon nanotubes and graphene nanoplatelets as reinforcements in polyamide 12 composites. *Nanotechnology*, 22(27):275714, 2011.

- [210] C. J. Ko, C. Y. Lee, F. H. Ko, H. L. Chen, and T. C. Chu. Highly efficient microwave-assisted purification of multiwalled carbon nanotubes. *Microelectronic engineering*, 73:570–577, 2004.
- [211] A. Agarwal, S. R. Bakshi, and D. Lahiri. *Carbon nanotubes: reinforced metal matrix composites*. CRC press, 2018.
- [212] A. Mazzoli. Selective laser sintering in biomedical engineering. *Medical & biological engineering & computing*, 51(3):245–256, 2013.
- [213] K. Shahzad, J. Deckers, J. P. Kruth, and J. Vleugels. Additive manufacturing of alumina parts by indirect selective laser sintering and post processing. *Journal of Materials Processing Technology*, 213(9):1484–1494, 2013.
- [214] S. F. S. Shirazi, S. Gharehkhani, M. Mehrali, H. Yarmand, H. S. C. Metselaar, N. A. Kadri, and N. A. A. Osman. A review on powder-based additive manufacturing for tissue engineering: selective laser sintering and inkjet 3d printing. *Science and technology of advanced materials*, 2015.
- [215] R. Rensberger, R. van de Zande, H. Delaney, E. Zaretsky, W. Rakowski, J. J. Kingsley, C. H. Schilling, J. H. Adair, J. Beaman, J. Barlow, et al. Three materials reports. *Materials Technology*, 12(2):74–78, 1997.
- [216] C. R. Deckard. Selective laser sintering. *U. S. Patent*, 1990.
- [217] K. Wudy and D. Drummer. Infiltration behavior of thermosets for use in a combined selective laser sintering process of polymers. *JOM*, 71(3):920–927, 2019.
- [218] N. Hopkinson, R. Hague, and P. Dickens. *Rapid manufacturing: an industrial revolution for the digital age*. John Wiley & Sons, 2006.
- [219] A. Amado, M. Schmid, and K. Wegener. Simulation of warpage induced by non-isothermal crystallization of co-polypropylene during the sls process. In *AIP Conference Proceedings*, volume 1664, page 160002. AIP Publishing LLC, 2015.
- [220] M. Schmid, F. Amado, G. Levy, and K. Wegener. Flowability of powders for selective laser sintering (sls) investigated by round robin test. In *High Value Manufacturing: Advanced Research in Virtual and Rapid Prototyping: Proceedings of the 6th International Conference on Advanced Research in Virtual and Rapid Prototyping*, page 95, 2013.
- [221] S. Yuan, J. Bai, C. K. Chua, J. Wei, and K. Zhou. Material evaluation and process optimization of cnt-coated polymer powders for selective laser sintering. *Polymers*, 8(10):370, 2016.
- [222] K. R. Meyer, K. H. Hornung, R. Feldmann, and H. J. Smigarski. Method for polytropically precipitating polyamide powder coating compositions where the polyamides have at least 10 aliphatically bound carbon atoms per carbonamide group, June 8 1982. US Patent 4,334,056.

- [223] Y. Zhang, K. Song, J. Meng, and M. L. Minus. Tailoring polyacrylonitrile interfacial morphological structure by crystallization in the presence of single-wall carbon nanotubes. *ACS applied materials & interfaces*, 5(3):807–814, 2013.
- [224] A. Bernasconi, F. Cosmi, and D. Dreossi. Local anisotropy analysis of injection moulded fibre reinforced polymer composites. *Composites Science and Technology*, 68(12):2574–2581, 2008.
- [225] D. Zindani and K. Kumar. An insight into additive manufacturing of fiber reinforced polymer composite. *International Journal of Lightweight Materials and Manufacture*, 2(4):267–278, 2019.
- [226] Y. Chunze, S. Yusheng, Y. Jinsong, and L. Jinhui. A nanosilica/nylon-12 composite powder for selective laser sintering. *Journal of Reinforced Plastics and Composites*, 28(23):2889–2902, 2009.
- [227] H. Chung and S. Das. Functionally graded nylon-11/silica nanocomposites produced by selective laser sintering. *Materials Science and Engineering: A*, 487(1-2): 251–257, 2008.
- [228] J. Bai, R. D. Goodridge, Richard J. M. Hague, M. Song, and M. Okamoto. Influence of carbon nanotubes on the rheology and dynamic mechanical properties of polyamide-12 for laser sintering. *Polymer testing*, 36:95–100, 2014.
- [229] J. Bai, R. D. Goodridge, S. Yuan, K. Zhou, C. K. Chua, and J. Wei. Thermal influence of cnt on the polyamide 12 nanocomposite for selective laser sintering. *Molecules*, 20(10):19041–19050, 2015.
- [230] A. H. Espera Jr, A. D. Valino, J. O. Palaganas, L. Souza, Q. Chen, and R. C. Advincula. 3d printing of a robust polyamide-12-carbon black composite via selective laser sintering: Thermal and electrical conductivity. *Macromolecular Materials and Engineering*, 304(4):1800718, 2019.
- [231] M. J. Thompson, D. C. Whalley, and N. Hopkinson. Investigating dielectric properties of sintered polymers for rapid manufacturing. In *2008 International Solid Freeform Fabrication Symposium*, 2008.
- [232] S. Berretta, K. E. Evans, and O. R. Ghita. Predicting processing parameters in high temperature laser sintering (ht-ls) from powder properties. *Materials & Design*, 105:301–314, 2016.
- [233] J. Kim and T. S. Creasy. Selective laser sintering characteristics of nylon 6/clay-reinforced nanocomposite. *Polymer Testing*, 23(6):629–636, 2004.
- [234] B. Van Hooreweder, D. Moens, R. Boonen, J. P. Kruth, and P. Sas. On the difference in material structure and fatigue properties of nylon specimens produced by injection molding and selective laser sintering. *Polymer Testing*, 32(5):972–981, 2013.
- [235] K. Shahzad, J. Deckers, Z. Zhang, J. P. Kruth, and J. Vleugels. Additive manufacturing of zirconia parts by indirect selective laser sintering. *Journal of the European Ceramic Society*, 34(1):81–89, 2014.



- [236] B. Van Hooreweder and J. P. Kruth. High cycle fatigue properties of selective laser sintered parts in polyamide 12. *CIRP Annals*, 63(1):241–244, 2014.
- [237] D. W. Koon and C. J. Knickerbocker. What do you measure when you measure resistivity? *Review of scientific instruments*, 63(1):207–210, 1992.
- [238] I. Miccoli, F. Edler, H. Pfnür, and C. Tegenkamp. The 100th anniversary of the four-point probe technique: the role of probe geometries in isotropic and anisotropic systems. *Journal of Physics: Condensed Matter*, 27(22):223201, 2015.
- [239] L. B. Valdes. Resistivity measurements on germanium for transistors. *Proceedings of the IRE*, 42(2):420–427, 1954.
- [240] J.K.W. Sandler, S. Pegel, M. Cadek, F. Gojny, M. Van Es, J. Lohmar, W.J. Blau, K. Schulte, A.H. Windle, and M.S.P. Shaffer. A comparative study of melt spun polyamide-12 fibres reinforced with carbon nanotubes and nanofibres. *Polymer*, 45(6):2001–2015, 2004.
- [241] A. R. Bhattacharyya, S. Bose, A. R. Kulkarni, P. Pötschke, L. Häußler, D. Fischer, and D. Jehnichen. Styrene maleic anhydride copolymer mediated dispersion of single wall carbon nanotubes in polyamide 12: crystallization behavior and morphology. *Journal of applied polymer science*, 106(1):345–353, 2007.
- [242] R. Socher, B. Krause, S. Hermasch, R. Wursche, and P. Pötschke. Electrical and thermal properties of polyamide 12 composites with hybrid fillers systems of multiwalled carbon nanotubes and carbon black. *Composites Science and Technology*, 71(8):1053–1059, 2011.
- [243] A. R. Bhattacharyya, T. V. Sreekumar, T. Liu, S. Kumar, L. M. Ericson, R. H. Hauge, and R. E. Smalley. Crystallization and orientation studies in polypropylene/single wall carbon nanotube composite. *Polymer*, 44(8):2373–2377, 2003.
- [244] L. Zonder, A. Ophir, S. Kenig, and S. McCarthy. The effect of carbon nanotubes on the rheology and electrical resistivity of polyamide 12/high density polyethylene blends. *Polymer*, 52(22):5085–5091, 2011.
- [245] A. Bharati, R. Cardinaels, J. W. Seo, M. Wübbenhorst, and P. Moldenaers. Enhancing the conductivity of carbon nanotube filled blends by tuning their phase separated morphology with a copolymer. *Polymer*, 79:271–282, 2015.
- [246] M. Wang, W. Wang, T. Liu, and W. D. Zhang. Melt rheological properties of nylon 6/multi-walled carbon nanotube composites. *Composites Science and Technology*, 68(12):2498–2502, 2008.
- [247] S. Y. Kwon, I. M. Kwon, Y. G. Kim, S. Lee, and Y. S. Seo. A large increase in the thermal conductivity of carbon nanotube/polymer composites produced by percolation phenomena. *Carbon*, 55:285–290, 2013.
- [248] Z. Han and A. Fina. Thermal conductivity of carbon nanotubes and their polymer nanocomposites: A review. *Progress in polymer science*, 36(7):914–944, 2011.

- [249] N. Patil, L. Balzano, G. Portale, and S. Rastogi. A study on the chain- particle interaction and aspect ratio of nanoparticles on structure development of a linear polymer. *Macromolecules*, 43(16):6749–6759, 2010.
- [250] N. Mahmood, M. Islam, A. Hameed, and S. Saeed. Polyamide 6/multiwalled carbon nanotubes nanocomposites with modified morphology and thermal properties. *Polymers*, 5(4):1380–1391, 2013.
- [251] M. Razavi-Nouri, M. Ghorbanzadeh-Ahangari, A. Fereidoon, and M. Jahanshahi. Effect of carbon nanotubes content on crystallization kinetics and morphology of polypropylene. *Polymer Testing*, 28(1):46–52, 2009.
- [252] J. C. Huang. Carbon black filled conducting polymers and polymer blends. *Advances in Polymer Technology: Journal of the Polymer Processing Institute*, 21(4):299–313, 2002.
- [253] W. Zhang, A. A. Dehghani-Sani, and R. S. Blackburn. Carbon based conductive polymer composites. *Journal of materials science*, 42(10):3408–3418, 2007.
- [254] W. Steinmann, T. Vad, B. Weise, J. Wulfhorst, G. Seide, T. Gries, M. Heidelmann, and T. Weirich. Extrusion of cnt-modified polymers with low viscosity-influence of crystallization and cnt orientation on the electrical properties. *Polymers and Polymer Composites*, 21(8):473–482, 2013.
- [255] S. K. H. Gulrez, M. E. Ali Mohsin, H. Shaikh, A. Anis, A. Manjaly Pulose, M. K. Yadav, E. H. P. Qua, and S. M. Al-Zahrani. A review on electrically conductive polypropylene and polyethylene. *Polymer composites*, 35(5):900–914, 2014.
- [256] J. F. Niven, M. B. Johnson, S. M. Juckes, M. A. White, N. T. Alvarez, and V. Shanov. Influence of annealing on thermal and electrical properties of carbon nanotube yarns. *Carbon*, 99:485–490, 2016.
- [257] Y. Pan, H. K. F. Cheng, L. Li, S. H. Chan, J. Zhao, and Y. K. Juay. Annealing induced electrical conductivity jump of multi-walled carbon nanotube/polypropylene composites and influence of molecular weight of polypropylene. *Journal of Polymer Science Part B: Polymer Physics*, 48(21):2238–2247, 2010.
- [258] A. Bharati, P. Hejmady, T. Van der Donck, J. W. Seo, R. Cardinaels, and P. Moldenaers. Developing conductive immiscible polystyrene/polypropylene blends with a percolated conducting polyaniline/polyamide filler by tuning its specific interactions with the styrene-based triblock compatibilizer grafted with maleic anhydride. *Journal of Applied Polymer Science*, 137(9):48433, 2020.



## Publications

Belonging to this thesis:

1. Hejmady, P., Cleven, L. C., Van Breemen, L. C. A., Anderson, P. D., & Cardinaels, R. (2019). A novel experimental setup for in situ optical and X-ray imaging of laser sintering of polymer particles. *Review of Scientific Instruments*, 90(8), 083905.
2. Hejmady, P., Van Breemen, L. C. A., Anderson, P. D., & Cardinaels, R. (2019). Laser sintering of polymer particle pairs studied by in situ visualization. *Soft Matter*, 15(6), 1373-1387.
3. Hejmady, P., Van Breemen, L. C. A., Anderson, P. D., & Cardinaels, R. Production of spherical particles from thermoplastic polymers through droplet retraction *submitted to Powder Technology*
4. Hejmady, P., Van Breemen, L. C. A., Anderson, P. D., & Cardinaels, R. Laser sintering of PA12 particles studied by in-situ optical, thermal and X-ray characterization. *submitted to Additive Manufacturing*
5. Hejmady, P., Van Breemen, L. C. A., Anderson, P. D., & Cardinaels, R. Laser sintering on polyamide 12/MWCNT composite particle pairs. *to be submitted*
6. Balemans, C., Hejmady, P., Cardinaels, R., & Anderson, P. D. (2019). Towards unraveling the sintering process of two polystyrene particles by numerical simulations. *Korea-Australia Rheology Journal*, 31(4), 285-295
7. Hejmady, P., Cardinaels, R. M., Van Breemen, L. C. A. A. & Anderson, P. D., 20 Apr 2020, Polymer spheres., Patent No. 19156044.0-1102, 7 Feb 2019

Other Contributions :

1. Bharati, A., Hejmady, P., Cardinaels, R., Seo, J. W., & Moldenaers, P. (2017, December). Inducing conductivity in immiscible PS/PP blends by a percolated polyaniline/PA filler selectively localised by specific interactions. In AIP Conference Proceedings (Vol. 1914, No. 1, p. 050002). AIP Publishing LLC.
2. Bharati, A., Hejmady, P., Van der Donck, T., Seo, J. W., Cardinaels, R., & Moldenaers, P. (2020). Developing conductive immiscible polystyrene/polypropylene blends with a percolated conducting polyaniline/polyamide filler by tuning its specific interactions with the styrene-based triblock compatibilizer grafted with maleic anhydride. *Journal of Applied Polymer Science*, 137(9), 48433.



## Acknowledgment

Welcome to the most read part of the thesis. It's been a great pleasure working with people of different age, mindset and culture which has nurtured me, personally and professionally. My gratitude to Patrick for giving the freedom in exploring the project, for collaborations in various projects and the opportunities you gave in presenting our work at conferences. Also, for the valuable advice on how work and life can be balanced, my thanks and appreciation. To Lambert for the valuable advice, guidance and for the tips with the presentations, but above all for showing how things can be done differently. To Ruth, foremost I am grateful to you in shaping this work at every step. Learning from you on being critical and diligent has helped me changing my perspective and approach. Lastly, thanks for keeping a tab on me when needed. Cheers to you guys on making this work a success together, marking a stepping stone for forthcoming works. I would like to thank Brightlands Material Center (BMC) for funding my PhD project, providing me with opportunities to connect with people from various academia and industries. Thanks to the members of my committee for being part of this, and for all the valuable comments. Behind the scene there have always been people supporting this project directly or indirectly, thank you guys. Starting from Lucien, for our great collaboration which led to this unique setup and our first publication together, to Daniel for all the support and the non-stop resilience we showed at ESRF with the successful experiments. Tom Sama, for all the helpful resources, discussions, and sharing some of your unique playlist. Gerrit and Leon for the valuable discussion and materials you provided in the early phase of the project, and lastly to dear Ans, for the support and the nice discussions we had in late working hours. Ups and downs are a constant part of this journey, but support from friends is precious. You know who you are, and I cherish your companionship and trust, Thank You, Dhanyawad, Grazie Mille, Muchas Gracias, mamnoon, Dank je, Obrigado, Shukraan. . . To my young energetic buddies at Keiron, thanks for the co-operation as always, we have a long way to go, let's keep it rolling. Finally to my family from Bangalore to Boston, love and respect, for all the support, my deepest gratitude.



## Curriculum Vitae

Prakhyat Hejmady was born on 3rd of March 1989 in Mulki, India. After obtaining his Bachelor's degree in Mechanical Engineering in January 2011, he followed his interest in research at Raman Research Institute, Bangalore, India, as a Research Assistant in the Soft Condensed Matter group until August 2013. During these years, he studied the flow of granular material and crack propagation in non-newtonian media, under the supervision of prof. Ranjini Bandhyopadhyay and prof. Abhishek Dhar.

He obtained a full scholarship from the European Union Commission, to pursue his Master's degree in an Erasmus Mundus program (EURHEO), at University of Minho (UMINHO), Guimarães, Portugal and Katholieke Universiteit Leuven (KUL), Leuven, Belgium. He carried out his Master's thesis at the Department of Chemical Engineering, KUL, titled "Developing conducting blends by percolation of conducting polymers in immiscible blends" under the supervision of prof. Paula Moldenaers. In July 2015, he received his Master's degree in Chemical Engineering with specialization in polymer processing and rheology. After completion of his Master's degree, Prakhyat took a position as a Doctoral candidate in Polymer Technology group at Eindhoven University of technology, Eindhoven, Netherlands, under the supervision of prof.dr.ir. P.D. Anderson and co-supervisors, dr.ir. R. Cardinaels and dr.ir. L.C.A. van Breemen, of which the results are presented in this dissertation.

In February 2020, Prakhyat joined Canon, Venlo, The Netherlands as a Material & Process Interaction Researcher. He is the co-founder of Keiron Printing Technologies B.V., Eindhoven, The Netherlands.